

METABOLIC HETEROGENEITY IN ISCHEMIA REPERFUSION INJURY:

THE INSIDE STORY

by

Robert Kazmierski

A dissertation submitted to Johns Hopkins University in conformity with the
requirements for the degree of Doctor of Philosophy

Baltimore, Maryland
October, 2014

© 2010 Robert T. Kazmierski
All Rights Reserved

Abstract

It is well established that ischemia reperfusion (IR) injury can lead to life-threatening arrhythmias. Our group introduced the theory of metabolic sinks as a novel cause of arrhythmogenesis in a heart exposed to IR injury. Metabolic sinks are clusters of myocytes in which ischemia-induced reduction of ATP:ADP ratio increases open probability of sarcolemmal ATP-sensitive K^+ channels. This in turn leads to hyperpolarization of membrane potential that reduces or ablates electrical excitability within the affected region of myocardium. To date, studies of metabolic sinks in intact hearts have been largely limited to use of fluorescent indicators to image mitochondrial membrane potential on the epicardial surface. This has revealed the existence of spatio-temporally evolving regions of myocardium within which mitochondrial membrane potential is depolarized, and whose presence influences electrical conduction and action potential duration. In order to explore the three-dimensional structure of metabolic sinks within the myocardium, we have developed a protocol for labeling an intact guinea pig heart exposed to IR injury and imaging any portion of the labeled heart using a custom designed automated volume imaging microtome (AVIM) to overcome the limited imaging field of laser scanning microscopy (LSM). Our AVIM is composed of low-cost components that can be easily installed and removed from a shared microscope. We have developed an open-source software signal processing pipeline to correct for imaging artifacts inherent to LSM and effectively reconstruct the acquired image volumes. Using this approach, we show that hearts undergoing reperfusion arrhythmias have an endocardium containing mostly depolarized mitochondria, with an abrupt transition to repolarized mitochondria in mid-myocardial to epicardial regions. Hearts not exhibiting

reperfusion arrhythmias show a much more uniform distribution of depolarized mitochondria as a function of transmural location. These results show different stereotypical patterns of mitochondrial depolarization that are correlated with the presence and absence of reperfusion arrhythmias.

Thesis Committee

Raimond L. Winslow, Professor, Department of Biomedical Engineering, The Johns Hopkins University

Brian O'Rourke, Professor, Department of Medicine, Division of Cardiology, The Johns Hopkins University

Feilim Mac Gabhann, Assistant Professor, Department of Biomedical Engineering, The Johns Hopkins University

Acknowledgements

There are so many people who without which, this dissertation could not have been completed. As I write this I know that I will leave out so many who were integral to this endeavor; to you I apologize. Please know how much I appreciated all the help and guidance that was provided to me over the years. I really could not have done this without all of you.

First, I would like to thank my advisor, Rai Winslow. Without your unerring patience and guidance, I most likely would have lost my way and quit long ago. While I may not have been the most receptive of your advice and feedback at times, I appreciate now more than ever how invaluable your guidance has been and how much I have benefited from our meetings and discussions. Thank you so much for bearing with me and pushing me in the right direction over the years.

To Brian O'Rourke, I want to thank you for the countless hours spent discussing, evaluating, debugging, and advising over the years that I've been working with you. Without your diverse knowledge and calm approach to seemingly impossible experimental setbacks, I would still be lost in the details. The time spent in your lab has been instrumental in building my appreciation for "wet lab" experimentation.

To Feilim Mac Gabhann, I want to thank you for your time and willingness to discuss problems and questions even though you weren't directly involved with my projects. I have learned so much from your experimental knowledge and critical thinking skills.

To Aagam Shah, I want to thank you for the enormous commitment that you made to debugging and tweaking the final design of the AVIM. I cannot state how much help you have been over the years in dividing-and-conquering this huge task. Without your help and feedback, I would probably still be calibrating blades and running hearts. I wish you the best in your future studies.

To the rest of the Winslow, O'Rourke, and Mac Gabhann labs (both past and present), I want to thank you for being a great resource of both knowledge and encouragement. Pat, Joe, Jason, Troy, Yasmin, Laura, Lulu, Dave, An-Chi, Ting, Sonia, Miguel, Agnes, Alice, Soroosh, Mark, Peggy, Lindsay, Liz, Iraj, and Claire, it has been wonderful working with you, and I hope that future colleagues and friends are as supportive and as just plain fun to be around as all of you have been.

To Kyle Reynolds, I want to thank you for your help with the cluster and several other computer mishaps that have happened over the years. I am in awe over how calm and objective you can remain in the midst of such calamity and chaos.

And to my family, in particular my parents, I want to thank you so much for your love and support over the years. I have always looked up to you in your amazing endurance for hard work and seemingly endless patience and loving support of me. I would not be in the position to even start a doctoral thesis (much less actually write one) if it wasn't for your emphasis on education and hard work along with all the help you have given me in countless forms over the years.

And to my wife Meghan, I will never be able to articulate how much you mean to me and how much you have helped me through this endeavor. Your ability to calm me and

refocus me while I'm overwhelmed and overworked kept me going. I can't imagine where I would be without you today. Finally, a little shout-out to our baby on the way affectionately nicknamed Blueberry, BB, or Beebs - you gave me that final push to get out of school so that I can help support a family. I can't wait to meet you. But take your time in there – January will be early enough!

Table of Contents

Chapter 1 - Introduction.....	1
1.1 Cardiac Arrhythmogenesis in Ischemia-Reperfusion Injury	1
1.2 Automated Two-Photon Fluorescence Microscopy.....	4
Chapter 2 – Automated Volume Imaging Microtome	6
2.1 Methods.....	6
2.1.1 Instrument Design	6
2.1.2 Sample Preparation	14
2.1.3 Image Acquisition.....	15
2.1.4 Image Processing	20
2.1.5 Image Volume Reconstruction and Visualization	30
2.2 Results.....	30
2.3 Discussion.....	39
Chapter 3 - Spatial Properties of Metabolic Sinks and Their Relationship to Ischemia Reperfusion Arrhythmias.....	42
3.1 Methods.....	42
3.1.1 Sample Preparation	42
3.1.2 Image Acquisition.....	44
3.2 Results.....	45

3.3 Discussion	62
Chapter 4 - Conclusions and Future Directions	66
Appendix A AVIM Parts List	69
Off-the-shelf components	69
Custom-Machined Components.....	73
Wiring Diagram	76
Appendix B AVIM Operation Manual	77
Image Volume Acquisition Protocol	77
Turning on the system.....	77
Preparing the Sample to be Imaged	78
Setting Up Microscope	82
Setting up an Acquisition.....	87
Restarting the Acquisition.....	96
Image Volume Acquisition Worksheet.....	99
Image Volume Reconstruction Protocol.....	105
Gathering the Data	105
Reconstruction	107
Checking Slice Registration.....	110
Visualizing the Image Volume	112
Laser GDD Correction.....	114

Setting up a Quick Z Acquisition.....	116
Rotary Stage Alignment.....	117
Microtome Blade Adjustment.....	119
Appendix C Converting AVIM to Different Microscope.....	124
Changes to Acquisition LabVIEW Code.....	124
Bibliography	128

List of Tables

Table 1: Comparing In-Plane Correction Algorithms	25
---	----

List of Figures

Figure 2-1: AVIM Design and Integration	8
Figure 2-2: Minimizing Striations with Blade Selection and Example Cross Sections	9
Figure 2-3: Compensating for Inverter Cantilever Sag.....	12
Figure 2-4: Aligning 3D Stage Axes with Microscope Scanning Axes	13
Figure 2-5: AVIM Image Acquisition Sequence	16
Figure 2-6: Optical Stack Acquisition Setup	18
Figure 2-7: AVIM Image Processing Pipeline.....	21
Figure 2-8: Removing Image Vignetting.....	22
Figure 2-9: In-Plane Correction X & Y Profiles.....	24
Figure 2-10: Depth Correcting Acquired Images	29
Figure 2-11: Image Volume 3D Rendering and Virtual Cut Planes - Mouse Heart.....	32
Figure 2-12: Fiber Structure in Mouse Heart - Virtual Cut Planes.....	33
Figure 2-13: Fiber Inclination Angle for Mouse Left Ventricle	35
Figure 2-14: Fiber Inclination Angle for Mouse Right Ventricle.....	36
Figure 2-15: Interdigitation of Sheets in Mouse Left Ventricular Endocardium.....	38
Figure 3-1: Guinea Pig Control Hearts with Hoechst and Mitotracker	47
Figure 3-2: GP Hearts Rhythmic Beating with Transmural Bias	49
Figure 3-3: GP Hearts Rhythmic Beating without Transmural Bias	50
Figure 3-4: GP Hearts Sustained Reperfusion Arrhythmia	51
Figure 3-5: Recovery is More Sparse in Hearts without Transmural Bias	56
Figure 3-6: 3D Reconstruction of a Metabolic Sink.....	61

Chapter 1 - Introduction

Coronary heart disease (CHD) is the leading cause of death in the United States for both men and women resulting in over 400,000 deaths in 2006 or roughly 1 out of 6 deaths that year in the US [1]. CHD is characterized by the buildup of plaques on the walls of the coronary arteries reducing the flow of blood to cardiac tissue and, in severe events, leading to tissue ischemia and necrosis. Reperfusion of the affected cardiac region is the most common clinical treatment for acute ischemic events [2, 3]. Paradoxically, this reperfusion therapy itself can be a cause of arrhythmias and ultimately sudden cardiac death [4, 5].

It has been shown that periods of ischemia followed by reperfusion, termed ischemia-reperfusion (IR) injury, can create electrically non-conducting regions of tissue termed “metabolic sinks” [4, 6-8]. They are designated as metabolic sinks because metabolic imbalances create a condition where the region of tissue will draw in the stimulating current from surrounding healthy tissue, an effect that increases the likelihood of arrhythmogenesis [9]. Several studies have demonstrated the effects of metabolic sinks in the intact heart [4-8]. However, it has not been possible to fully characterize a metabolic sink in an intact heart due to technological limitations. Characterization has been limited to surface mapping of the epicardium, which neglects the effect of the heterogeneous metabolic activity across the wall of the left ventricle[10]. In order to investigate the effect of IR injury throughout the myocardium, new instrumentation and methodology is needed. But first, the basic mechanisms leading to metabolic sinks are presented.

1.1 Cardiac Arrhythmogenesis in Ischemia-Reperfusion Injury

Cardiac myocytes require a constant supply of energy to ensure normal function of the heart. It has been well established that during times of metabolic stress, the production of energy within cardiac mitochondria can become disrupted [11-13]. However, it was not until recently that a mechanism was proposed linking metabolic dysfunction to the formation of life-threatening arrhythmias in the heart [4]. Akar et al. first proposed the theory of metabolic sinks in hearts exposed to IR injury [4]. They describe a metabolic sink as a region of tissue that is still coupled to neighboring cells via gap junctions but inexcitable due to activation of ATP-sensitive K^+ (KATP) channels in the sarcolemma which occurs upon reduction of the ATP:ADP ratio. These regions of tissue act as a current sink, into which current flows from surrounding cells, but in which membrane depolarization is limited or absent. In surrounding healthy cells, action potential duration (APD) can be reduced or membrane depolarization can be completely ablated because the current sinks remain electrically connected to these cells via gap junctions. This creates a reduced effective refractory period due to the shortened APD in surrounding cells and increases dispersion of APD within the myocardium, effects have both been shown be arrhythmogenic [14, 15].

The formation of metabolic sinks is related to reactive oxygen species (ROS) signaling [12, 16]. During metabolic stress, mitochondrial ROS concentration increases. This leads to a flux of ROS through the inner membrane anion channel (IMAC) into the intermembrane space. Once the level of ROS within this space reaches a critical concentration, open probability of the IMAC increases abruptly, inducing more ROS release and depolarization of mitochondrial membrane potential (ψ_m) in a process known as ROS-induced ROS-release (RIRR) [17]. RIRR can result in propagating waves of

ROS within the mitochondrial network [12, 16], producing uncoupling of oxidative phosphorylation and energy dissipation within the myocyte. As the ATP:ADP ratio decreases, open probability of KATP channels in the sarcolemma increases. The region of cells in which this occurs is known as a metabolic sink.

In order to investigate metabolic sinks in the context of the myocardium, several studies have labeled polarized mitochondria throughout intact rodent hearts using fluorescent dyes. Slodzinski et al. loaded a guinea pig (GP) heart with tetramethylrhodamine ethylester and, using a two-photon microscope to image the epicardium of the heart, was able to demonstrate the existence of clusters of cells lacking a fluorescent signal, i.e. cells with depolarized ψ_m [6]. This study provided the first view of a metabolic sink in an intact heart. Lyon et al. built upon this and expanded the area of epicardium that could be imaged by using optical mapping on a rat heart loaded with tetramethylrhodamine methylester, demonstrating waves of ψ_m depolarization during ischemia[8].

Previous studies have been limited to imaging of the epicardium due to the reliance on fluorescent dyes, which must be imaged using an optical modality, and the lack of methodology to expand this modality beyond the epicardium. Thus there is no understanding of the three dimensional (3D) structure and any transmural dependency of metabolic sink architecture. Such an understanding is important because it has been well established that the endocardium has a different metabolic profile as compared to the epicardium [10, 18-21]. In particular, the endocardium of the left ventricle consumes more oxygen, undergoes a higher amount of strain, and contracts for a longer period of time as compared to the epicardium [18, 21]. Therefore, in order to understand the effects of metabolic sinks and their contribution to reperfusion arrhythmias, it is important to

label and image them throughout the myocardium. In order to achieve this, we will expand the capabilities of the traditional two-photon microscope through the use of custom instrumentation and software.

1.2 Automated Two-Photon Fluorescence Microscopy

Two-photon microscopy (TPM) and confocal microscopy (together referred to as laser scanning microscopy, LSM) have been widely adopted as integral tools in biological research since their development [22, 23]. They provide the ability to acquire submicron resolution images of a variety of fluorescent markers. Researchers have applied these technologies to image a variety of structures within the cell including cytoskeletal components [24], t-tubule organization [25], ion channel localization [26], extracellular components such as collagen [27] and vasculature [28]. These techniques have been applied in diverse fields of disease research including Alzheimer's [29], cancer [30], and heart failure [25]. The ability of TPM to image fluorescent markers throughout a thick specimen up to approximately 1 mm [31] greatly expanded upon the imaging capabilities of the confocal microscope [32]. However, due to its limited depth penetration, it is not possible to use LSM alone to image large-scale macroscopic tissues or organ structure.

Driven by this need to image larger specimens, several groups have designed and built automated systems that expand on LSM imaging capabilities. Ragan et al. developed an automated high resolution 3D stage to position samples beneath the microscope objective and interfaced the stage with an automated microtome[33]. Sequential positioning and imaging of the sample, followed by removal of the imaged material allowed for image volumes to be collected throughout macroscopic samples that had been fixed and

embedded in paraffin. Sands et al. further developed this technique by integrating an ultramiller into the automated setup allowing the sample to be embedded in agar resin, thereby eliminating the quenching of fluorescent signal by paraffin. Ragan et al. introduced a vibratome into their design that allowed the use of agarose as the embedding media, enabling collection of the tissue sections following the cut step for archival purposes [34, 35].

These automated imaging instruments enable the collection of many high quality image volumes. However, each instrument thus far requires a dedicated confocal or two-photon microscope, and the cost of the microtome system is high. These factors present a barrier to more widespread adoption of these techniques. For our investigation of metabolic sinks throughout the myocardium and more generally for the field of LSM, it is important that these barriers are removed.

Chapter 2 – Automated Volume Imaging Microtome

In order to expand the capabilities of a two-photon microscope, we have designed an automated volume imaging microtome (AVIM) that can be quickly installed and removed from a shared microscope. This newly designed AVIM enables the collection of high quality image volumes despite its relatively low manufacturing cost. We achieve this by leveraging image processing techniques to overcome limitations of lower cost microtome technologies. Here, we describe the design of the AVIM and demonstrate its application to high spatial resolution reconstruction of whole mouse hearts to gain insight into the organization of fibers and sheets throughout the organ.

2.1 Methods

2.1.1 Instrument Design

Instrument design follows that of Ragan et al. [33]. The automated volume imaging microtome (AVIM) shown in Figure 2-1A consists of a high resolution 3D stage (3DMS, Sutter Instruments, Novato, CA) with a custom machined platform to allow mounting of a linear slide (Edmund Optics, Barrington, NJ) and microactuator (L12, Firgelli, Victoria, BC, Canada). The sample, embedded in paraffin on a standard mounting cassette, is attached to the linear slide with custom machined mounts. A microactuator moves the sample from the objective, beneath the blade for sectioning, and back to the objective. The microtome is comprised of custom-machined knife holder arms with brass-tipped set screws that allow precise calibration of the cutting angle. Initially, disposable low-profile blades were used. However, cutting artifacts, which we refer to as striations, appeared on the sample (indicated by arrows in Figure 2-2A) before an entire volume could be

acquired. A variety of disposable blades manufactured by Leica, TissueTek, C.L. Sturkey were evaluated. These included low and high profile versions of gold, silver and diamond coated blades and tungsten carbide blades. Reusable steel knives manufactured by C.L. Sturkey provided the best results, allowing a complete image volume to be acquired before problematic cutting artifacts were noticeable, see Figure 2-2B.

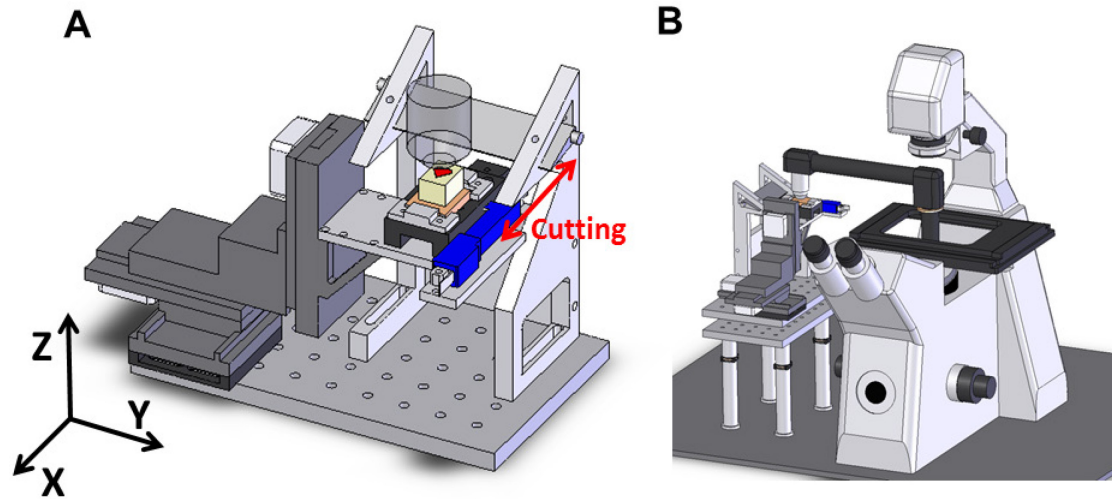


Figure 2-1: AVIM Design and Integration

The AVIM consists of an automated 3D stage that positions the sample beneath the microscope objective (shown in transparency). The stage holds a linear slide that facilitates the movement of the sample between the objective and the microtome and an actuator (in blue) that provides the travel between the two. The sample (red heart symbol) is embedded in paraffin on a standard cassette (orange) and is mounted to the linear slide with custom machined mounts. (B) The AVIM is positioned adjacent to the Zeiss 7MP microscope and optically interfaced via an objective inverter that allows for quick installation and removal of the AVIM from the microscope.

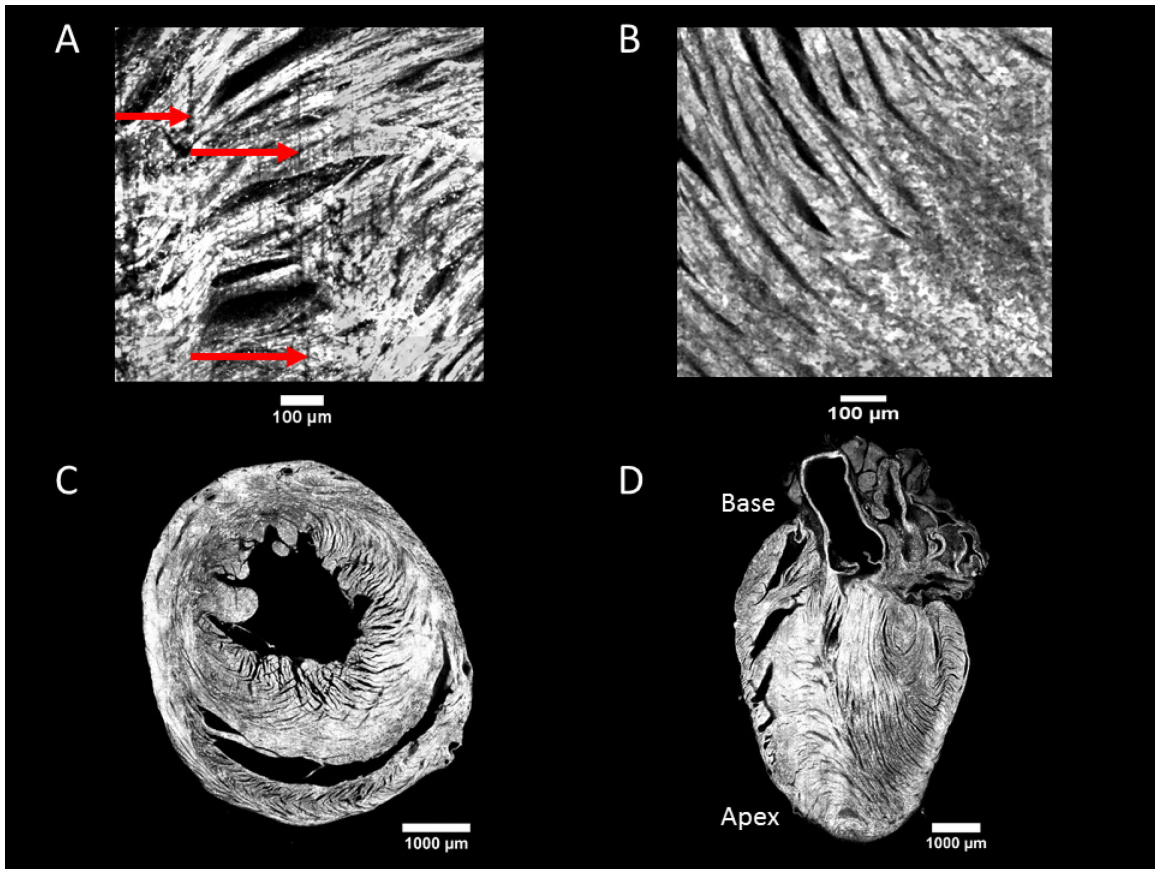


Figure 2-2: Minimizing Striations with Blade Selection and Example Cross Sections

(A) Vertical striations, shown by red arrows are visible in the sample sectioned with a low-profile disposable blade. (B) A sample sectioned with a reusable steel knife from C.L. Sturkey. Cutting artifacts are minimal throughout a complete image volume acquisition. (C) Example image of a heart embedded with the base-apex axis perpendicular to the cutting axis. (D) Example image of a heart embedded with the base-apex axis parallel to the cutting axis.

The AVIM is mounted adjacent to a Zeiss 7MP system (Carl Zeiss, Thornwood, NY; see Figure 2-1B). An InverterScope Objective Inverter (LSM Tech, Wellsville, PA) is used to interface the AVIM with the microscope. The inverter extends the objective point of installation from the microscope to an upright position adjacent to microscope body. This allows the AVIM to be fixed beneath the new position of the microscope objective, and also allows for easy installation and removal of the AVIM from the microscope so that other users can utilize the standalone microscope. This inverter has two degrees of freedom that can cause poor image quality in the resulting image volume if not addressed. First, the objective inverter, due to its cantilever design, can introduce a slight amount of misalignment between the imaging plane and the surface of the sample. In order to check for this, the focal plane is adjusted to the uppermost portion of the sample, and the vignette pattern of the acquired image tile at this location is viewed. A typical vignette can be seen in Figure 2-3 with uniform intensity drop-off towards the periphery of the image tile. Any variation from this pattern implies a misalignment between the imaging plane and the surface of the sample. This is corrected by fine-tuning the height adjusters on the posts supporting the AVIM's platform, indicated by yellow arrows in Figure 2-3. Through trial and error, the desired vignette pattern can be restored, helping to minimize in-plane imaging artifacts. Second, the objective inverter can be rotated around its attachment point on the microscope. Markings on the inverter and microscope (not shown) help correctly position the objective inverter during installation, but fine-tuning is necessary in order to align the scanning axes of the microscope with the travel of the 3D automated stage. This is done by collecting a plane of images across the surface of the sample and reconstructing them into an image slice. If any misalignment is present,

adjacent image tiles will show a disconnect in structure, see Figure 2-4A. This is remedied by adjusting a rotary stage between the two platforms, indicated by the red arrow in Figure 2-4B.

The operation of the AVIM is controlled by custom LabVIEW software (National Instruments, Austin, TX). Communication between the AVIM and microscope is conducted via bidirectional trigger signals to coordinate their actions during image acquisition. We make use of the Multi-Time software package within the ZEN imaging software (Carl Zeiss, Thornwood, NY). Because of the flexibility of Multi-Time, we were able to work with the manufacturer to improve the reliability of the communication between the microscope and the AVIM, decreasing the time between stack acquisitions in the process.

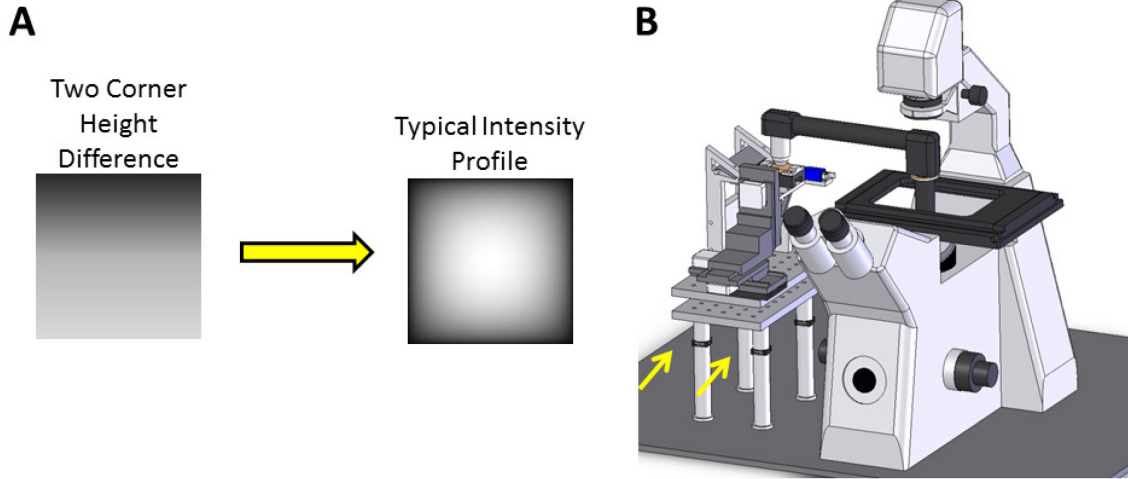


Figure 2-3: Compensating for Inverter Cantilever Sag

The surface of the sample is adjusted to match the focal plane of the objective. (A) Upon installation of the objective inverter, a sample image tile is collected on the surface of the sample. Any non-symmetric vignette implies a misalignment between the sample surface and the focal plane. (B) Height adjusters, indicated by yellow arrows, are adjusted to create a typical intensity profile seen in A.

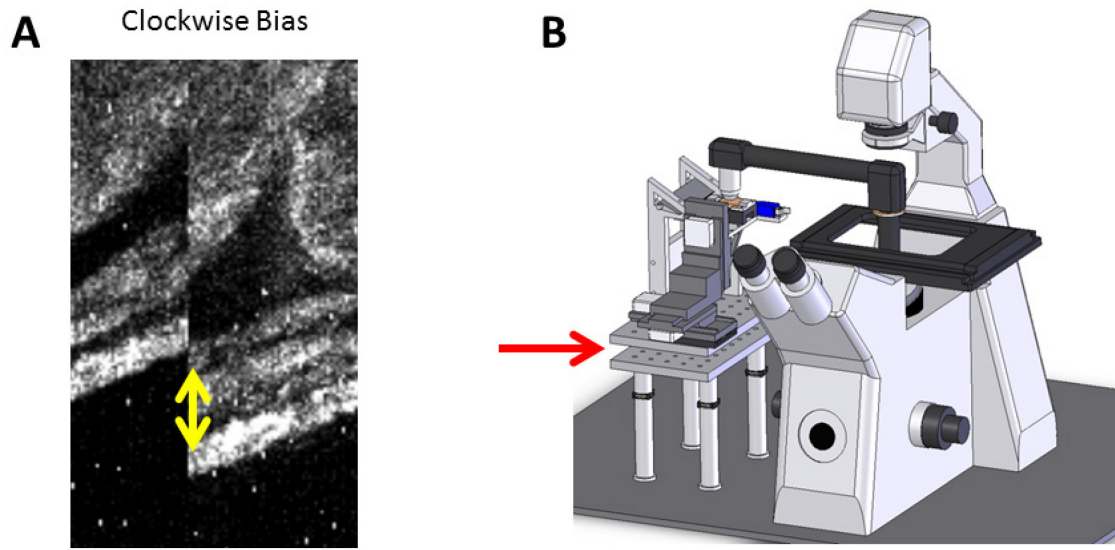


Figure 2-4: Aligning 3D Stage Axes with Microscope Scanning Axes

The scanning axes of the microscope are brought into alignment with the axes of the stage travel. (A) Misalignment between the two axes results in misalignment of structures between adjacent image tiles after reconstruction. Yellow double arrow demonstrates the mismatch in structure between two image tiles. (B) Adjustment of a rotary stage between the two platforms (indicated by the red arrow) brings the two axes into alignment.

2.1.2 Sample Preparation

We illustrate the imaging quality of our system by large-scale reconstruction of whole mouse heart ventricles. All surgical protocols were approved by the Animal Care and Use Committee of the Johns Hopkins University. Adult male mice were anesthetized with ketamine/xylazine/atropine (80/8/0.08 mg/kg) intraperitoneal. The jugular vein was surgically exposed and 375 units heparin slowly injected. The mouse was then euthanized with intraperitoneal injection of pentobarbital (0.25 mg/kg). The heart was rapidly excised and retrograde perfused through the aorta with cold cardioplegic solution at constant flow (3ml/min). After the heart was cleared of blood, the fluorescent indicator Di-4ANEPPS was added to the perfusate (0.05 mg/ml), and perfusion was continued for 25 minutes to ensure thorough and uniform labeling of sarcolemmal membrane. The heart was then fixed by perfusing pH-balanced 4% paraformaldehyde prepared fresh that day. Following 5 minutes perfusion of the fixative, the heart was submerged in the fixative for 2 hours to ensure thorough fixation. The heart was then rinsed twice with phosphate buffered solution (PBS) (Life Technologies, Grand Island, NY) and stored in PBS for less than 6 hours before dehydration and embedding. The fixed sample was dehydrated with a graded ethanol, xylene series (ethanol 80% / 95% / 95% / 100% / 100%; xylene 100% / 100%; 1 hour each at 40° C) immediately followed by immersion in paraffin (4 immersions of 1 hour each at 60° C); all steps were performed under negative pressure and agitation. Samples were embedded so that in-plane imaging and cutting could either be perpendicular (Figure 2-2C) or parallel (see Figure 2-2D) to the base-apex axis. Special care was taken during the embedding step to prevent deforming the heart while positioning it in the paraffin mold.

2.1.3 Image Acquisition

The AVIM interfaces with a Zeiss 7MP two-photon microscope. Figure 2-5 demonstrates the automated image acquisition process. The AVIM initially positions the sample beneath the microscope objective so that an area of the sample can be imaged (Figure 2-5A), in our case 850 μm by 850 μm for a 10X Apochromatic C objective. This corresponds to a square 512 x 512 voxel image at the spatial resolution per voxel of 1.6 μm in-plane and 10 μm out-of-plane.

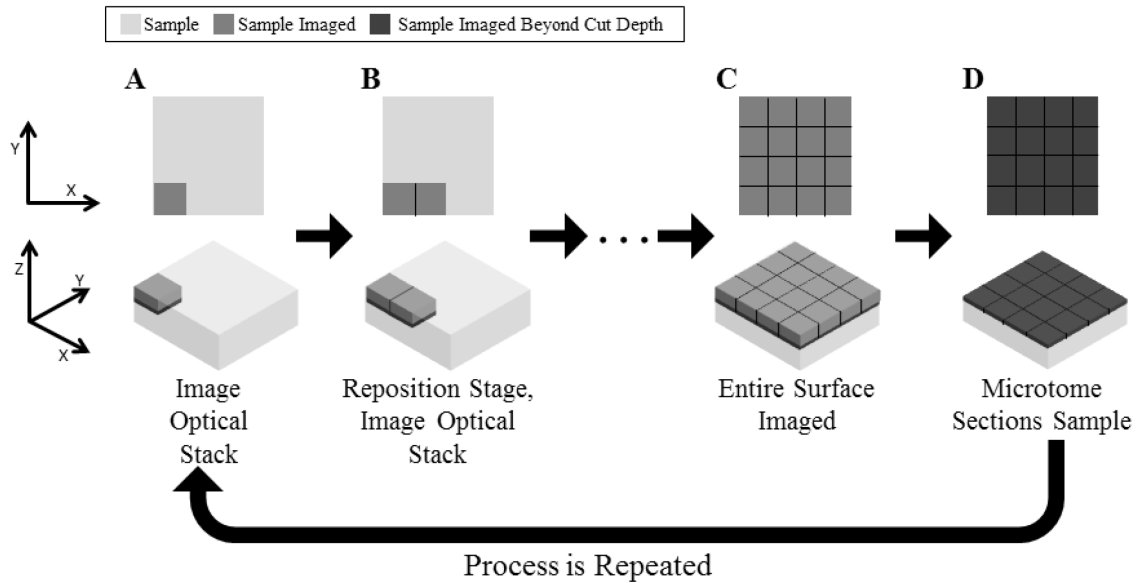


Figure 2-5: AVIM Image Acquisition Sequence

An optical stack of images consisting of several z-steps into the sample is acquired at a location on the sample. The sample is repositioned and another optical stack is acquired adjacent to the prior. This repositioning and optical stack acquisition is repeated until the entire surface of the sample has been imaged. The sample is then sectioned to remove most of the imaged material. Some overlap between cuts is imaged twice for later image registration. Following sectioning, the process is repeated until the entire volume of the sample has been imaged.

Excitation wavelength is set to 740nm. A single 512 x 512 voxel image acquired in the x-y plane is referred to as an image tile. The focal plane of the objective is adjusted so that several 512 x 512 image tiles are acquired at increasing depths in the z-direction (in this case 10 microns) into the sample (optical sectioning). The set of tiles collected at the same x-y positions for different depths is referred to as an optical stack. Typically, the total depth that can be imaged is limited to approximately 60 μm in cardiac tissue before photon scattering and absorption degrades image quality. Because of the refractive index mismatch between the air and paraffin, the actual depth of the focal plane must be calculated from Equation 1.

$$D_c = D_a \frac{n_1}{n_2} \quad (1)$$

In this equation, D_c is the actual (or depth of focal plane in sample due to refractive index mismatch) depth of the focal plane, D_a is the apparent depth (or depth the focal plane would be without a refractive index mismatch), n_1 is the refractive index for air ($n_1 = 1.00$), and n_2 is the refractive index for paraffin ($n_2 = 1.47$). An optical stack range is defined to be 130 μm tall with 10 μm steps in the z-direction so that the tiles with optimal image quality (approximately 60 μm in z as mentioned previously) appear at the center of the optical stack, see Figure 2-6. This range in the optical stack ensures that high quality image tiles will be collected even if the cutting step accumulates some error. An extreme example of accumulated cutting error is demonstrated in Figure 2-6B and C.

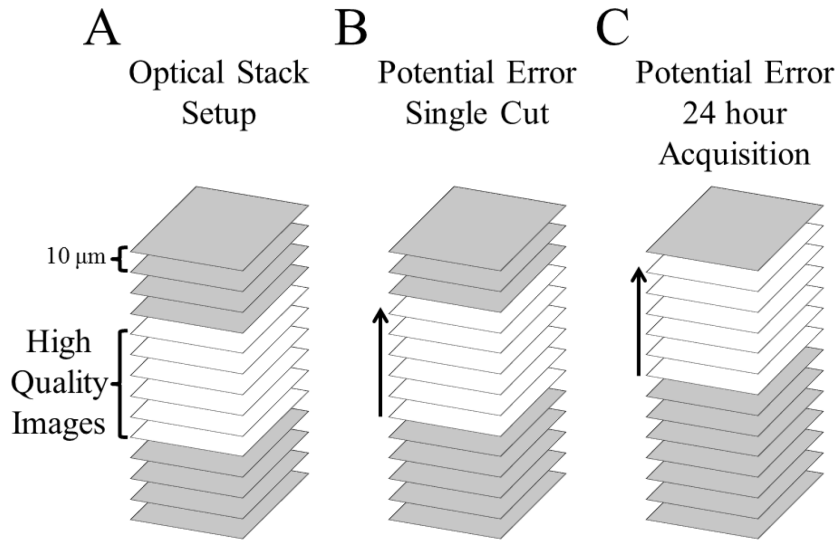


Figure 2-6: Optical Stack Acquisition Setup

High quality image collection is limited to a depth of within 60 μm of the sample surface (demonstrated with the white tiles). Additional tiles (shown in gray) are collected above and below this range to ensure high quality images are collected even in the case of a cut that is too shallow (as in B and C) or too deep. In a shallow cut, shown in B, this cutting error ($< 10 \mu\text{m}$) will shift the images used for image reconstruction (within the set of white tiles) up in relation to the gray tiles. Over the course of an acquisition, accumulation in error (shown in C) can shift the set of high quality images up several steps within the optical stack

Because the error is only in sample cutting height and not in relation to the stage or objective position, the location the image was acquired is still correctly recorded in this situation. The z-step was chosen as an optimal balance between the necessary resolution to demonstrate the cardiac architecture of the heart and a manageable amount of imaging time, i.e. smaller steps in z requires more imaging time. Following the acquisition of an optical stack, the AVIM repositions the sample beneath the objective so that an optical stack is collected over an adjacent area of the sample, Figure 2-5B. The prior stack acquired and the adjacent stack are adjusted to overlap approximately 10% of the image tile's dimension in either the x or y axis, depending on which axis the step was taken, in our case 50 voxels. This overlap between adjacent stacks eliminates the need to use the extreme edge of the acquired tiles where the optical aberrations are maximal. This process of positioning the sample and collecting an optical stack is repeated until the sample's surface has been imaged in its entirety, Figure 2-5C. The set of optical stacks collected over the surface of the sample is referred to as an intercut volume. The linear slide of the AVIM then transports the sample from beneath the objective to the microtome blade. The height of the sample is adjusted relative to the microtome blade so that a portion of the sample is removed. The portion of the sample removed is less than the portion imaged (depth of optical stack is greater than the cut depth); see Figure 2-5D. Typical sectioning depth is at or near 40 μm . The previously imaged portion of the sample remaining will be imaged again following the cut to serve as a reference for intercut volume alignment. The sample is returned to the objective to repeat the process of imaging the exposed surface, i.e. collecting another intercut volume. By repeating this as many times as needed, the sample can be imaged in its entirety. In its current design,

the AVIM can image samples as large as 25 x 25 x 20 mm in x, y, and z respectively. Imaging of a complete mouse heart requires roughly 5 days with the parameters used here. This time will be reduced or increased with larger or smaller steps in z, respectively.

The actuator needed for the microtome sectioning introduces some error in the coordinates between cuts. This is minimized by limiting the travel of the actuator so that the imaging position is defined by the linear slide hitting a set screw before the actuator reaches the fully retracted position, rather than relying on the fully retracted position of the actuator as the imaging position. This results in less than 20 μm error between cuts as compared to almost 200 μm (specified by the manufacturer) when using the fully retracted position of the actuator as the imaging position. Correction of the actuator-induced error is described in the image processing methodology.

2.1.4 Image Processing

The software pipeline for processing collected images consists of several steps as shown in Figure 2-7. Two-photon imaging creates certain artifacts that can be corrected, mainly image vignetting within the plane of imaging and signal attenuation as the plane of imaging is moved deeper into the sample. The first image processing step is referred to as in-plane tile intensity correction, Figure 2-7B. The primary purpose of this step is to remove center to edge intensity variation in each tile known as vignetting. Figure 2-8A demonstrates how a vignette on the individual tiles results in noticeable artifacts when the tiles are stitched into a plane.

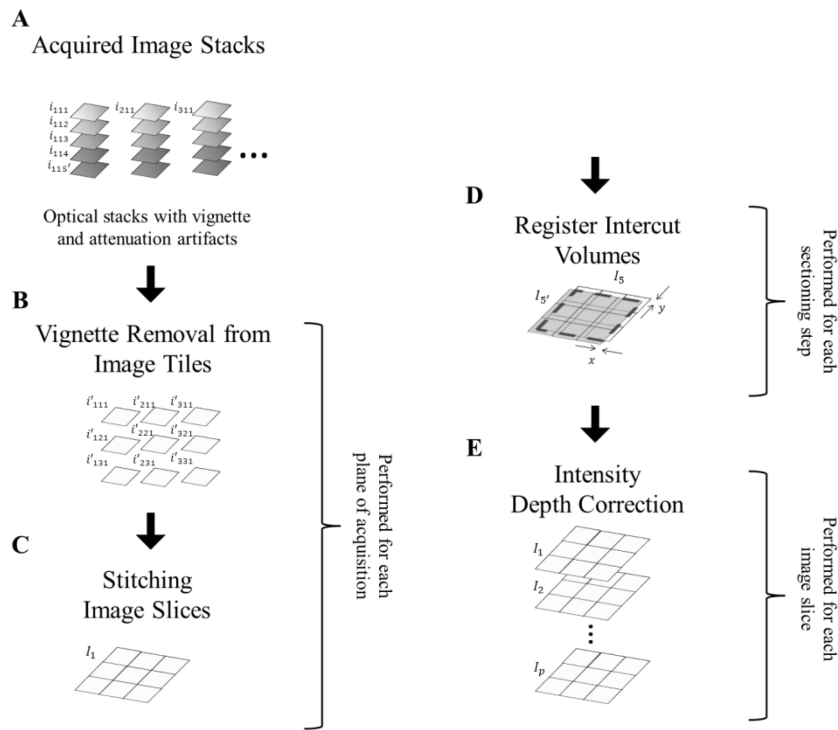


Figure 2-7: AVIM Image Processing Pipeline

Images are acquired by the microscope as optical stacks, shown here as 5 images deep. The image tiles, i (with subscripts indicating x, y, and z index respectively), have both vignetting artifacts and intensity attenuation with increasing imaging depth. (A) In this diagram, 3 stacks are acquired across the surface of the sample in both x and y, and a total of p locations in the z-axis were acquired throughout the sample. (B) Image tiles are grouped by plane of acquisition for vignette removal. (C) Corrected image tiles, i' , are then stitched into image slices, I . (D) Image slices acquired at the same z location, I_5 and I_5' , are registered to one another to calculate any displacement (in x and/or y) introduced by microtome sectioning for each of the cuts performed for the acquisition. (E) Finally, the image slices are corrected for intensity attenuation due to increased imaging depth.

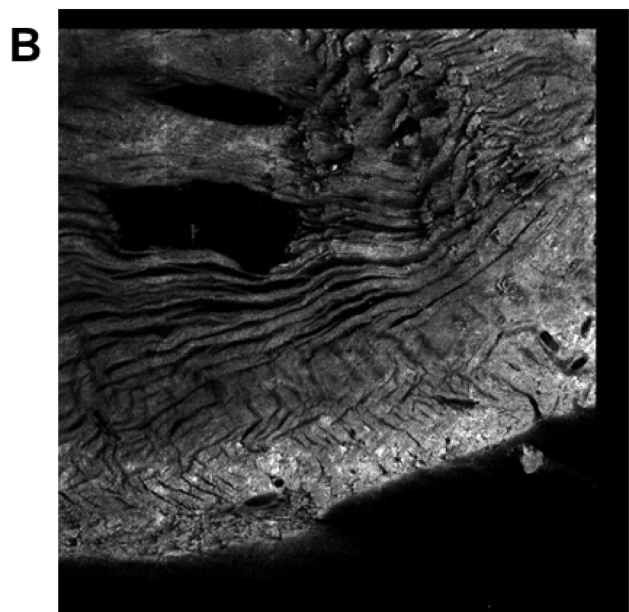
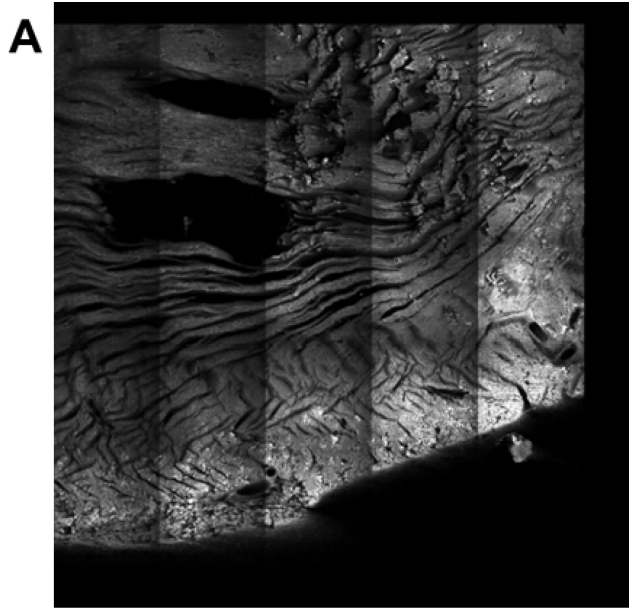


Figure 2-8: Removing Image Vignetting

Collected tiles of cardiac tissue are stitched together into an image slice before vignette-removal (A) and after vignette-removal (B). Correction algorithm from Chow et al. [36].

Image vignetting is removed in an automated fashion using previously developed methods [36]. This was the better performing algorithm of the two considered [36, 37]. Briefly, Chow et al.'s algorithm builds an average intensity tile for each plane of acquisition by averaging each pixel location within a tile throughout all image tiles acquired in that plane. The image tiles for that plane are then corrected by dividing them by the average intensity tile and multiplying by the average pixel intensity among all coordinates for that plane. See Figure 2-8B for an example of vignette-removal using this algorithm.

A second in-plane correction algorithm developed by Hovhannisyan et al. was considered[37]. Their method takes the average intensity tile as described above and projects average pixel values for that tile in the x and y directions. Using this method, Figure 2-9 plots the x and y pixel intensity profiles for a representative average intensity tile. A quadratic function is then fit to the x and y profiles, and discrete values are taken from this function to fill a row and column vector for the respective axes. These vectors are matrix multiplied to create a correction matrix. The image tiles are then divided by the correction matrix (element-wise division) to remove the in-plane bias.

In order to compare this method to the Chow algorithm described above, profiles of x and y average intensity values were generated from the output image tiles using each correction method. A perfectly flat x and y intensity profile was assumed to be the theoretical ideal correction, a technique introduced by Hovhannisyan. The mean squared error was calculated from the generated profiles to the ideal profile for each correction method. The results are displayed in Table 1. This comparison was done across several datasets, and the Chow algorithm brought the x and y profiles closest to ideal in all cases.

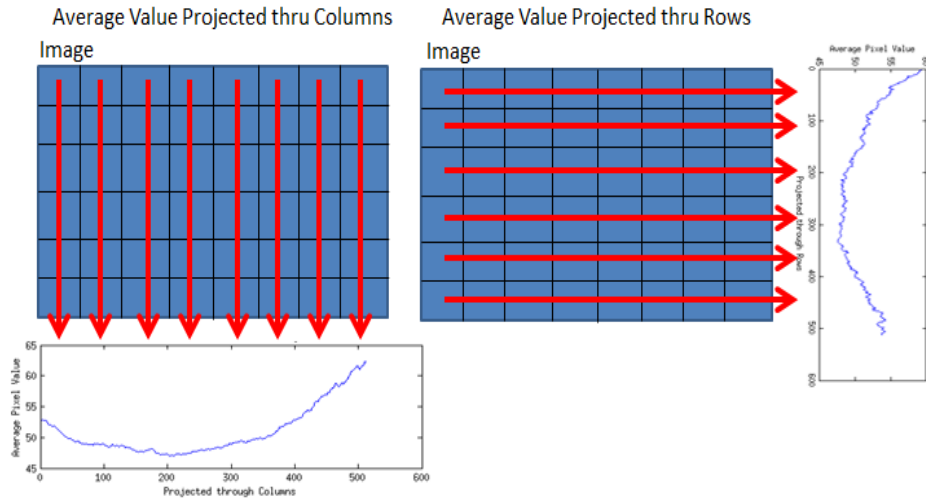


Figure 2-9: In-Plane Correction X & Y Profiles

The x profile (Left) is created by projecting an average value down the columns of the image. The y profile (Right) is created by projecting an average value across the rows of the image. This technique is used both in the algorithm for correcting images as described by Hovhannisyanyan et al. and to measure corrected image tiles from the ideal “flat” profile[37].

	Dataset 1		Dataset 2		Dataset 3	
	X-profile Error	Y-profile Error	X-profile Error	Y-profile Error	X-profile Error	Y-profile Error
Raw Data	15.59	7.37	0.64	0.52	0.79	4.34
Chow	2.23	1.13	0.001	0.001	0.002	0.01
Hovhannisyan	3.79	2.84	0.049	0.076	0.25	0.12

Table 1: Comparing In-Plane Correction Algorithms

Chow vs Hovhannisyan in-plane correction efficacy comparison. Three separate datasets were used for comparison. Chow outperformed Hovhannisyan each time.

Following in-plane tile intensity correction, adjacent image tiles for a particular z value are rigidly aligned, in a process known as stitching, into a single image, see Figure 2-7C. This stitched image for a single z value is referred to as an image slice. Each tile is aligned on the output image slice according to the stage coordinates recorded during acquisition of that tile. Each intercut volume (except for the topmost and bottommost volume) will have image slices at the top and bottom of the z range that have been imaged twice (due to the cut step being smaller than the optical stack depth). In these overlapping regions, both sets of images collected will be stitched for image registration done later; however, the images at the top of the optical stack obtained after cutting will be used in the final image volume rather than the corresponding images at the same z value at the bottom of the optical stack prior to the cut. This is done for two reasons: 1) while the signal attenuation with depth will be corrected (see below), this is not a perfect correction, and the lower images in an optical stack will be somewhat dimmer than the top of the stack, and 2) the point spread function will increase with imaging depth, meaning the images closer to the surface will have better image quality than the deeper images.

To align intercut volumes, the image slices collected at the same position in the sample (before and after the cut) are co-registered, Figure 2-7D. Two image slices acquired at the same z -value are registered with a Nelder Mead Simplex optimization [38] adjusting the x, y offset to minimize the cost function in Equation 2.

$$C(x, y) = 1 - NCC(I'_1(x, y), I'_2(x, y)) \quad (2)$$

In this equation, x and y represent the offset in coordinates of the first image slice acquired (I_1) and the second image slice acquired (I_2), as shown in Figure 2-7D. NCC is the normalized cross correlation of the two input images. I_1' is the portion of I_1 overlapping I_2 with offset x and y , and I_2' is the portion of I_2 overlapping I_1 with offset x and y as shown by the dashed line in Figure 2-7D. This registration method is robust to differences in image intensity[39]. The x,y offsets are determined in this way for each error-inducing cut step. Once the offsets between each intercut volume are determined, the stitched image slices are adjusted on their templates to bring the image slices into alignment.

Following image registration, overlapping image slices are compared in order to select the images acquired closer to the surface of the sample. Because the signal attenuates with increasing imaging depth, the pixels at corresponding coordinates on the overlapping image slices are compared, and the brightest (or maximum pixel intensity) is selected for the final image slice as this corresponds to the imaging position closest to the surface of the sample. This method is preferable to assuming the location of the image in the optical stack because of the cutting error that manifests during long acquisitions as shown in Figure 2-6.

Signal attenuation with depth results from scattering and absorption both of the incident and reflected photons. Images acquired from deeper in the sample will be more attenuated than those acquired closer to the surface. Therefore image depth intensity correction must be performed, Figure 2-7E. Many approaches have been developed to perform this correction [40-42]. Because of the relatively large depth of the optical stacks collected by the AVIM, it is necessary to have a correction method that is robust and

insensitive to the noise that is inherent in images acquired at large depths. After testing three separate algorithms [40-42], a mixture modeling algorithm by Gopinath et al. was found to work the best. Briefly, the mixture modeling algorithm takes the aligned image slices and labels the brightest image slice as the reference image. It then assumes the image has two components in its histogram of pixel intensity, a foreground component and a background component. The expectation-maximization algorithm is used to segment pixels into foreground and background classes by iteratively defining the probability each pixel intensity has of belonging to either class and calculating the mean and standard deviation of each class with such memberships. This process of finding the foreground and background information is repeated for the other image slices in dataset. The non-reference images are then adjusted so that the parameters of their foreground component more closely resemble those of the reference image. The algorithms considered were evaluated based on their ability to restore pixel intensity with increasing depth as well as preserve image specific features. In regards to preserving pixel intensity with depth, Lee's mean-weight filtering technique[42] outperformed all others; however the resulting corrected images amplified noise that obscured the relevant structures of interest. An example is shown below in Figure 2-10. Of the two remaining algorithms, Gopinath's mixture modeling algorithm was superior in both restoring pixel intensity (an objective measure) as well as preserving image quality (a subjective measure). Refer to Figure 2-10 for an example of this depth correction using the Gaussian mixture model algorithm.

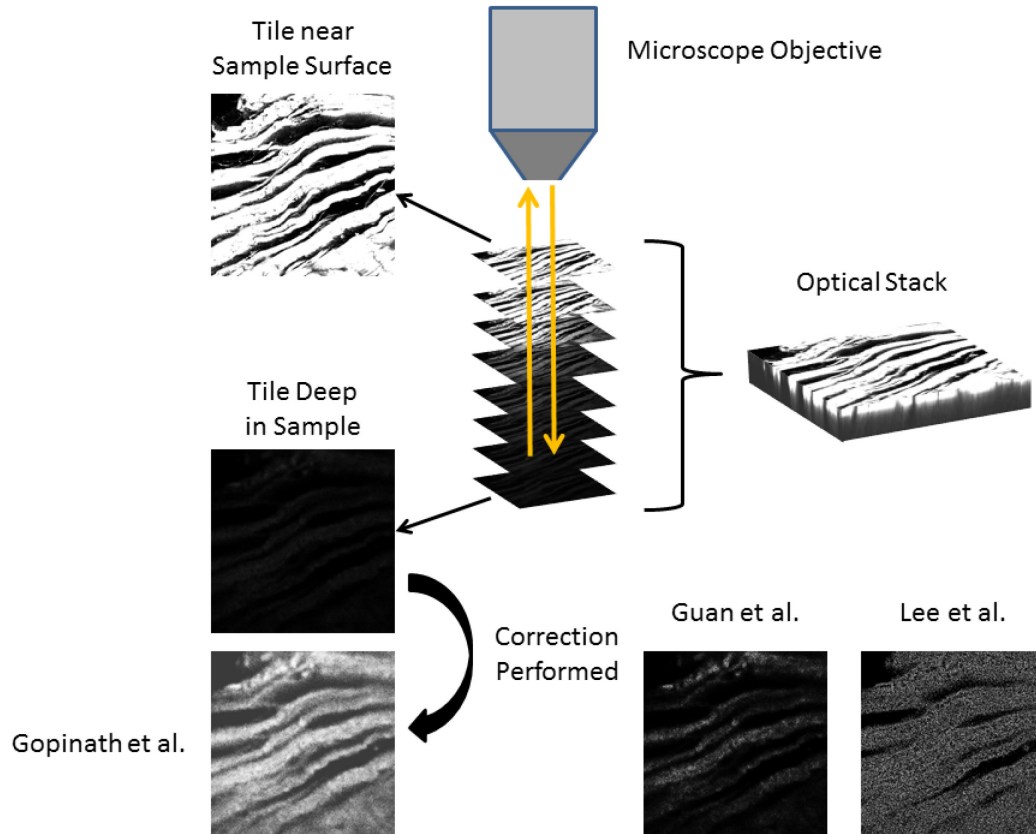


Figure 2-10: Depth Correcting Acquired Images

When an optical stack is acquired, photon scattering and absorption (both incident and excited) will attenuate signal intensity. This attenuation increases with increasing focal plane depth. Tiles acquired deeper in the tissue are corrected so that their intensity more closely matches tiles acquired near the surface. Three algorithms were considered [40-42], and Gopinath et al. was found to have the best performing for our application.

2.1.5 Image Volume Reconstruction and Visualization

The acquired images from a complete mouse heart acquisition were corrected and reconstructed on an IBM iDataPlex cluster using 4 nodes, each with 2 Intel Xeon E5472 3.00GHz Quad-core processors and 32GB RAM. Correction and reconstruction took roughly 10 days. This reconstruction is embarrassingly parallel and computational time will decrease approximately linearly with additional compute nodes. The final volume was 4968 x 4968 x 566 pixels occupying 14GB of space uncompressed and roughly 7GB in PNG format.

The large size of the image volume presents a challenge in rendering the volume for 3D visualization. When using ImageJ, datasets need to be downsampled to a fraction of their original size so that the PNG files can be imported and rendered with the plugins VolumeViewer and 3DViewer [43]. To view larger datasets at full resolution, we have used ImageVis3D (Scientific Computing and Imaging Institute, Salt Lake City, Utah) which allows the dataset to be read directly from the hard drive for visualization of datasets much larger than the physical memory available. Both ImageJ and ImageVis3D are open source, freely available software packages that are compatible with the output of the AVIM software pipeline.

2.2 Results

Several mouse hearts were labeled, imaged, and visualized in order to investigate the cardiac architecture in the heart using the AVIM. Figure 2-11 shows a mouse heart that was mounted in paraffin so that cutting was perpendicular to the long axis of the heart. The different panels in the figure demonstrate the versatile nature of the reconstructed

image volume. The whole heart is rendered in 3D using ImageJ in Figure 2-11A. Arbitrary virtual cut planes can be defined using the VolumeViewer plugin in ImageJ so that the interior cardiac structure can be viewed approximately halfway between the epicardium and endocardium of the left ventricle (LV) anterior wall in Figure 2-11B. These 3D renderings are composed of reconstructed image slices, an example of which is shown in Figure 2-11C. Figure 2-11D is the enlarged view of the region in the yellow box in Figure 2-11C. The image volumes shown in Figure 2-11 have an in-plane resolution of 1.6 μm and an out-of-plane resolution of 10 μm .

The image seen in Figure 2-12A is another view of the image volume in Figure 2-11 where the virtual cut-plane has been adjusted so that a portion of the anterior left ventricle wall was removed. Cardiac sheet structure, originally demonstrated in canine tissue [45], can be observed from a transmural perspective in this image, along with trabecular structure within the ventricle. The sheets start at the base of the heart, progress vertically downward then change orientation by almost 90 degrees to project radially through the LV wall. This is illustrated by a series of red arrows following the sheet structure across the wall of the heart in Figure 2-12A.

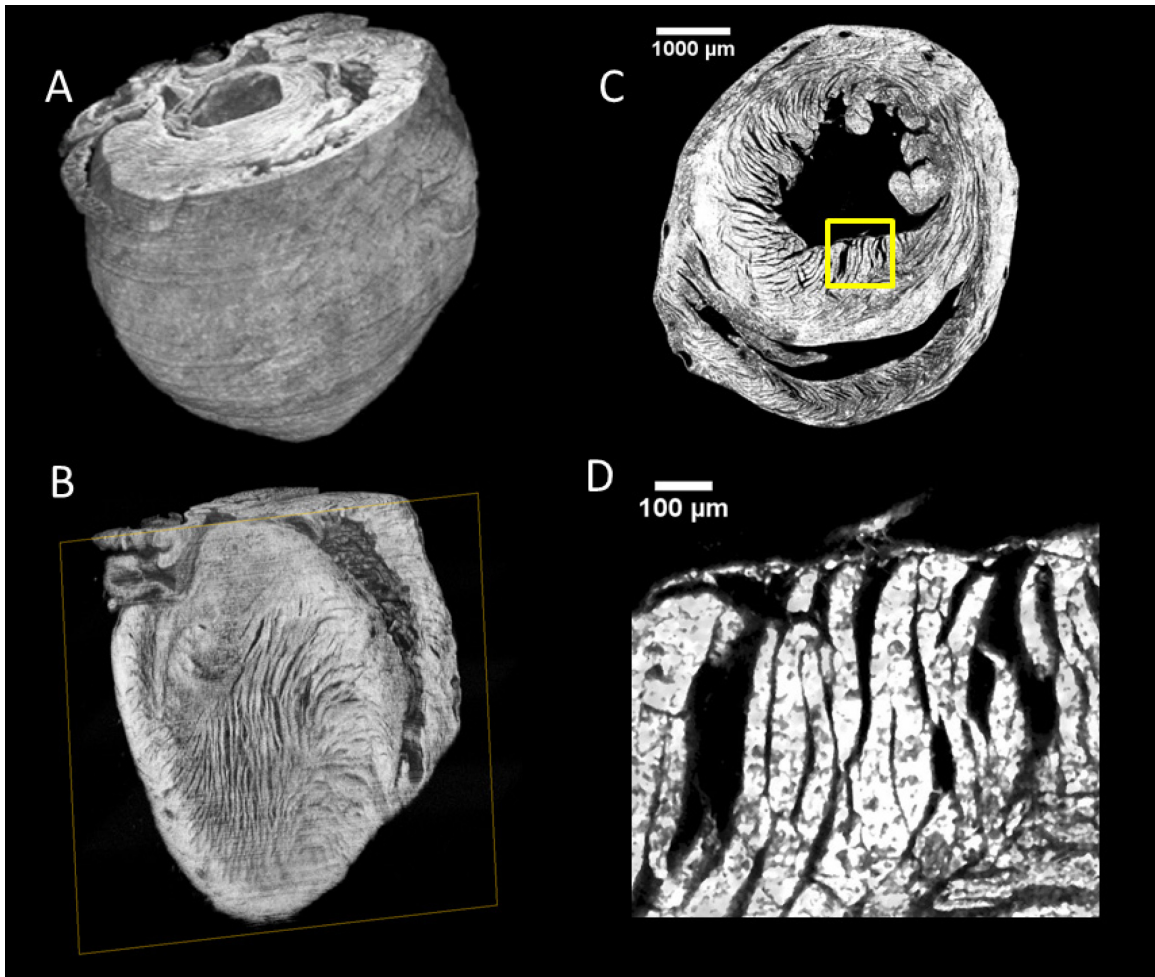


Figure 2-11: Image Volume 3D Rendering and Virtual Cut Planes - Mouse Heart

(A) Complete 3D volume of mouse heart ventricles rendered with ImageJ Volume Viewer. (B) A generated virtual cut plane demonstrating the cardiac architecture in the left ventricle. (C) A transverse image slice depicting the original plane of sectioning and imaging. (D) A small portion of the slice, highlighted in C, showing the finer detail of the endocardium.

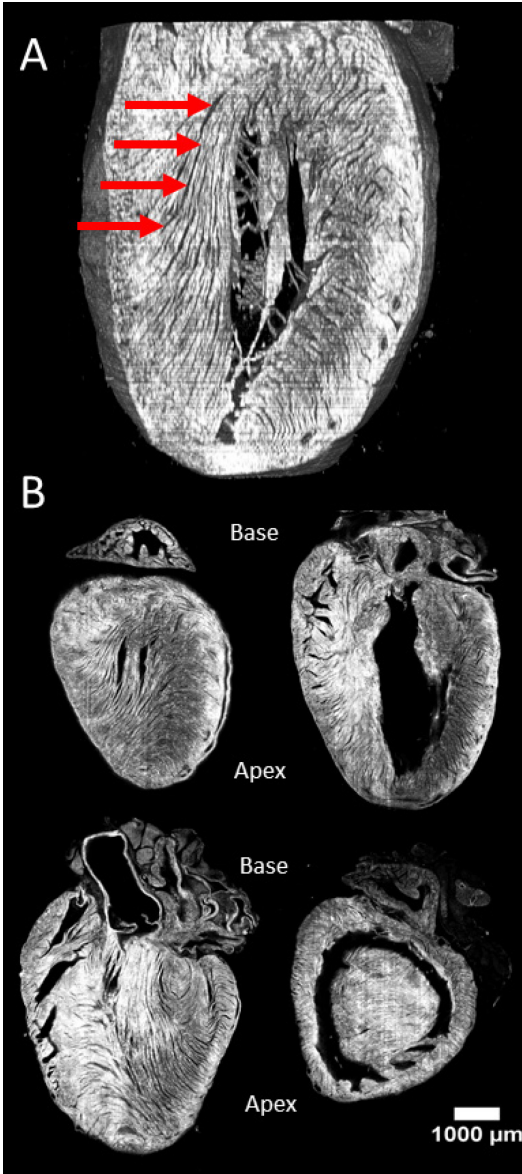


Figure 2-12: Fiber Structure in Mouse Heart - Virtual Cut Planes

(A) A virtual cut plane from the mouse heart in Figure 2-11 chosen to demonstrate the sheet structure in the mouse left ventricle. The red arrows follow a sheet through the wall of the heart. (B) Representative image slices from a mouse heart that was embedded so that cutting was parallel to long axis of heart. The base and apex in the heart are labelled for orientation.

One mouse heart was embedded so that the cutting axis was parallel to the long axis of the heart, providing higher resolution image slices along the sagittal plane, shown in Figure 2-12B. The panel shows images that are parallel to each other and taken at different depths, roughly 1 mm apart from each other. This embedding orientation enabled measurement of transmural fiber inclination angle through the right and left ventricular walls. Figure 2-13A and Figure 2-14A shows a view of the left and right ventricular epicardial surface respectively. It can be seen that cardiac fibers have different orientations depending on surface location. The angle (relative to the circumferential direction) formed by projection of this orientation onto the epicardial tangent plane is known as fiber inclination angle[46]. The Directionality plugin in ImageJ was used to compute the fiber inclination angle at distinct regions in each of the ventricular walls. Briefly, this algorithm assumes fiber angle will be perpendicular to the local pixel intensity gradient at locations throughout the image. The gradient is calculated using a 5x5 Sobel filter for each pixel within the image, and the local gradient will be defined as the most commonly occurring angle within the image. Two locations were selected on each of the ventricular walls 800 μm by 800 μm in size for analysis, and fiber inclination angle was calculated at for each step in z, 10 μm . The results can be seen in Figure 2-13B and Figure 2-14B respectively.

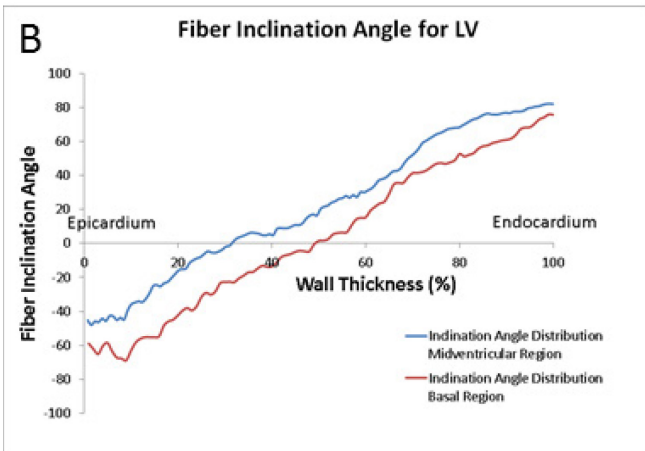
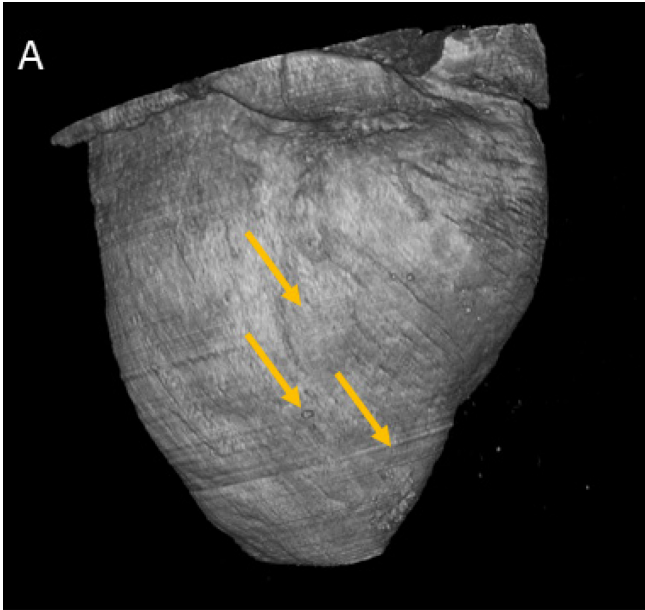


Figure 2-13: Fiber Inclination Angle for Mouse Left Ventricle

(A). Example of the epicardial surface demonstrating the orientation of the cardiac fibers and their inclination, in the direction of the yellow arrows. (B) Fiber inclination angle was measured at two locations (red and blue) through the wall of the left ventricle. There is a counter-clockwise rotation in the measured fiber inclination angle traveling in the epicardium to endocardium direction.

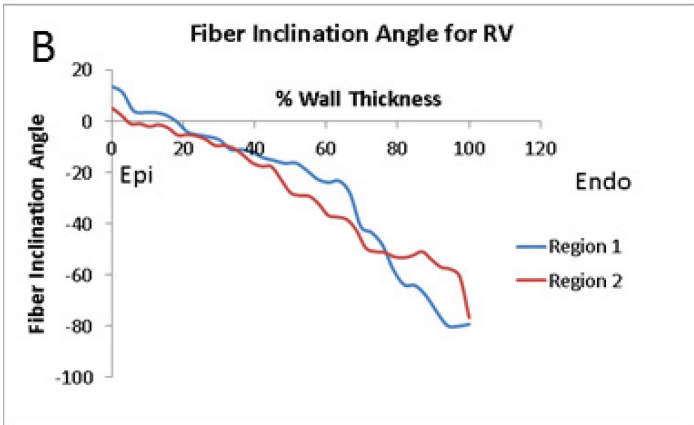
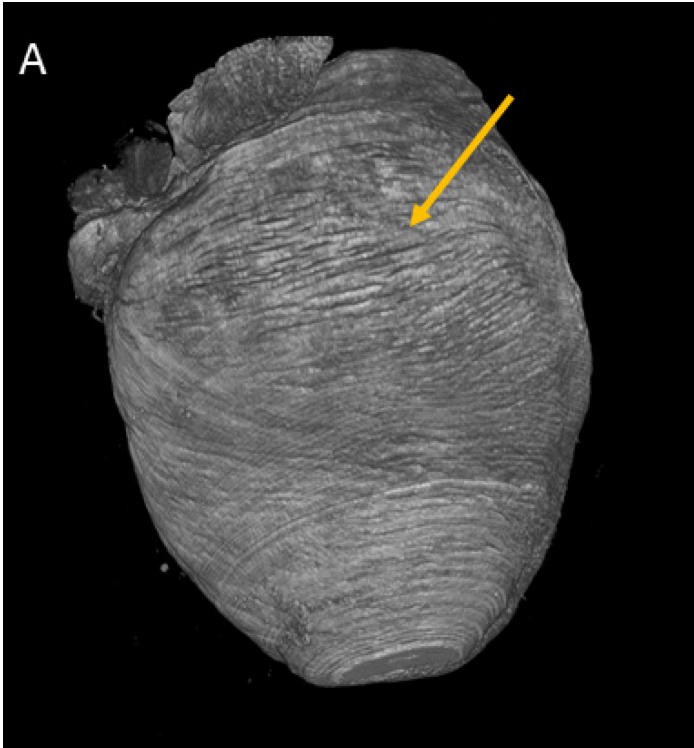


Figure 2-14: Fiber Inclination Angle for Mouse Right Ventricle

(A) Epicardial surface of the right ventricle, shown by the yellow arrow, showcasing almost circumferential organization of myofibers. (B) Fiber inclination angle measured at two locations through the wall of the right ventricle. There is a clockwise rotation in the measured fiber inclination angle, opposite to that observed in the left ventricle.

While diffusion tensor MR imaging (DTMRI) has been able to produce a better resolution for measurement of fiber inclination angle, we can achieve that by the use of a higher resolution objective. Also, we achieve a much better depth increment (10 microns) as compared to DTMRI ($>100\ \mu\text{m}$) typically. The plot of fiber inclination angle as a function of percent distance from the epicardium to endocardium has positive slope. The epicardium has negative angles, fibers in the mid-myocardium are aligned in a circumferential direction (0 degrees) and in endocardium angles are positive. This profile agrees with those obtained using anatomic reconstruction [46] and DTMRI[47, 48].

Fiber inclination angles were also calculated as a function of distance through the RV wall. Unlike the LV wall, the plot of inclination angle as a function of percent distance from epicardium to endocardium (Figure 2-14B) has negative slope. As shown in Figure 2-14A cardiac fibers on the epicardium of the RV can have an approximately circumferential orientation (0 degrees). To our knowledge, fiber orientation in the RV has not been measured using either anatomic or imaging-based approaches for mouse. This is likely due to the small thickness of the RV wall.

Closer inspection of the image slices from this heart revealed interdigitation of the sheet structure near the endocardium, seen in Figure 2-15A. Panel B in the same figure is an enlargement of the area in the box in panel A. This result shows what was originally hypothesized by Arts et al. [49].

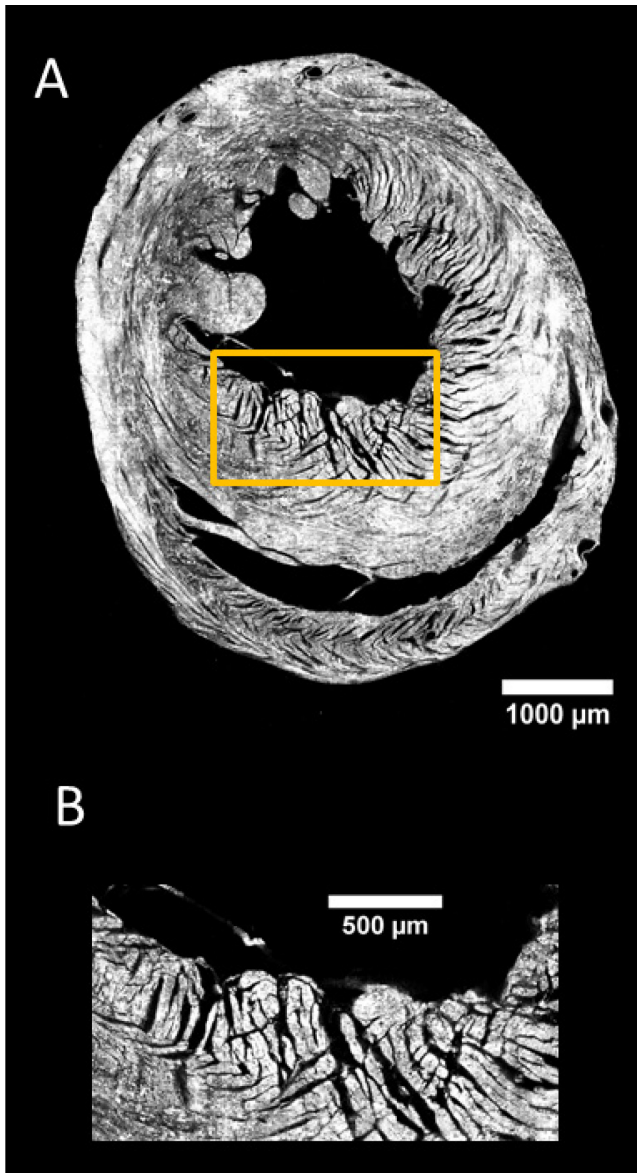


Figure 2-15: Interdigitation of Sheets in Mouse Left Ventricular Endocardium

(A) An image slice from a mouse heart embedded so that cutting was perpendicular to the long axis of the heart. The yellow box shows the region of the endocardium demonstrating interdigitation of cardiac sheet structure, something hypothesized by Arts et al. [49]. (B) The region in the yellow box in (A) enlarged to depict clear interdigitation in the endocardium.

2.3 Discussion

The modular and low cost design of the AVIM reduces the barriers to entry for automated laser scanning microscopy of large tissue volumes. Two-photon and confocal microscopes are often shared resources. Our goal was to design a portable macro-scale high spatial-resolution tissue reconstruction system that can be used on shared instrumentation. We demonstrate the ability of such a system to obtain high quality image volumes in macro-scale tissue samples. We provide detailed plans for the construction and use of the AVIM so that others may reproduce this hardware; see Appendices.

The low cost and portability design constraints for the AVIM necessitated the use of more compact and less precise instrumentation than has been used by other groups. In order to compensate for this, computational methods are applied to the acquired images during several post-processing steps in order to correct, register, and visualize a high quality, high spatial-resolution image volume. The software pipeline developed for the reconstruction of the acquired images into an image volume is provided in Appendices.

The great potential of automated LSM as a tool in biomedical research is its ability to visualize the imaged sample in arbitrary cut planes. This provides the capability to visually explore and obtain greater insights into biological phenomena. Previous studies have demonstrated the importance of automated LSM. Several studies have focused on the organization of cardiac myocytes in fibers and sheets [34, 50, 51], which greatly expanded on studies using diffusion tensor magnetic resonance imaging (DTMRI) to measure these structures. The reliance on an indirect measure of cardiac structure is a major limitation of DTMRI, one that can be overcome with new methodology since

automated LSM has adequate resolution to measure and visualize cardiac structure directly. The result of these studies regarding cardiac structure provided a known biological template to compare and validate the results gathered with the AVIM. The fiber inclination angles computed from the images obtained were validated against histological and DTMRI studies [46, 48]. We have also used the AVIM to collect novel information including fiber inclination angle through the RV wall and the interdigitation of sheets in the LV, the latter of which was hypothesized by Arts et al. [49]. We wished to briefly demonstrate one of the many possible applications of the AVIM. Measuring fiber angle through the RV and LV is only part of what can be learned from the reconstructed image volumes. Accordingly, the mouse heart image volumes acquired and reconstructed for this study will be made available in the Cardiovascular Research Grid Database, <http://www.cvrg.org>. Going forward, many more applications for automated LSM exist that could be explored through a more accessible means of implementation.

A limitation to our work on designing and disseminating the AVIM and the associated software pipeline is the specificity for a Zeiss 7MP microscope. This leaves to the end user two main tasks to adapt the designs to other microscope system: 1) establishing a reliable communication protocol between the AVIM and their microscope and 2) loading the proprietary image files (in the case of Zeiss, “.lsm” files) into the software pipeline. We have taken care to highlight these portions of the acquisition and reconstruction code where necessary changes would be made for use with other microscope vendors. Other limitations of the AVIM arise primarily from constraints on the design of the AVIM in keeping with the low cost and modular requirements. First and foremost, when using steel microtome blades the sample must be fixed and embedded in paraffin, an

embedding media known to quench the fluorescent signal of dyes [35]. Other embedding media were considered based on protocols developed in other labs [34, 35], but ultimately ruled out due to the added complexity and cost. We have found that adequate signal intensity can be achieved even with paraffin embedding, Figure 2-11. A second limitation of the AVIM is the maximum sample size of roughly 1 inch in each dimension constrained by the travel of the stage. A third constraint is the acquisition time required for a sample. For the mouse hearts presented here, image acquisition required 5 days on the microscope. The maximum sample size would allow for over a month of image acquisition time with a z-step of 10 μm , considerably more with a smaller increment in z. Since this instrument is intended for a shared microscope, limitations on imaging time rather than sample size will be the main constraint.

The AVIM design represents a trade-off between hardware investment (both the instrument itself as well as a laser scanning microscope) versus image processing. The design allows for an adequate acquisition of a sample, and the accompanying software pipeline to apply the necessary corrections in order to produce a high quality image volume. As further developments are made in the field of image processing, upgrades can be applied to the reconstruction process for continued refinement of the output image volume.

Chapter 3 - Spatial Properties of Metabolic Sinks and Their Relationship to Ischemia Reperfusion Arrhythmias

As discussed in Chapter 1, the endocardium consumes oxygen at a higher rate and is exposed to more strain than the epicardium putting the endocardium at a disadvantage when exposed to a metabolic stress [10, 18-21]. Because of this, we hypothesize that endocardial tissue may be more susceptible to IR injury than other myocardial regions. To test this hypothesis, we have developed an approach to label and image polarized mitochondria throughout a GP heart. We first expose the heart to an IR injury. During reperfusion we perfuse the heart with Mitotracker Red CMXRos (MTR) (Molecular Probes, Eugene, OR), a dye that loads into mitochondria with polarized ψ_m and is retained upon fixation. Following fixation and embedding, the AVIM (described in Chapter 2) is used to section and image the heart. This protocol provides a snapshot in time of the polarized mitochondria throughout the GP heart and provides more insight into the effects of IR injury on the heart as a whole. We apply this protocol to test our hypothesis that the endocardium is more strongly affected by IR injury than the epicardium due to the different micro-environments of the two regions.

3.1 Methods

3.1.1 Sample Preparation

All surgical protocols are approved by the Animal Care and Use Committee of the Johns Hopkins University. Adult male guinea pigs between 300-700 g in weight and 4-12 weeks old in age are anesthetized with sodium pentobarbital (35 mg/kg, i.p. injection). The heart is rapidly excised and transferred to a Langendorff perfusion apparatus. The

heart is perfused at 70-80 mmHg constant pressure with Tyrode's solution heated to 37 °C (in mM): 118 NaCl, 24 NaHCO₃, 1.2 KH₂PO₄, 4.75 KCl, 1.2 MgSO₄, 2.0 CaCl₂, and 10 glucose (equilibrated with 95/5 %O₂/CO₂). Perfusion is maintained for 20 minutes to allow the heart to stabilize. During this time, ECG leads are placed to allow for monitoring during the protocol and to ensure normal rhythm during the stabilization phase. A video camera is setup near the perfusion apparatus so that the initial period of each portion of the perfusion protocol can be recorded.

In order to induce global ischemia, the perfusion pump is turned off, halting any perfusion pressure/flow to the heart, for 30 minutes. This length of global ischemia was determined from the literature to both induce mitochondrial depolarization but still allow for recovery in the reperfusion phase [4, 6, 8, 52-55]. During global ischemia, the bath around the heart is bubbled with nitrogen gas to displace oxygen from the Tyrode's solution.

Following the period of global ischemia, the heart is reperfused with Tyrode's solution at a constant pressure of 70-80 mmHg for 5 minutes. Other studies have found that there is a dynamic period of mitochondrial polarization immediately upon reperfusion, which will eventually stabilize after 5 minutes [8, 56].

At 5 minutes of reperfusion with normal Tyrode's solution, the perfusate is switched to a Tyrode's solution containing 1 μM Mitotracker Red CMXRos (MTR) and 15 nM Hoechst 33342 (Molecular Probes, Eugene, OR) for 10 minutes to fluorescently label the heart. Hoechst stain is a fluorescent indicator that labels nucleic acids in the nucleus. Here, we use Hoechst staining to assess the extent of myocardium that is perfused with

fluorescent indicator. The combination of fluorescent markers allows for the demarcation of perfused tissue with polarized mitochondria (fluorescent signal in both blue and red channel), and perfused tissue with depolarized mitochondria (fluorescent signal in blue channel and no signal in red). Excess dye is washed out of the heart by switching the perfusate to the normal Tyrode's solution for an additional 5 minutes.

The heart is removed from the perfusion apparatus, and cold cardioplegic solution containing (in mM) potassium glutamate 120, KCl 25, MgCl₂ 1, HEPES 10, EGTA 1 is perfused through the heart for 5 minutes using a manual syringe. This perfusion ensures the heart is in a state of diastole for fixing. The heart is then perfused and superfused for 10 minutes with methanol chilled to -20° C. To ensure good fixation, the heart is submerged in chilled methanol for an additional 10 minutes. We find that methanol fixation helps reduce the autofluorescence of cardiac tissue.

The heart is rinsed twice in phosphate buffered solution (Life Technologies, Grand Island, NY). Then the heart is dehydrated with a graded ethanol, xylene series (ethanol 80% / 95% / 95% / 100% / 100%; xylene 100% / 100%; 1 hour each at 40° C) immediately followed by immersion in paraffin (4 immersions of 1 hour each at 60° C); all steps are performed under negative pressure and agitation. The heart is then embedded in a paraffin block with a standard mounting cassette. A total of 10 hearts were processed through this protocol for use in this study.

3.1.2 Image Acquisition

Each heart is mounted on the automated volume imaging microtome (AVIM), see Chapter 2 for full description. Briefly, the AVIM uses an automated high resolution 3D

stage in combination with an automated microtome to sequentially image throughout a macroscopic sample embedded in paraffin. Before imaging, the microtome is used to repeatedly section the heart until the exposed surface includes the full base-apex axis (cutting to approximately halfway through the paraffin block). At this point, the surface of the sample is imaged with a 10X Apochromatic C lens on a Zeiss 7MP microscope interfaced with the AVIM. Excitation wavelength is set to 780 nm, a setting determined from the control samples deemed sufficient to excite both the Hoechst and MTR dyes. Images are recorded in the red channel and blue channel for the MTR and Hoechst signal respectively. The AVIM positions the sample beneath the objective and acquires an image, referred to as an image tile. This process of positioning the sample beneath the objective and acquiring an image tile is repeated until the entire sample surface is imaged. The individual image tiles collected over the sample surface are corrected for imaging artifacts [36, 40] and are rigidly aligned using the 3D stage coordinates set during image acquisition to correctly position the image tiles into an image slice. This produces a high quality cross section of the GP heart as seen in Figure 3-1.

3.2 Results

In order to validate the labeling protocol, two control hearts were processed. The positive control or no-ischemia heart had perfusion pressure maintained throughout the protocol described above. This heart, seen in Figure 3-1A, shows a uniform labeling of the tissue both in the blue channel, indicating adequate perfusion of the tissue, and in the red channel, indicating polarized mitochondria throughout the heart. The negative control heart was treated with 5 mM cyanide and 5 μ M oligomycin during the reperfusion phase in order to uncouple the electron transport chain and depolarize the mitochondria in the

heart. The negative control heart can be seen in Figure 3-1C. A global threshold value was determined so that the signal in the positive control heart was preserved. This threshold was varied within 30% of its value; findings of significance discussed below persist throughout this range of thresholds. The positive and negative control hearts were segmented using this value in Figure 3-1B & Figure 3-1D respectively.

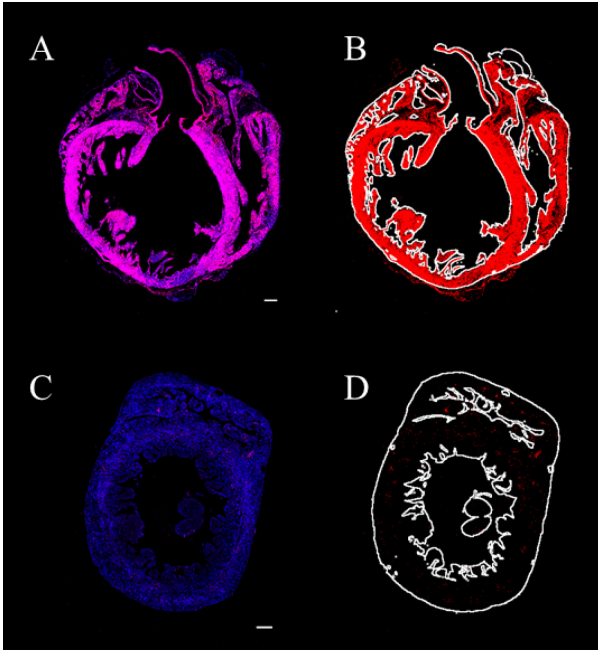


Figure 3-1: Guinea Pig Control Hearts with Hoechst and Mitotracker

(A) Sagittal section of heart treated without ischemia; scale bar is 1 mm. (B) Segmented Mitotracker signal for the heart in A. (C) Axial section of heart treated with oligomycin and cyanide during reperfusion; scale bar is 1 mm. (D) Segmented Mitotracker signal for the heart in C.

The cross sections acquired for the 10 GP hearts exposed to the ischemia-reperfusion protocol along with a representative ECG waveform recorded during the reperfusion phase can be seen in Figure 3-2, Figure 3-3, and Figure 3-4 panels A and C. Each heart was segmented using the global threshold defined in the control hearts. In addition to the segmentation step, signal in the blue channel was used to define the boundaries of the myocardium so that areas of depolarized mitochondria can be inferred from the lack of signal in the red channel; see Figure 3-2, Figure 3-3, and Figure 3-4 panel B.

If we define recovery from IR injury as regaining a rhythmic ECG waveform, then 6 out of the 10 hearts recovered from the IR injury (Figure 3-2 & Figure 3-3), and 4 out of the 10 hearts have sustained arrhythmia following reperfusion (Figure 3-4). Of the 4 hearts exhibiting sustained arrhythmia, each have depolarized mitochondria in or near the endocardium and polarized mitochondria in or near the epicardium, producing a sharp gradient in ψ_m across the left ventricular wall; see Figure 3-4. Because this pattern of ψ_m was seen in all the hearts that displayed sustained arrhythmia upon reperfusion, this appears to be a necessary condition for sustained reperfusion arrhythmia. However, the same pattern of mitochondrial depolarization appears in 3 of the 6 hearts that regained a rhythmic ECG, Figure 3-2, suggesting that this pattern of depolarization is not a sufficient condition for sustained arrhythmogenesis and other factors are at play.

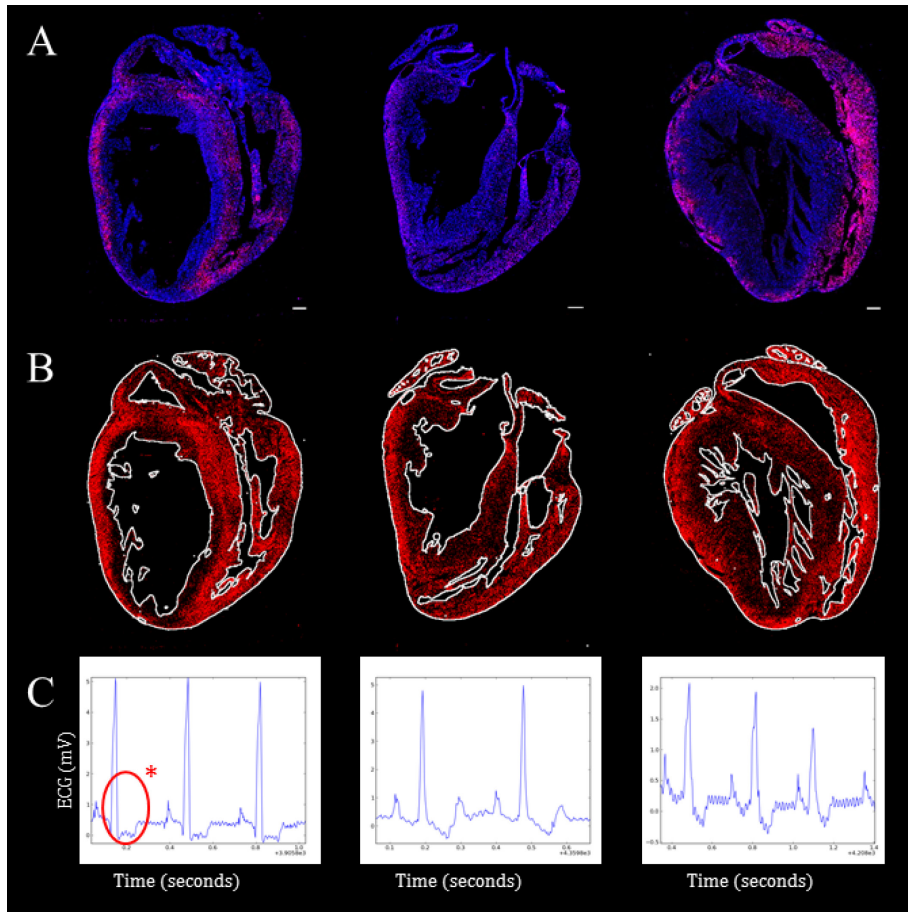


Figure 3-2: GP Hearts Rhythmic Beating with Transmural Bias

Three of the six GP hearts exposed to IR injury protocol that recovered a rhythmic ECG displayed depolarized ψ_m in and/or near the endocardium. (A) Cross sections were acquired for each heart using the AVIM; scale bar is 1 mm. (B) Segmented MTR signal from the raw images in A. The Hoechst signal was used to define the boundaries of the heart, shown in white. (C) Recorded ECG during the reperfusion phase for each heart. The profile of recovery can be predicted from the ECG. The ECG from a recovery heart with a depolarized endocardium shows a depressed ST segment with little or no T wave, indicated in the first ECG with a red circle and asterisk.

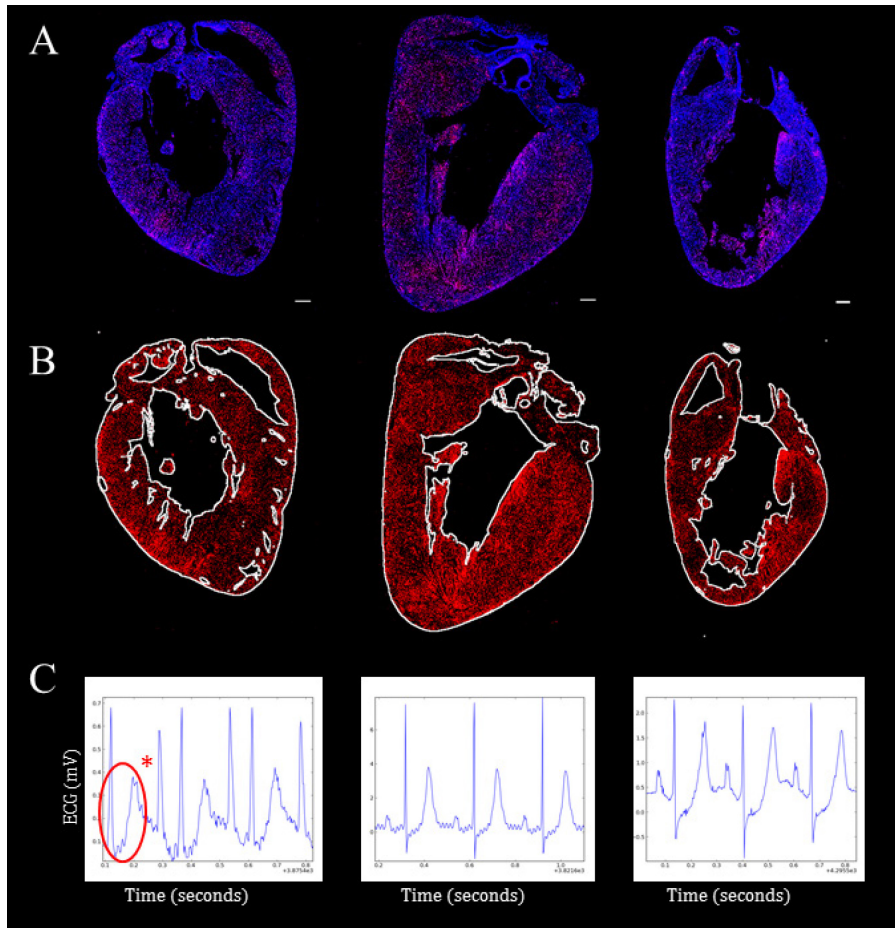


Figure 3-3: GP Hearts Rhythmic Beating without Transmural Bias

Three of the six GP hearts exposed to IR injury protocol that recovered a rhythmic ECG and displayed polarized ψ_m both in the epicardium and endocardium. (A) Cross sections were acquired for each heart using the AVIM; scale bar is 1 mm. (B) Segmented MTR signal from the raw images in A. The Hoechst signal was used to define the boundaries of the heart, shown in white. (C) Recorded ECG during the reperfusion phase for each heart. The profile of recovery can be predicted from the ECG. The ECG from a recovery heart with uniform recovery shows a depression of ST segment but a large upright T wave, indicated in the first ECG with a red circle and asterisk.

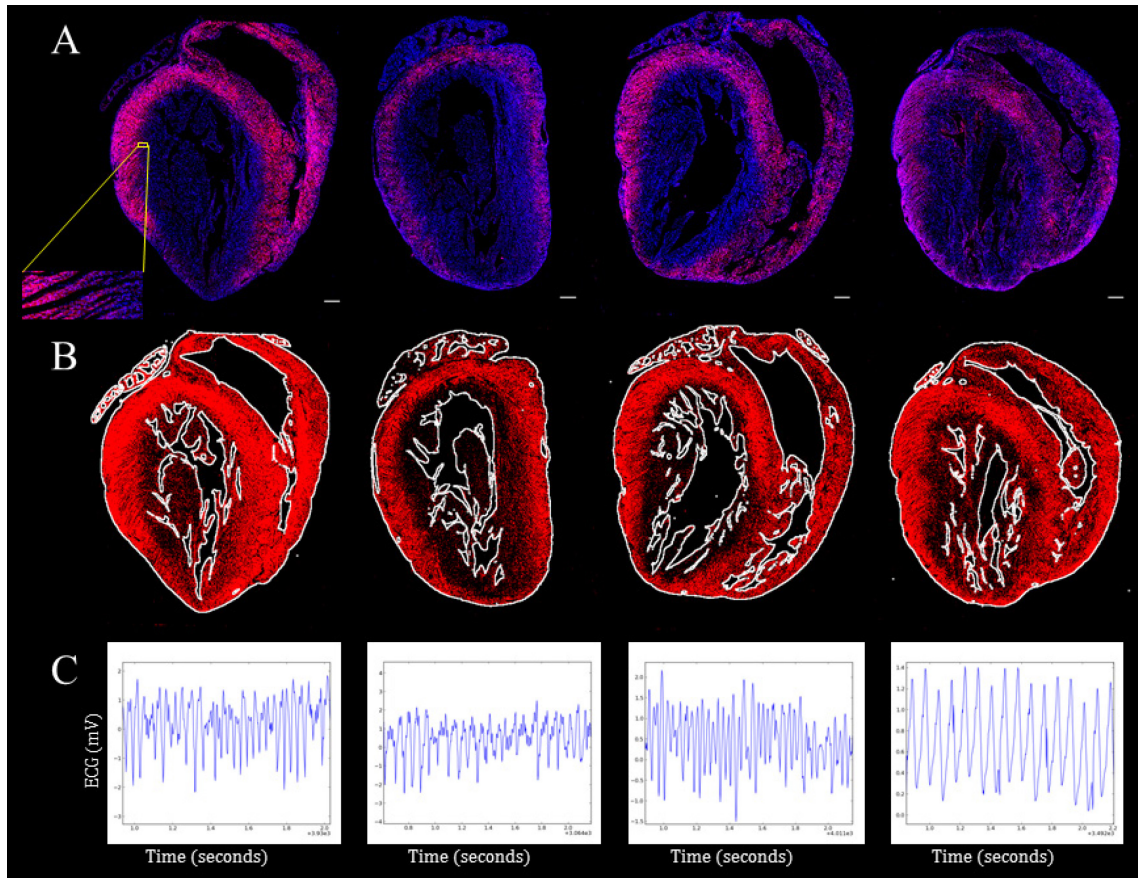


Figure 3-4: GP Hearts Sustained Reperfusion Arrhythmia

Four of the ten GP hearts exposed to IR injury protocol that did not recover rhythmic ECGs. (A) Cross sections were acquired for each heart using the AVIM; scale bar is 1 mm. The region selected in yellow is enlarged to show the detail acquired in these images. (B) Segmented MTR signal from the raw images in A. The Hoechst signal was used to define the boundaries of the heart, shown in white. (C) Recorded ECG during the reperfusion phase for each heart.

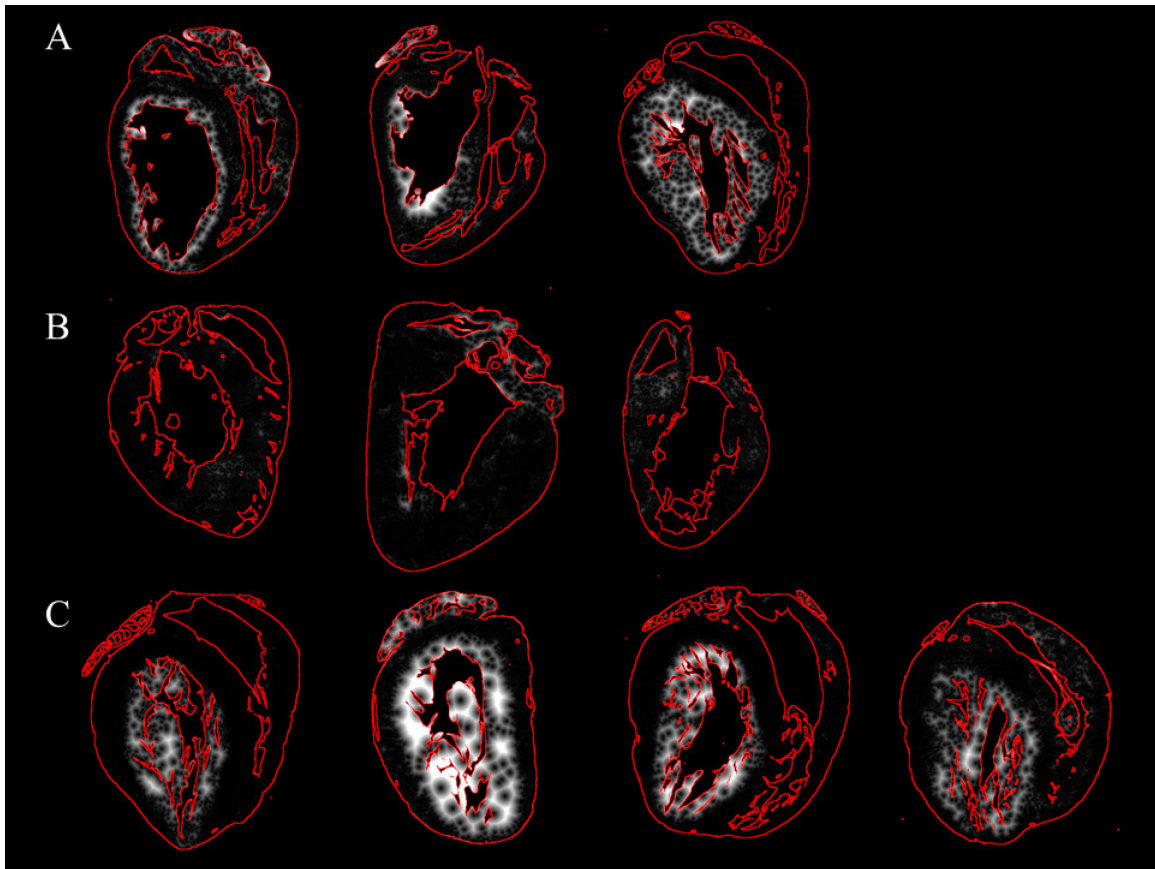


Figure 3-5: Euclidean Distance Mapping to Polarized Pixels

The Euclidean distance was calculated from each pixel classified as depolarized to the nearest polarized pixel. The intensity in white corresponds to this distance, higher intensity indicates that depolarized pixel is farther away from a polarized pixel. (A) Hearts regaining rhythmic beating with a depolarized endocardium. (B) Hearts regaining rhythmic beating with a uniform polarization across the myocardium. (C) Hearts displaying a sustained arrhythmia upon reperfusion.

It is only in the remaining 3 hearts that regained a rhythmic ECG (Figure 3-3) where both the epicardium and endocardium have a sparse uniform distribution of mitochondria with recovered (polarized) ψ_m , a profile that we refer to as uniform recovery. The Euclidean distance between a pixel classified as depolarized and the nearest polarized pixel was calculated for the 10 hearts, see Figure 3-5. The higher pixel intensities indicate that depolarized pixels are farther away from a polarized pixel. This demonstrates the depolarized endocardium in 7 of the 10 hearts, Figure 3-5A & C. Whereas the hearts with more uniform distribution of polarized mitochondria, Figure 3-5B, shows very low pixel intensities, or short distances between polarized tissue. When the ECG's are compared between the two subgroups within the recovery hearts (uniform recovery and depolarized endocardium), we observe a difference in the ST segments and T waves between the two. The hearts with depolarized ψ_m in and/or near the endocardium have a depressed ST segment and little or no T wave, see Figure 3-2C (red indicator), as compared to those hearts with uniform ψ_m polarization throughout the myocardium, see Figure 3-3C (red indicator). This difference in ECG agrees with what is observed clinically, where a more severe ischemia will display an ECG similar to the hearts with depolarized mitochondria in the endocardium [57, 58].

A surprising result is the difference in the amount of tissue containing polarized mitochondria between the three different profiles observed. The recovery hearts with no transmural bias (endocardium and epicardium show similar amounts of polarized mitochondria) show sparse regions of polarized mitochondria throughout the left ventricle as compared to the epicardium of the remaining hearts (both recovery and arrhythmia hearts) with a transmural bias (epicardium more polarized mitochondria than

endocardium). In order to measure this difference, the region of the left ventricle with polarized mitochondria is selected for each heart; see Figure 3-7 for the selected region of each heart. Within these selected regions, the amount of tissue segmented as polarized is measured with respect to total amount of tissue within the selected regions. The results are reported as percentage of the selected tissue with polarized mitochondria, see Figure 3-6. Surprisingly, the recovered hearts displaying polarized mitochondria in both the epicardium as well as the endocardium (see Figure 3-6), what we refer to as a uniform recovery, show the least amount of tissue containing polarized mitochondria, significantly less than the two remaining profiles observed when compared using Student's t-test ($p < 0.05$). Figure 3-6 plots the values for the three profiles observed.

In order to gain a better understanding of the gradient of polarized mitochondria across the LV, a transmural region measuring approximately 1.5 mm square was selected in each heart as seen in Figure 3-8. The average pixel intensity in this region of the segmented Mitotracker signal was plotted versus the location in the LV wall in Figure 3-9. Before plotting, the calculated values at each location across the wall were median filtered. The resulting plot demonstrates the change in amount of polarized mitochondria from the epicardium to the endocardium in hearts with a depolarized endocardium. This was quantified as the change in pixel intensity per millimeter and plotted versus the observed profile in Figure 3-10. The Student's T-test was used to determine a significant difference ($p < 0.05$) between the hearts without a transmural bias and the two remaining profiles observed.

In order to obtain a more complete 3-D understanding of the nature of metabolic sinks, one heart was imaged throughout half its volume. A cross-sectional image slice was

acquired every 40 μm in an automated fashion using the AVIM. The collected image slices were loaded into ImageJ using the VolumeViewer plugin[43]. A virtual cut-plane was created along the septum to demonstrate that the distribution of the polarized mitochondria remained the same throughout the collected image volume with a depolarized region in and near the endocardium and a polarized region in and near the epicardium. The rendered image volume can be seen in Figure 3-11 along with several selected cross-sectional images acquired at different positions in the heart.

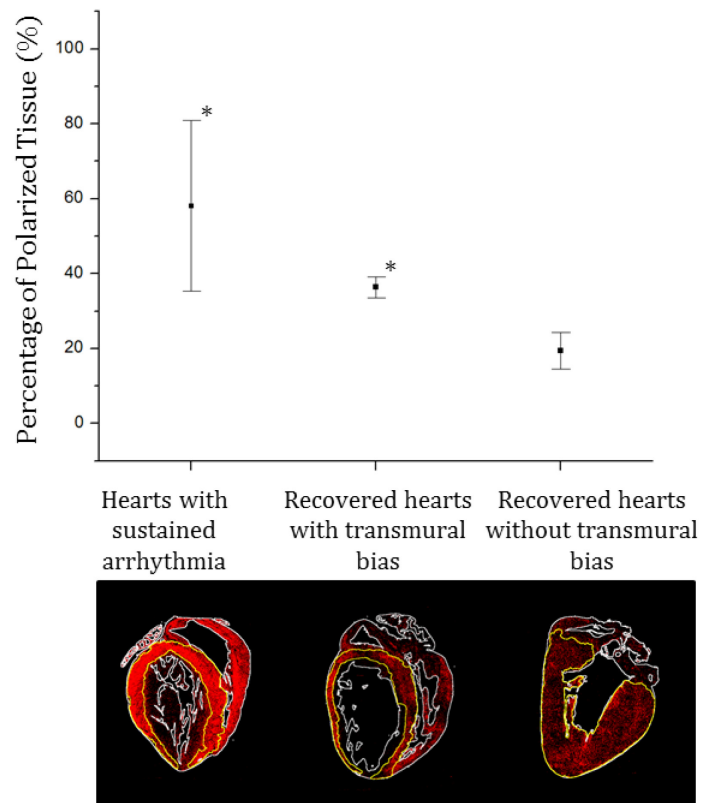


Figure 3-6: Recovery is More Sparse in Hearts without Transmural Bias

The tissue containing polarized mitochondria was selected in each heart and the percent of polarized tissue was calculated as the amount of tissue classified as polarized divided by total area considered; example selected regions are shown for each profile observed. Hearts with a sustained arrhythmia had a higher density of polarized mitochondria than the recovery hearts showing a uniform recovery. Also, there was a significant difference in the density of polarized mitochondria between recovery hearts that had a transmural bias and those that did not. (*) indicates significantly different ($p < 0.05$) from the recovered heart without transmural bias. Bars show standard deviation.

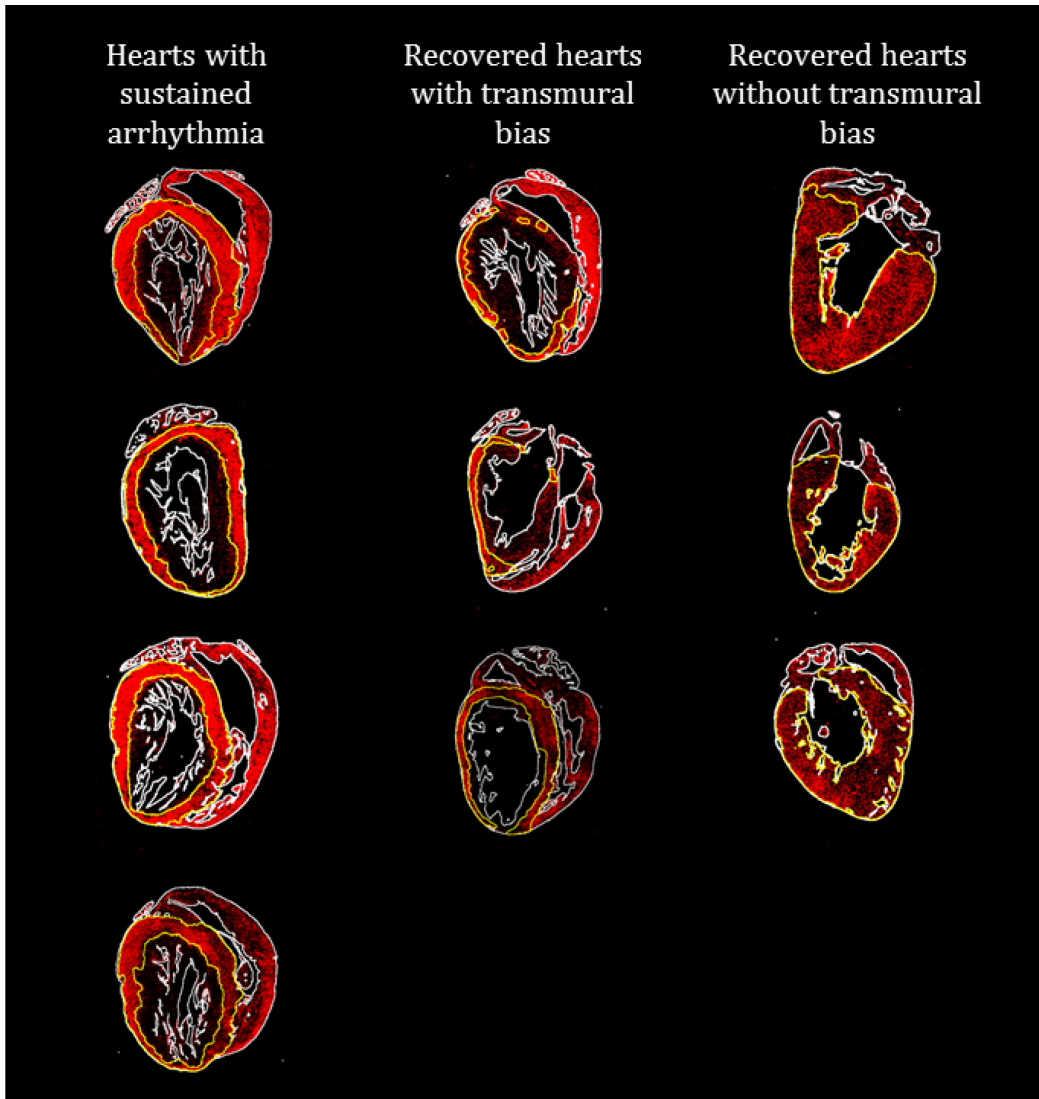


Figure 3-7: Selecting Regions with Polarized Mitochondria

The regions of tissue in the left ventricle displaying polarized mitochondria were selected in order to calculate the percentage of tissue within these regions containing polarized mitochondria in Figure 3-6.

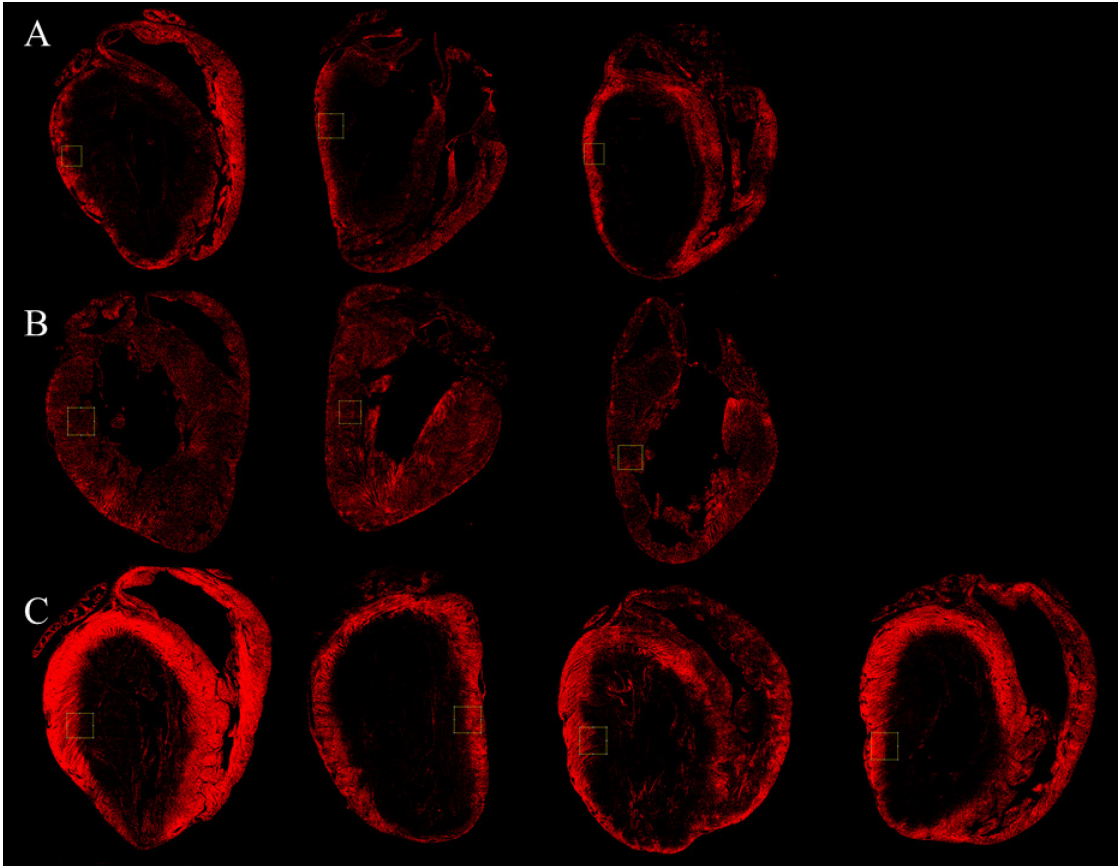


Figure 3-8: Selecting Transmural Gradient of Mitochondrial Polarization

A representative transmural region of the LV that captured the transition of mitochondrial polarization change from the epicardium to the endocardium was selected for each heart.

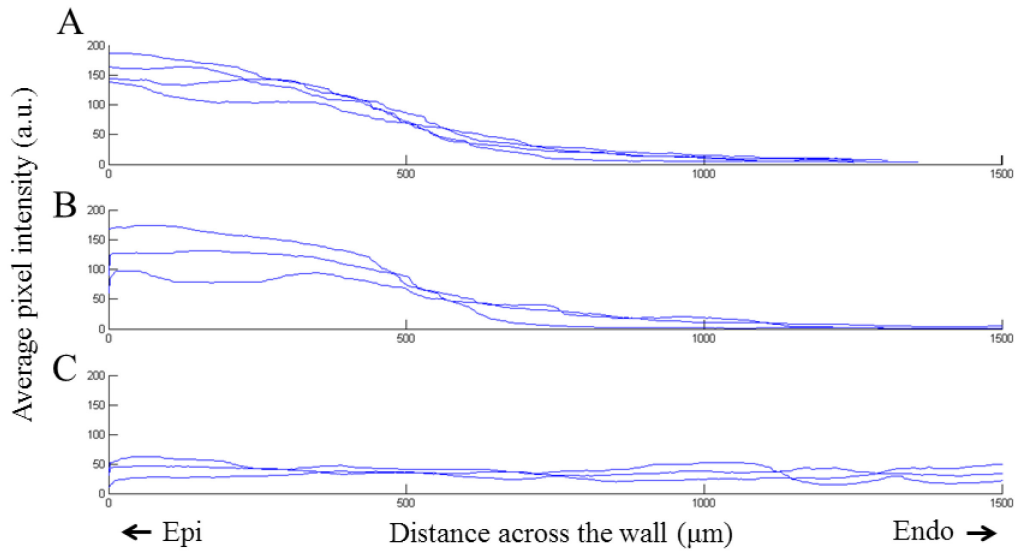


Figure 3-9: Gradient of Mitochondrial Polarization Transmurally

The average pixel intensity was used as a measure of amount of polarized mitochondria at each transmural position in the regions selected in Figure 3-8. This was plotted versus position transmurally for (A) the hearts with sustained reperfusion arrhythmias, (B) hearts regaining rhythmic beating with a depolarized endocardium, and (C) hearts with polarized mitochondria throughout the myocardium.

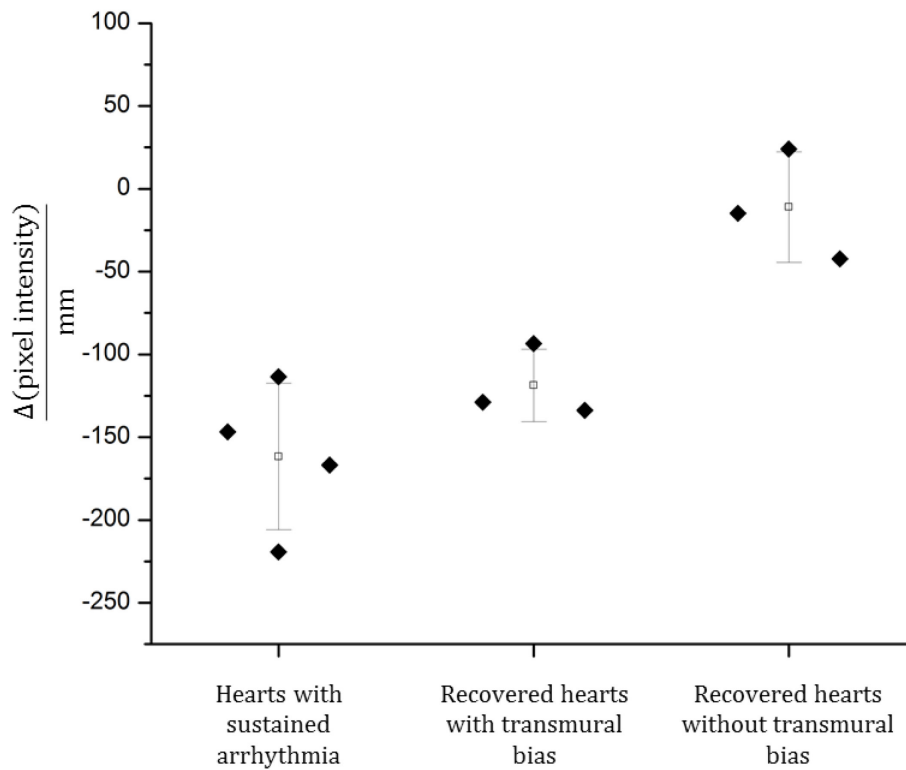


Figure 3-10: Comparing Gradient of Mitochondrial Polarization in Observed Profiles

For each of the plots in Figure 3-9, the change in average pixel intensity was calculated per millimeter. A Student's T-test was used to compare these values between the profiles of hearts observed in this study. A significant difference ($p < 0.05$) was measured between the recovered hearts without a transmural bias and the other two classes.

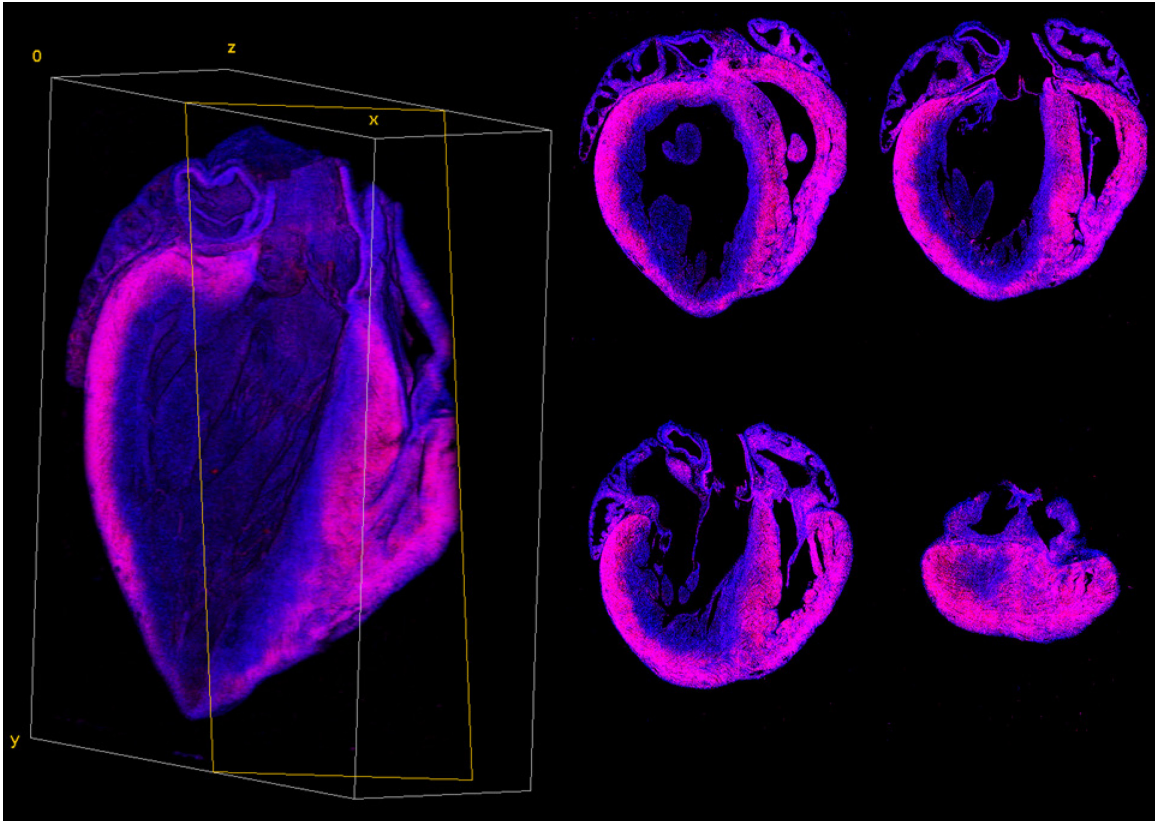


Figure 3-11: 3D Reconstruction of a Metabolic Sink

(Left) Image volume showing profile of polarized mitochondria throughout the septum.

(Right) Selected image slices from the acquired image volume showing depolarized mitochondria in or near the endocardium throughout the imaged volume.

3.3 Discussion

In this work, we have performed the first transmural imaging of metabolic sinks.

Slodzinski et al. originally found minimal loss of ψ_m following reperfusion in an intact GP heart exposed to IR injury by imaging the epicardial surface with a two-photon microscope[6]. These findings are supported by others showing that intact rodent hearts largely recovery ψ_m in the epicardium following up to 30 minutes of ischemia followed by reperfusion[7, 8, 52].

In the current work, we found that IR injury induced widespread depolarization of ψ_m in the endocardium of hearts displaying sustained reperfusion arrhythmias. It is well established that the endocardium of the left ventricle has a different metabolic profile than the epicardium [10, 18-21]. Weiss et al. first found a difference in the rate of oxygen consumption across the wall of the left ventricle, finding that the endocardium consumes roughly 30% more oxygen as compared to the epicardium [10]. This difference in oxygen consumption has been attributed to the greater amount of work being done by the endocardium, demonstrated most recently by Tsamis et al. showing that the endocardium undergoes higher levels of strain for longer periods of time than the epicardium [21]. In addition to the mechanical differences, Gao et al. found that endocardial cells had a higher intracellular sodium concentration $[Na^+]_i$ than epicardial cells [18]. The difference in $[Na^+]_i$ was supported by Gao et al.'s functional measurement of a higher current through the Na/K sarcolemmal pump as well as Osadchii et al.'s finding that endocardial cells have a higher expression of voltage-gated sodium channels as measured by western blotting[18, 20]. Because of the interdependence of pH, $[Na^+]_i$, and $[Ca^{2+}]_i$, through their respective exchangers, an increase in $[Na^+]_i$ may exacerbate the $[Na^+]_i$ increase known to

occur during reperfusion[59-61] thereby making endocardial cells more susceptible to Ca^{2+} overload during reperfusion.. Together, these findings suggest that epicardial cells may be more resilient to IR injury than endocardial cells in an intact heart.

The theory of a metabolic sink and its contribution to arrhythmogenesis was first introduced by Akar et al.[4]. Since then, many others have investigated the effects of metabolic stress on arrhythmogenesis [54, 55, 62-65]. In this study, we were able to show a significant depolarization of ψ_m in and near the endocardium of all (GP) hearts displaying a sustained arrhythmia following reperfusion. The depolarized endocardium juxtaposed to the polarized epicardium produces a sharp gradient in ψ_m transmurally. Zhou et al. created an experimental model of a metabolic current sink in a 2-D monolayer of neo-natal rat ventricular myocytes, using a coverslip to induce ischemia and subsequent depolarization of ψ_m in a region of cells surrounded by non-ischemic neighbors [15]. Using this preparation, they were able to demonstrate that these sharp gradients in ψ_m can be arrhythmogenic. Our findings show that hearts displaying a sustained reperfusion arrhythmia have a much larger region of depolarized myocardium in an intact heart than was used in Zhou et al.'s preparation or has been shown in epicardial mapping studies to date [7, 8, 15]. These results further support the theory of metabolic sinks as an important factor in reperfusion arrhythmogenesis.

While a depolarized ψ_m in and/or near the endocardium appears to be a necessary condition for reperfusion arrhythmia, the appearance of this recovery profile in hearts regaining rhythmic ECG demonstrates that this is not a sufficient condition for arrhythmogenesis. Normal conduction and beating in the heart relies on a wide array of factors and further studies will be needed to describe the difference between hearts with a

depolarized ψ_m in and/or near the endocardium that did recover rhythmic ECG and those hearts with a similar recovery profile that did not. An important finding in designing these studies is the difference in ECG between hearts with a recovered endocardium and those with a depolarized region in and/or near the endocardium. The difference in the ST segment and T wave between the two groups agrees with clinical diagnoses, mainly that the ECG of hearts with the depolarized ψ_m in and/or near the endocardium represents a more severe form of ischemia [57, 58]. It is possible that future studies can use the ECG interpretation to predict the recovery profile of ψ_m in the intact heart, facilitating a higher number of samples without the need to image each heart.

When we consider the relative amount of tissue with polarized ψ_m in the epicardium of hearts with a depolarized endocardium (those seen in Figure 3-2 and Figure 3-4), we are able to show that these regions in the epicardium have more tissue with polarized ψ_m per unit area than the hearts displaying uniform polarization of ψ_m (those seen in Figure 3-3). This was a surprising discovery and demonstrates the need for further research on this topic using the methods provided in this study.

A limitation of this study is the tradeoff between more spatial information and less temporal information. By loading the heart with MTR, fixing it in that state, and imaging as much of the heart as necessary, we have gained more spatial information than has been collected to date on the regional effects of IR injury on ψ_m depolarization. However, any mitochondria that is polarized during the 10 minute labeling period takes up MTR irreversibly, so there is the possibility that we have labeled some mitochondria incorrectly if they proceed to depolarize following labeling. The labeling phase is timed to prevent such mis-labeling, delivering MTR to the heart 5 minutes after the start of

reperfusion, a period in time sufficient to allow any depolarization of ψ_m to occur that will occur in reperfusion [8, 56]. We also have used a global ischemia model for the IR injury, a less clinically relevant model than one of regional ischemia. This model has been chosen because of the greater control it provided over the conditions in the heart, exposing all the tissue to the same conditions. Regional ischemia, mimicking the effects of a coronary occlusion, is known to create a non-uniform perfusion field, causing the endocardium to receive less flow than the epicardium[19]. Had we included this added complexity using a regional occlusion, it would be more difficult to separate the effect of uneven perfusion versus transmural heterogeneity.

Chapter 4 - Conclusions and Future Directions

Research into reperfusion arrhythmias dates back to the early 1970s[66]. In the following decades, a considerable amount has been learned about the molecular, cellular, and tissue-level mechanisms that lead to this clinical paradox. The experiments performed by Akar et al. and Slodzinski et al. to demonstrate the existence of metabolic sinks in intact hearts provided great support for this novel mechanism of arrhythmogenesis in the heart[4, 6]. In addition, the methods used in these studies have provided means to assess the efficacy of therapeutic pharmacological interventions designed to treat and prevent such arrhythmogenesis in the context of an intact heart [5, 52]. However, up until now our understanding of metabolic sinks *in situ* has been limited to only what can be observed and measured on the surface of the heart.

The methods provided in this work provide a glimpse of metabolic activity beyond the surface of the heart and demonstrate what we refer to as the “inside story” of myocardial metabolic sinks. The depolarization of ψ_m is far more widespread throughout the heart than has been demonstrated to date. The lack of polarized mitochondria in the endocardium of all hearts undergoing a sustained reperfusion arrhythmia underscores the importance of metabolic sinks in reperfusion arrhythmias. Of course, our findings create many questions as well.

Further work is needed to understand why only a portion of the hearts with a depolarized ψ_m in the endocardium presented with a sustained reperfusion arrhythmia. Also, it is not clear why hearts with uniform transmural recovery (polarized ψ_m in both epicardium and endocardium) have an overall lower density of cells exhibiting polarized ψ_m as compared

with the epicardium of hearts showing a transmural bias in the recovery of ψ_m following reperfusion. In addition to the questions raised in this study, there remains work to be done to elucidate the role metabolic sinks may play in heart failure. Studies have shown that mitochondrial function is impaired in heart failure [67, 68]. However, there has yet to be a study directed at the role of metabolic sinks under these pathophysiological conditions. A better understanding of these phenomena is vital for the treatment and prevention of reperfusion arrhythmias.

Going forward, we have provided unique methodologies to investigate these and other scientific questions. While the AVIM is well suited for the investigation of metabolic sinks in intact hearts, it also provides a platform for a wide range of experimentation. We have adapted the techniques of others [33-35] in order to make a more affordable and accommodating instrument. The ability to image fluorescent markers throughout a macroscopic volume at high spatial resolution can be applied to a variety of investigations. We provide detailed schematics and instructions for the AVIM in the Appendices and anticipate that this expansion of LSM capabilities will open the door to many new imaging studies and gain widespread use in the research community.

Further improvements to the AVIM software pipeline can both improve the quality of the output image volume as well as reduce the computational time and resources required to produce such a volume. The image tiles were acquired with 10% of their image dimension overlapped with adjacent in-plane tiles. In addition to reducing the effect of vignetting, this provides adequate overlap to apply an in-plane registration for image stitching. Currently, the over-defined problem of in-plane registration (aligning structure with several neighboring tiles) has produced unreliable results, leaving out image tiles or

incorrectly registering tiles to one another. Further work in this area may make in-plane registration for image stitching possible, improving the quality of the output image volume.

Because of the embarrassingly parallel nature of image volume reconstruction, the software pipeline relies on computational resources to facilitate reasonable reconstruction times. Improvements could be made to the software pipeline in order to reduce the dependence on computational resources mainly in the image registration step between intercut volumes and in the depth correction step on the output image slices. The Nelder-Mead optimization produces an accurate and relatively efficient alignment of the intercut volumes. However, the maximum error corrected in volumes thus far is under 20 μm or roughly 12 pixels in x or y. A constrained search algorithm within this search space may improve the efficiency of this registration step.

The depth correction algorithm uses the expectation-maximization algorithm to fit the foreground and background pixel intensity to a Gaussian distribution. The majority of the reconstruction time takes place during this fitting step. The algorithm is sensitive to the seeding parameters, and the algorithm can be restarted several times for an image slice in order to find adequate seeding parameters. An intelligent or adaptive seeding strategy may provide a more efficient approach to this problem. Also, implementing this algorithm on graphics processing units could significantly reduce the reconstruction time. These strategies would make the use of the AVIM more accessible by removing the need for large computational resources.

Appendix A AVIM Parts List

Off-the-shelf components

1. Inverterscope objective inverter – LSM Tech (Etters, PA). Contact the manufacturer for appropriate model. Arm length of 250 mm is recommended with Zeiss 7MP.



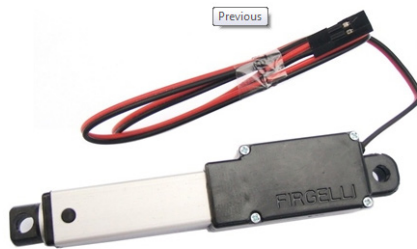
2. Sutter Instruments (Novato, CA) 3DMS with MP-285 Controller (RS-232 Interface). Note: Detach Y-axis stage component, reverse orientation, and re-mount Y-axis stage to X-axis stage. This provides a more compact design to reduce deflection of stage during cutting. The platform attached to the Z-stage will be removed; detach platform support arms, reverse orientation (horizontal edge pointing up), and re-mount to Z-axis stage – the custom machined platform will be attached here.



3. Edmund Optics (Barrington, NJ) 2" Travel, 3"L x 1.75"W Ball Bearing Slide Stock #37-361



4. Firgelli Technologies Inc. (Victoria, BC, Canada) L12-S-50mm-100:1-12V microactuator



5. 12V 500mA DC power supply
6. Post/Platform system from Newport Corp. (Irving, CA). Note: Parts are specified with English fittings. They are also available in Metric fittings, and they should be matched to the microscope's air table fittings if possible.
 - a. Model: 290-TP Top Plate, 6 x 10 in., 33 holes 1/4-20 Thread, 12 holes 1/4-20 CLR; Quantity: 2. Note: Platform to be above rotary stage will need to be machined in order to be centered and mounted on rotary stage. Platform below can be used as is.



- b. 1 inch Optical Posts/Pedestals PS Series – Order enough to raise platform to height of inverter



- c. Pedestal clamps PS-F; Quantity: 4



d. Model: 481-A Rotation Stage, 360° Coarse, 5° Fine



e. Model: 9201 Tiny Lab Jack, 1/8 in. Travel, 8-32 Thread. Quantity: 4



7. Windows PC with 2 USB ports (used for communication with NI I/O boards) and 1 RS-232 serial port (used for communication with Sutter stage) (a port on the motherboard is preferable to a USB dongle converter to and RS-232 port)
8. LabVIEW and Digital I/O components from National Instruments (Austin, TX)
 - a. LabVIEW 8
 - b. NI USB-6501 (24-ch, 8.5 mA) Low-Cost USB Digital I/O Device



c. NI USB-6525 8 Solid-State Relays, 8 DI, Counter, Ch-to-Ch Isolated



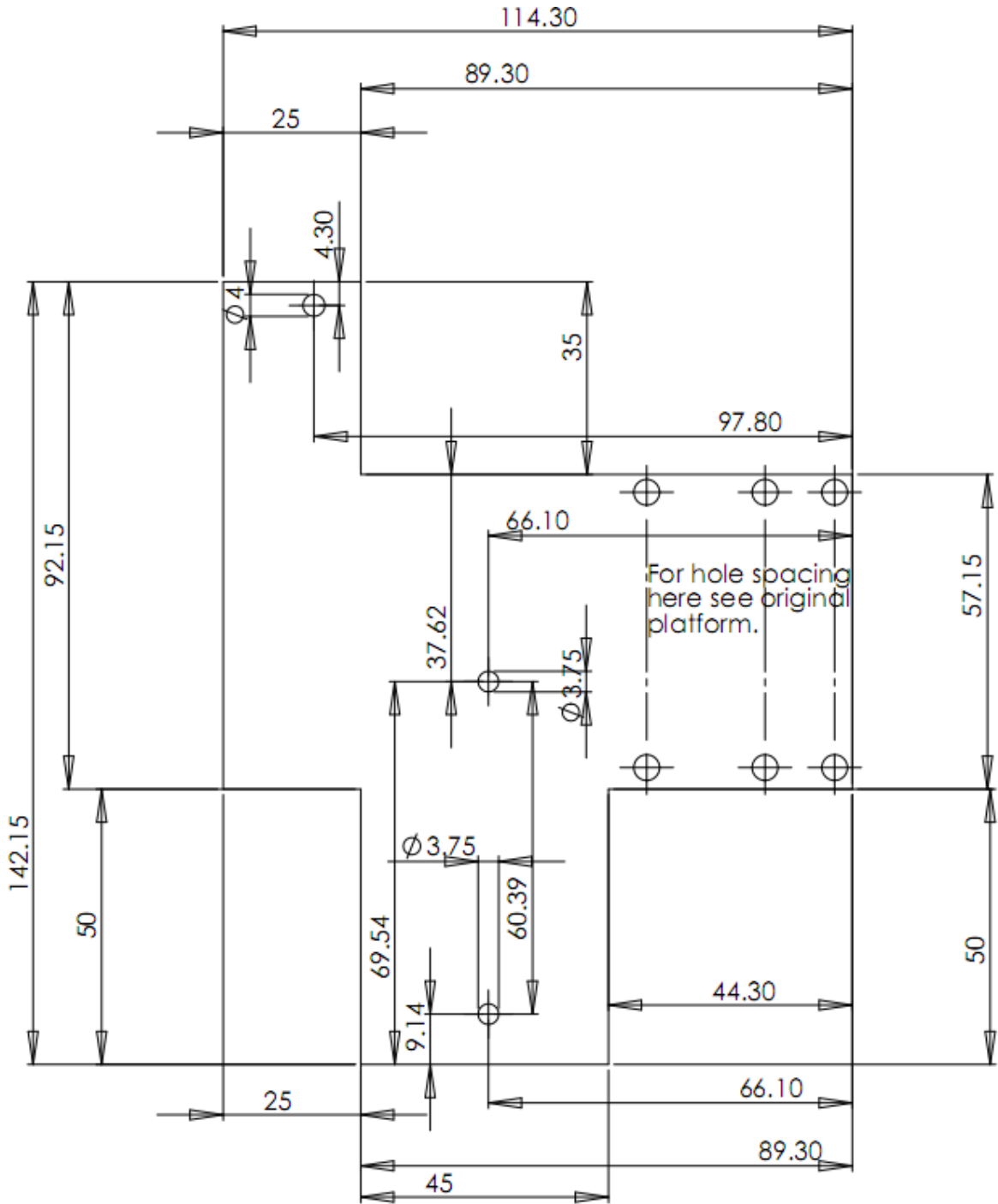
9. C.L. Sturkey Permanent Microtome Knife Flat Back 185mm (Catalog No.: 22-210-021 Fischer Sci)



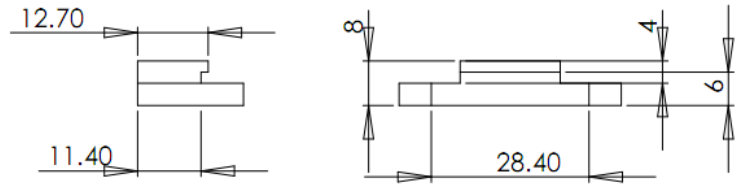
Custom-Machined Components

Unless otherwise specified, all units are in millimeters and the material is aluminum.

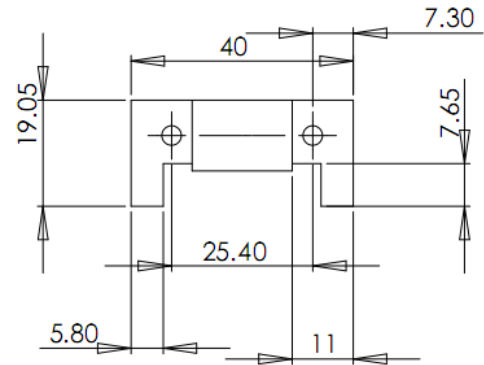
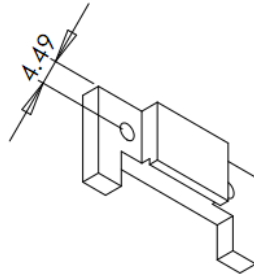
1. Replacement platform – attaches to support arms on Z-stage



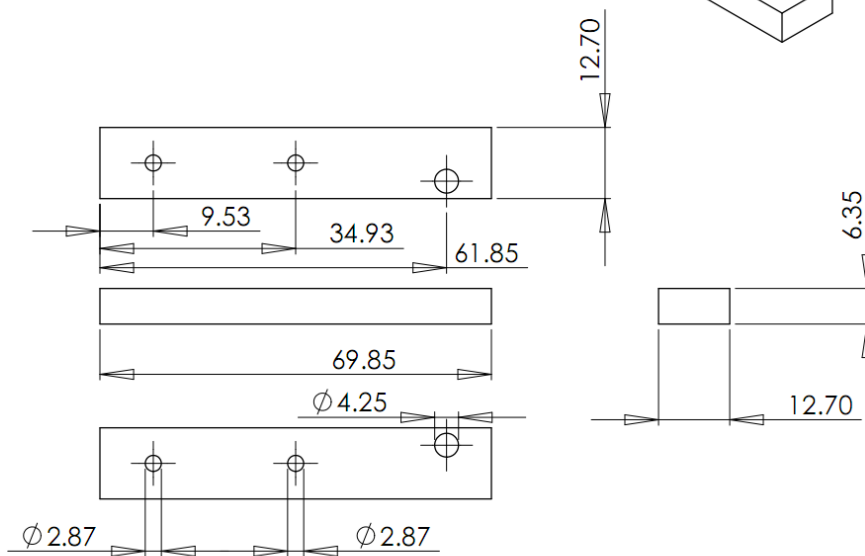
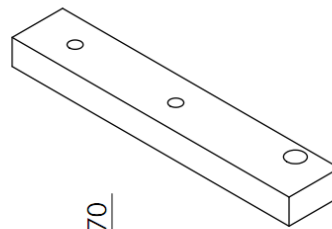
2. Embedding cassette holder – attaches to linear slide



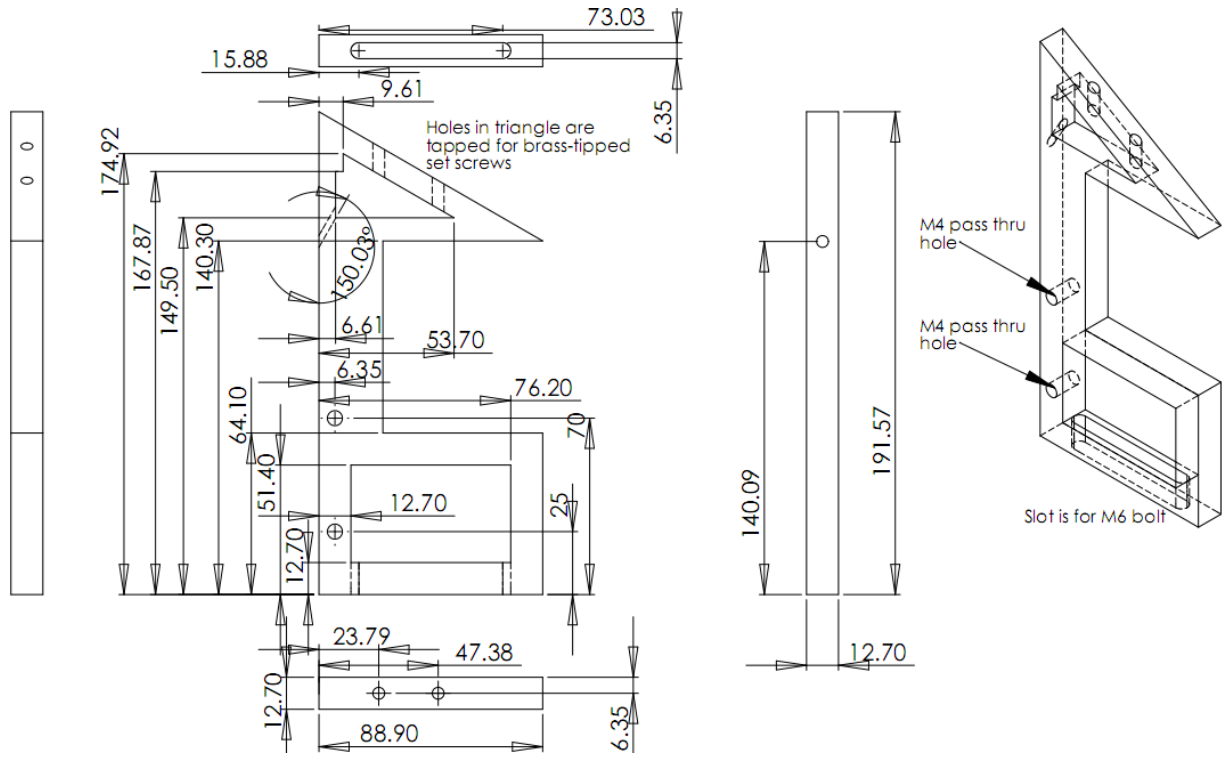
Holes are for a 6-32 screw to go through, NOT tapped.



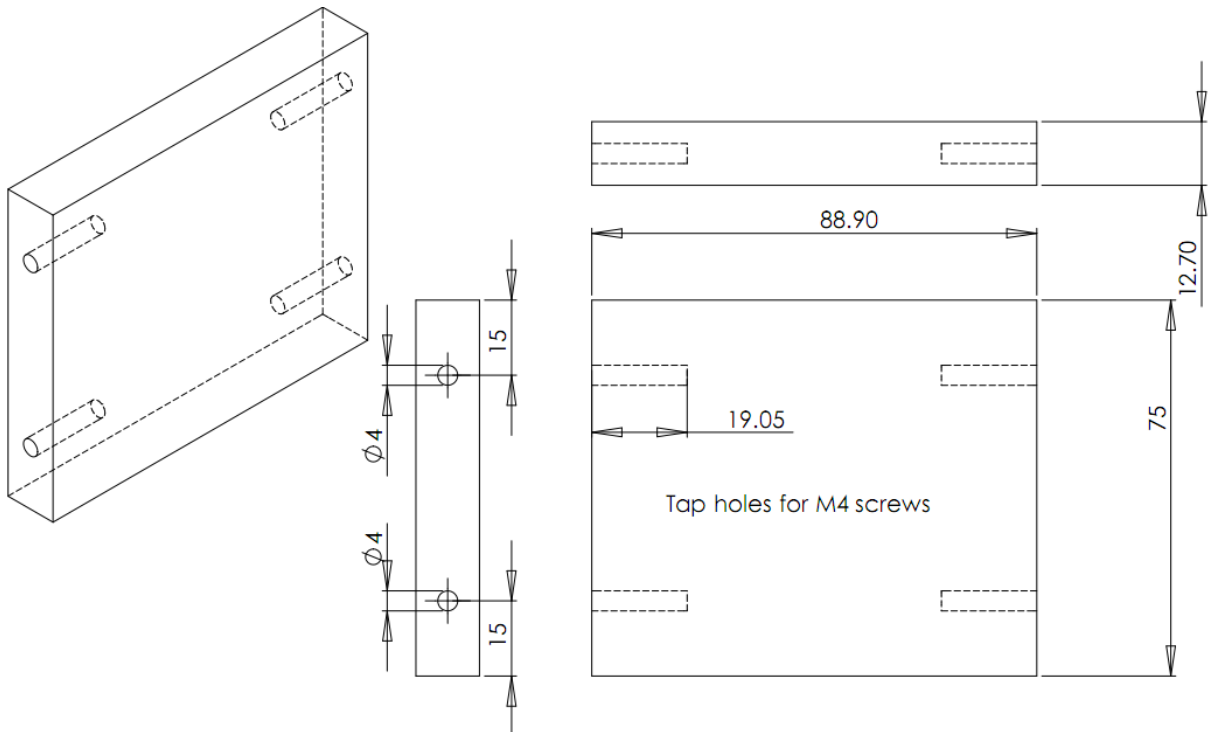
3. Actuator arm – attaches actuator to linear slide



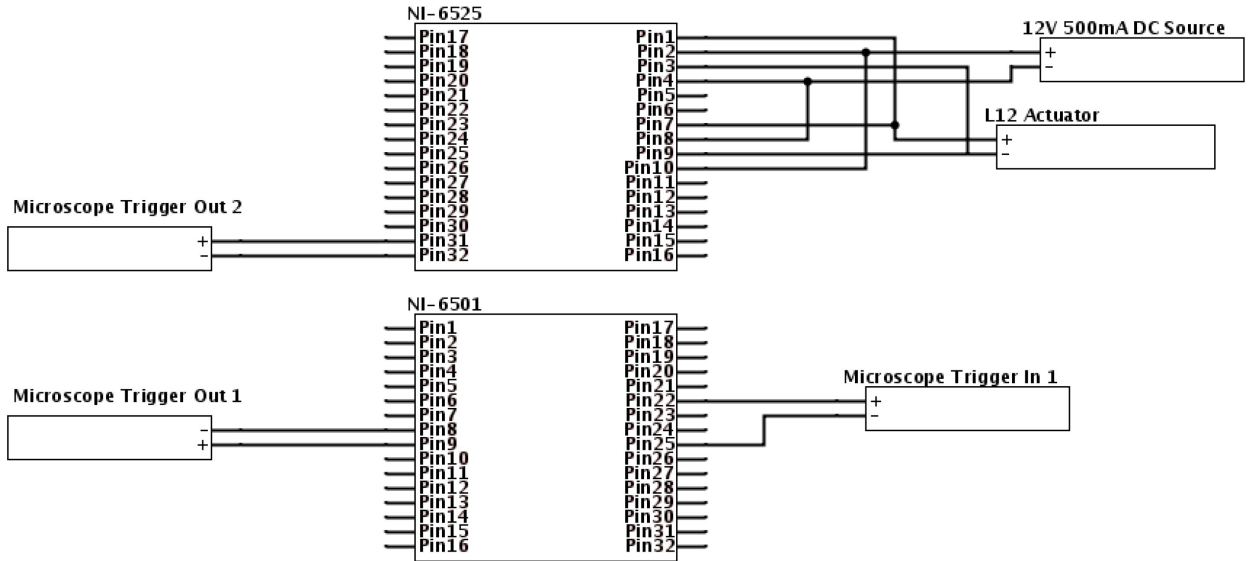
4. Microtome knife holder (Qty: 2) – attaches to Newport platform and holds Sturkey knife



5. Microtome cross beam – attaches to microtome knife holders



Wiring Diagram



Appendix B AVIM Operation Manual

These instructions are for use with a Zeiss 7MP microscope running Zen 2010 and Multi-Time 25.007. This version of Multi-Time has been modified by Zeiss to produce more reliable communication with the AVIM. Please consult Zeiss for questions regarding similarity in versioning with Multi-Time.

Image Volume Acquisition Protocol

Turning on the system

1. Locate the main power switch module near the microscope computer screen.
 - a. Turn on Main Switch.
 - b. Turn on Components.
 - c. Turn on Systems/PC.
2. Turn on Microscope Computer located beneath the air table towards the door.
3. Locate the laser power controller beneath the air table towards the window.

Switch the laser from Standby to On.

 - a. Switch the “Laser in Use” sign to On. The switch is next to the door.
4. Turn on the MP-285. Press the green Move button.
5. Turn on the AVIM Computer opposite the microscope.
 - a. The password for this computer is “password” without the quotes.

6. Plug in the 12V power supply and connect to the NI-USB 6525 control board.

Preparing the Sample to be Imaged

1. If an old sample is installed on the AVIM, remove it.
 - a. The sample can be removed with a phillips head screwdriver.
2. If an old knife cutting edge is still exposed, move the knife to a fresh cutting edge.
 - a. Never touch the knife where the sample would be cut.
 - b. The knife can be moved by loosening the four screws with the help of a flat screwdriver on top of the AVIM and carefully sliding the knife to make sure a new cutting edge will be exposed to the sample.
 - c. Tighten the four screws on top of the AVIM again and make sure the knife is securely fastened.
3. If there are no fresh cutting edges on the knife, change the knife.
 - a. Never touch the knife where the sample would be cut.
 - b. Loosen the top four screws on the AVIM which are used to fasten the knife in the holder.
 - c. Slowly slide the knife out from the holder space, and place it back in the wooden casing in which the knife came in, place the case in the box and send it for resharpening.

- d. Carefully remove the new knife from the wooden casing it came in, and slowly slide it in the knife holder area of the AVIM, not touching the cutting edge.
 - e. Tighten the four screws on top, making sure the knife is securely fastened.
 - f. See Microtome Blade Adjustment section below to fine tune the cutting before continuing.
4. Clean the sample-to-be-imaged of excess paraffin.
 - a. All sides of the cassette must be clear of paraffin including the bottom which needs to sit flush against the linear slide mount. Additional paraffin on the bottom of the cassette not interfering with a flush mount should not be removed. Removal of this material can interfere with the mounting integrity of the sample to the cassette.
 - b. The mounts used on the cassette need about 2 mm of the top of the cassette exposed along the short edges of the cassette. Clear away the paraffin in this area. Hold the mounts against the cassette to check for adequate clearance.
 - c. Remove all the excess paraffin on all the four sides of the embedded sample with a disposable blade. Be careful as to not chop off part of tissue in this process. Try to minimize, as much as possible, the cutting area that would be exposed to the knife cutting edge.
 5. Mount the sample on the AVIM using the phillips head screwdriver.

6. Using the MP-285 ROI, adjust the position of the stage so that the hash marks on the sides of each axis align with the “0” mark. Zero the MP-285 coordinates using the keys on the front of the controller.
 - a. Click on PGRM and follow the display to “SETUP”, “AXES”, “NEW ORIGIN”, “YES” to reset the axes.
 - b. Fill in point 5 in the acquisition worksheet to save the information.
7. Manually position the sample at X=0 Y=20,000.
8. Adjust the Z so that the top of the sample is just slightly lower than the microtome knife.
9. Open LabVIEW on the AVIM Computer.
10. Determine the height of the sample for cutting. Open and Run Manual_Cut_Control.vi
 - a. Click the “Extend” button in the LabVIEW window. When the actuator becomes fully extended, click the “Extend” button again to turn off the actuator.
 - i. THE ACTUATOR CAN ONLY RUN FOR SHORT PERIODS OF TIME. FAILURE TO TURN OFF THE ACTUATOR AT THE END OF EACH STROKE CAN DESTROY THE ACTUATOR!
 - b. Lower the sample 2 mm in the Z direction.

- c. Click the “Retract” button in the LabVIEW window. When the actuator becomes fully retracted, click the “Retract” button again to turn off the actuator.
 - i. NEVER HAVE BOTH THE “RETRACT” AND “EXTEND” BUTTONS ACTIVATED IN LABVIEW. THIS CONDITION CAN PERMANENTLY DAMAGE THE I/O CONTROLLER.
- d. Raise the sample to a height 50 microns higher than the initial attempted cut.
- e. Repeat [a] thru [d] until the knife comes in contact with the paraffin.
Record this value on the worksheet, point 7a
- f. Fully retract the sample returning the z position to the last cutting height.
Stop and Close Manual_Cut_Control.vi

11. Expose the sample on the surface of the paraffin block by first opening Automatic_Cutting_Control.vi

- a. Enter the Z value recorded in step 10e above as the starting value.
- b. Enter 40 (microns) as the step size between cuts.
- c. Enter a best guess at where the sample should appear on the surface of the paraffin as the stopping value.
- d. Run the VI. There are long pauses in the cutting to provide for the proper duty cycle required by the actuator. This step can take quite a long time.

- e. Monitor the sample during the cutting. When a portion of the sample becomes exposed on the surface of the paraffin, stop the VI making sure that it does not occur when the actuator is active - FAILURE TO DO SO CAN DESTROY THE ACTUATOR.
12. Note the Z location of the last cut; record this value on the worksheet, point 7b.
13. Move the stage to the Maximum Z value (i.e. all the way down). This will protect the sample during the positioning of the inverter.

Setting Up Microscope

1. If the condenser is installed on the microscope, remove it.
 - a. This is done by detaching its interface cable from the left side of the microscope and loosening its set screw on the right side of the microscope with a 3 mm hex key.
 - b. Place it on the counter in the box with padding being careful not to touch the lenses.
2. Check the cooler temperature. It should be $20.00^{\circ}\text{C} \pm 0.10^{\circ}\text{C}$.
 - a. The cooler is located next to the UPS, on the left of the Zen computer.
 - b. If coolant change is required, follow steps instructed in the Coherent laser guidebook. The book is usually located on the table opposite to the

microscope, or in the second from top rightmost drawer opposite the microscope.

3. Remove the 10X objective from the microscope (or the objective being used for this acquisition).
4. Locate the inverter stored in the top rightmost drawer opposite the microscope.
 - a. Attach the 10X (or other) objective to the inverter.
 - b. Straighten the inverter initially by placing two rotating flanges of the inverter flat on the counter and applying light pressure
 - c. Attach the inverter to the microscope, positioning the objective away from the microscope or AVIM to prevent possible damage to objective while mounting inverter.
5. Once Windows has loaded on the Microscope Computer select “LSM User”, no password.
6. Click on “Zen 2010” on the Desktop.
7. Once Zen has loaded, it gives you the option of Start System or Image Processing. If the condenser was installed before step 1, follow the sub-steps below. Otherwise, select “Start System”.
 - a. Click on the arrow next to “Boot Status”.
 - b. Click on the arrow next to “Hardware Configuration”.

- i. Select a configuration that does not include the condenser. This is denoted by the suffix “nocond” on the end of the configuration file.

If no such configuration file exists, contact Zeiss for assistance.
 - c. Click on “Start System”
 - d. If Zen doesn’t start up, reset the hardware controller CPU located behind the air table, near the wall.
8. Position the inverter over the sample using the bracket on the AVIM to center it correctly.
 - a. The bracket should slide easily over the inverter. If it doesn’t, adjust the position of the bracket on the rail so that the bracket applies equal (light) pressure to both sides of the inverter.
9. Return the stage to the position of the last cut noted above.
10. Using X and Y controls on the stage, position the exposed portion of the sample directly under the objective.
11. Click on the Ocular tab on the top left of the screen.
12. Click Online to bring the epifluorescent controls online.
13. Turn on the reflected light source by clicking the Off button on the icon denoting the reflected light source on the screen.
14. Adjust the light intensity; usually 12% (lowest nonzero setting) is ample.

Setting up the AVIM

1. Open AVIM_Zeiss_v11_MultipleCuts_NoFinalCut_xdec_yinc_NoZZ.vi in LabVIEW.
2. Specify a parameters and coordinates filename in the fields provided.
 - a. These must include the full path.
 - b. Click on the folder next to each field to select a file for this if desired.
 - c. It is recommended that these files include the date of acquisition (i.e. p14920101.txt and c14920101.txt for the parameters and coordinates file, respectively, collected on Jan 1, 1492.
3. Using the Ocular mode on the microscope, focus the microscope on the sample.
 - a. Adjust focus with the focal adjustment knobs on the microscope or touch panel.
 - i. Moving the knob clockwise move the objective up.
 - ii. Moving the knob counter-clockwise moves the objective down.
 - b. Adjust the sample's X and Y position using the MP-285 ROI if necessary.
 - c. Use the Microscope touch panel to switch reflectors, i.e. Red, Green, Blue. (This is done within the Control menu on the touch panel menu) if necessary.

4. Determine the X and Y start and stop coordinates by adjusting the position of the sample with the manual control knobs of the MP-285 while observing the sample through the eyepiece and noting the position of the incident light on the sample with the naked eye. Error on the side of imaging too much area.
 - a. While observing the position of the incident light, you may notice additional reflectance of sample buried within the paraffin appearing differently than the areas with no sample. Use this as an aid in determining the X and Y range above.
 - b. Record start and stop values for X and Y in their respective fields within LabVIEW program, as well as the worksheets in points 10 and 11.
 - i. Start values MUST be LARGER than Stop values for X and Y.
5. Roughly estimate the Stop value for Z so that the acquisition is running for less than 24 hours.
 - a. This can be done by calculating the time it takes to image one plane, and estimating the number of planes that could be imaged in the given time period.
 - b. Record your estimated stop value for z on the worksheet.
 - c. Z Stop value MUST be LESS THAN Z Start value.
6. Enter the Z Start and Stop values determined earlier in the LabVIEW program and in the worksheet at points 12a, 23b (start) and 23c (stop).

7. The value for the Z Cut Step has a default value of one 40 μm cut (for a single cut protocol, see Next Step for multiple cut setups). Large variations from this value are not recommended.
8. If you want to acquire images after each 40 μm cut step, leave Number of Cuts = 1 and Cut Step Size = 40 μm (Default Values). Otherwise, Number of Cuts and Cut Step Size are used for acquiring consecutive planes of images throughout a sample volume more than 40 μm (one cut) apart (i.e. acquire an image slice every 200 μm throughout the sample). “Number of Cuts” x “Cut Step Size” = “Z Cut Step”. Cut Step Size should be set to 40 μm to achieve optimal cutting. Number of Cuts should be set so that the equation described earlier is satisfied. For example: Acquiring an image slice every 200 μm throughout sample should have Z Cut Step = 200, Cut Step Size = 40, and Number of Cuts = 5.

Setting up an Acquisition

1. Position the sample so that the objective is over a center portion of the sample (and so that there will be some signal visible).
2. Ensure the Z position is set to the Z Start value.
3. Check that the sample is still in focus in the Ocular mode.
4. Switch the Ocular mode to Offline.
5. Click on the Acquisition tab.

6. Select a configuration file if desired. Otherwise, you can start from the default configuration.
7. If “Z Stack” isn’t checked, check it now.
8. Within the Setup Manager area on the left hand side of the screen, select Light Path.
 - a. Select the channels you wish to record in.
 - b. Turn the laser “On” and adjust its intensity to 1.0%.
 - c. Select the wavelength you require for the acquisition based on the dye used to prepare the sample.
 - d. Be sure to check that the Laser status is shown to be “Mode-Locked”. If it shows “CW-lasing” for a long time, then change the wavelength to 700nm, and then get it back up to the desired wavelength. This should help achieve a mode-lock.
9. Within the Online Acquisition area on the left hand side of the screen, select the relevant Channels.
 - a. Make sure the Master Gains are all below 1000 throughout the protocol.
 - b. A good starting value is 800 for each channel.
10. Turn off lights in the room.

11. Click “Live” on the upper left area of the screen. This gives you a continuous scanning of the sample, or a “live” view of the current imaging setup.
 - a. Clicking the button again (now represented by a Stop sign) will stop the acquisition.
 - b. Start and stop the laser scanning as needed.
 - c. Important: keep scanning time to a minimum to prevent/reduce sample photo-bleaching.
12. Increase laser intensity SLOWLY until a signal is noticeable.
 - a. While searching for signal, slightly adjust focal plane occasionally to ensure focal plane is appropriately adjusted.
13. Once signal is visible adjust focal plane so that signal is highest. This is the surface of the sample. Adjust laser intensity, gain, and background to produce best possible image.
14. Check if the corners of the image display a standard vignetting pattern i.e., the corners look the same in intensity.
 - a. If the corners do not display standard vignetting pattern, e.g. one corner is brighter than the other three, then adjust the leg height on which the AVIM is mounted on.

- b. Carefully select which leg height to adjust, based on the image. Note that there is a 90deg clockwise rotation of the image that is displayed on screen in the ZEN program from the actual orientation of the sample.
 - c. Use trial and error with the leg height and try and achieve a standard vignetting pattern on screen on all the 4 corners of the image.
15. Under the Multidimensional Analysis banner click on Z Stack.
- a. Click on the arrow next to Use Correction
 - b. Set the Refractive Index to 1.47 (this will compensate for the refractive index mismatch and scale the z coordinates accordingly)
16. Adjust the focus of the microscope (clockwise) until the focal plane is at the top of the range where the structure is still producing a good image. This should be close to where you made your adjustments in step 13.
- a. Click “Set Last” to set the current position as the last position in the optical stack.
17. Adjust the focus of the microscope (counter-clockwise) until the focal plane is at the bottom of the range where the structure is still visible.
- a. Click “Set First” to set the current position as the first position in the optical stack.
 - b. Repeat steps 15 and 16 until you have the desired z range for your optical stacks.

- c. The optical stacks are collected from the bottom of the Z-stack (First) to the top of the Z-stack (Last). The focus motor will always move in steps against gravity during an optical stack acquisition.
18. Because of slight cutting errors, it is best to add an additional range above and below your desired Z-stack. Best results have been found with an additional 50 microns on each end of the stack for a 24 hour acquisition.
19. Set the increment between images in the Z Stack (usually this is between 5 and 10 μm)
20. Adjust the speed of the scanning so that you obtain a clear enough image. Usually speeds 8 or 9 are sufficient to collect a quality image.
 - a. Using the acquisition time for a single image set above with the speed setting, determine how long an entire stack will take to acquire.
 - b. Add 2 seconds to this time and enter this value as Stack Acquisition Time into the AVIM Computer.
21. Place the mouse over the Run button on the LabVIEW program, and turn off the AVIM monitor. Do NOT click the mouse button at this point!
22. Select the brightest image in the optical stack and then adjust the GDD of the laser.
 - a. See Laser GDD Correction section below for instructions on GDD Adjustment.

23. Click on the “C” in the visual representation of the Z Stack. This will move the focal plane to the center of the defined stack and record a single image there.
 - a. IMPORTANT: FAILURE TO SAVE THE CONFIGURATION WITH THE Z-STACK CENTERED CAN CAUSE ERRORS IN Z-RANGE!
24. Save the configuration using the following format: name_year_month_day.
25. Open Multi-Time v25.007 by clicking on Macro at the top of the screen and then click on Multi-Time v25.007.
26. Set the directory where the acquired images will be saved. It is recommended that you save it on the D:\ (Data) drive in a folder named with your name or initials and finally setup a subfolder named as the current date (year_month_day).
 - a. Additional folders can be made for that day by adding a letter at the end of the directory name.
27. Click on the Acquisition tab in Multi-Time and load the configuration you saved above by selecting it from the drop-down menus and clicking Load (Make sure you click Load!)
28. Ensure “Trigger in to Start” is checked.
29. Ensure Trigger In is set to “Trigger1”
30. Ensure Trigger Out at Block Start is set to “Trigger 2”
31. Ensure Trigger Out at Block End is set to “Trigger 1” (note: input and output triggers have exclusive Trigger 1, 2, etc.)

32. Click on the Timing tab

- a. Ensure you collect enough stacks for the acquisition.
- b. Group should be set to 1000, and Experiment should be set so that more stacks than necessary will be acquired. (Multi-Time won't continue looking for triggers beyond the number of stacks defined here).
- c. Experiments * Group = Total stacks
- d. Usually Experiments is set to 100, resulting in 100,000 expected stack acquisitions, much larger than the average collection.

33. Click on Options Tab

- a. Ensure "Triggers Out Stop Special" is checked.
- b. Click on "Hardware Timing"
 - i. Set WI Switching = 0 ms
 - ii. Set NLO Shutter = 1000 ms

34. Click on Start in Multi-Time.

35. Start the air outlet present on the platform opposite the microscope which has plastic tubing that takes the air to the microtome in the AVIM.

- a. Adjust the opening of the tubing near the microtome to make sure sufficient air is blowing across the blade edge in contact with the sample.
- b. This is to prevent any excessive paraffin buildup near the cutting edge.

36. Click the mouse button on the AVIM Computer without moving the mouse. This should start the Acquisition. (Leaving the screen on can create large amounts of noise in the acquired images.)

The acquisition should be running now. Make sure the “Laser In Use” sign is illuminated, and exit the room between stack acquisitions to minimize noise from the hallway lights.

Finishing the Acquisition

1. Once the acquisition is complete, turn on the Microscope Computer monitor.
Click ‘Finish’ in Multi-Time.
 - a. IMPORTANT: IF YOU CLICK “STOP” IN MULTI-TIME BY MISTAKE, MAKE SURE YOU DO NOT DISCARD ACQUIRED STACKS! THIS WILL DELETE ALL IMAGES GATHERED DURING THIS ACQUISITION!!
 - b. Clicking ‘Finish’ will end the acquisition on the Microscope.
 - c. The acquisition on the AVIM is automatically ended when all images are acquired.
2. Close Multi-Time.
3. Connect a USB drive to the AVIM computer using the USB extension cable (This cable should remain attached to the AVIM computer at all times. It is used to prevent wear and tear on the AVIM computer’s USB connections)
 - a. Copy the parameters and coordinates file for the current image volume acquisition to the USB drive.

- b. Eject and disconnect the USB drive.
4. Connect the USB drive to the Microscope computer.
 - a. Copy the parameters and coordinates file to the directory created during the Acquisition Setup in the Multi-Time interface.
 - b. Eject and disconnect the USB drive.
5. Connect the Microscope computer to the network by plugging the blue network cable into the blue LAN port above the chiller (behind the microscope).
6. Copy all files gathered for the acquisition to the ICM cluster.
 - a. Open FileZilla on Microscope computer.
 - b. Open a connection to the ICM Cluster.
 - c. Copy the directory on the Microscope computer containing the images, parameters, and coordinates files to the ICM Cluster.
 - d. When copying is complete, close FileZilla.
7. If you wish to restart the acquisition, skip steps below go to the restarting the acquisition section.
8. Close Zen.
9. Quit LabVIEW on AVIM computer.
10. Shutdown AVIM computer.

11. Shutdown Microscope Computer.
12. Turn Laser to Standby.
13. Turn off MP-285 Controller.
14. Unplug the 12V power source from NI-6525 USB board.
15. Turn off Microscope as follows
 - a. Turn off Systems/PC
 - b. Turn off Components
 - c. Turn off Main Switch
16. Turn off “Laser in Use” sign.
17. Lock the door on the way out.

Restarting the Acquisition

1. Once you have completed the acquisition and transferred the files to the cluster, refer to the Image Volume Reconstruction protocol and do a quick reconstruction to check if the image quality is satisfactory.
 - a. If not, make a note of the parameters to change for the next acquisition.
2. Cut imaged portion of sample.
 - a. Open Automatic_cut_control.vi in the AVIM computer.

- b. Enter the Z_{start} value the same as the Z_{stop} value of the previous acquisition. Specify Z_{cut_step} and enter Z_{stop} as $Z_{stop}=Z_{start}-Z_{cut_step}$.
 - a. Run the VI. There are long pauses in the cutting to provide for the proper duty cycle required by the actuator. This step can take quite a long time.
 - b. Monitor the sample during the cutting. Stop the VI when you have taken off the desired cut depth, making sure that it does not occur when the actuator is active - FAILURE TO DO SO CAN DESTROY THE ACTUATOR.
- 3. The Z_{stop} value after the cut will be your Z_{start} value for the next acquisition. Update this in the AVIM_Zeiss_v11_MultipleCuts_NoFinalCut_xdec_yinc_NoZZ.vi.
 - a. Record this value in the Worksheet under the respective dataset.
- 4. Roughly estimate the Stop value for Z so that the acquisition is running for less than 24 hours.
 - a. This can be done by calculating the time it takes to image one plane, and estimating the number of planes that could be imaged in the given time period.
 - b. Record your estimated stop value for z on the worksheet.
 - c. Stop value MUST be LESS THAN Start value.

5. If required, make the necessary changes in the parameters.
6. Update the parameter and coordinate file name.
7. Place the mouse over the Run button on the LabVIEW program, and turn off the AVIM monitor. Do NOT click the mouse button at this point!
8. Reset the Zeiss system
 - a. First follow steps 8-15 in “Finishing the Acquisition”
 - b. Then steps 1-2 in “Turning on the System”
 - c. Then steps 5-7 in “Setting up the Microscope”
 - d. Load the configuration file from the previous acquisition
9. Setup Z-stack for acquisition.
 - a. First set the refractive index for paraffin as described in step 15 of “Setting up an Acquisition”
 - b. The Z-stack will be the same as the prior acquisition, but manually check the range, and adjust it using steps 16-18 of “Setting up an Acquisition”. Be sure to incorporate any changes in the parameters if required. Unless necessary, do not change the optical stack depth, preferably keeping it constant across all datasets for the same heart.
10. Start the acquisition as from step 20 in “Setting up an Acquisition”

Image Volume Acquisition Worksheet

(Please answer ALL questions below for EVERY Acquisition)

1. Date of Acquisition: _____

2. Sample Code (cassette label): _____

3. SampleDescription: _____

4. Sample orientation after embedding (rough diagram)

-
5. Reset MP-285 controller coordinates? _____
 - a. Previous X at 0? _____
 - b. Previous Y at 0? _____
 - c. Previous Z at 0? _____

6. Knife Description (Knife number on the back):

7. Cutting first engaged paraffin at :

- a. Z (start) = _____

b. $Z(\text{stop}) =$ _____

8. Z cut step used to prepare sample: _____

9. Number of cuts before reaching the sample = _____

10. X coordinates:

a. $X_{\text{start}} =$ _____

b. $X_{\text{stop}} =$ _____

11. Y Coordinates:

a. $Y_{\text{start}} =$ _____

b. $Y_{\text{stop}} =$ _____

12. Z coordinates:

a. $Z_{\text{Start}} =$ _____

13. Laser wavelength used: _____

14. Laser output power (Wattage and % of power): _____

15. Depth correction factor used in z-stacks: _____

a. (IMPORTANT: this is NOT saved by the configuration file)

16. Adjust GDD value?(what value if “yes”) _____

17. Objective Used: _____

18. "QuickZ" acquired? _____

a. At Z= _____

b. Directory: _____

19. Check Rotary Stage alignment? _____

a. Misalignment measured: _____

20. Uniform intensity across imaged area? _____

21. Image looks good in normal room lighting? (i.e. lights on in room)

22. Laser correction used? _____

a. Max laser power: _____

b. Max NDD gain: _____

c. Min laser power: _____

d. Min NDD gain: _____

23. Dataset 1:

a. Directory: _____

b. Start Z: _____

c. Stop Z: _____

- d. Name of configuration file in Zen: _____
- e. Estimated time to run protocol (this should be < 24 hours):

- f. Number of cuts and tissue area (microns): _____
- g. Reconstructed? (enter cluster information): _____

24. Dataset 2:

- a. Directory: _____
- b. Start Z: _____
- c. Stop Z: _____
- d. Name of configuration file in Zen: _____
- e. Estimated time to run protocol (this should be < 24 hours):

- f. Number of cuts and tissue area (microns): _____
- g. Reconstructed? (enter cluster information): _____

25. Dataset 3:

- a. Directory: _____
- b. Start Z: _____
- c. Stop Z: _____

- d. Name of configuration file in Zen: _____
- e. Estimated time to run protocol (this should be < 24 hours):

- f. Number of cuts and tissue area (microns): _____
- g. Reconstructed? (enter cluster information): _____

26. Dataset 4:

- a. Directory: _____
- b. Start Z: _____
- c. Stop Z: _____
- d. Name of configuration file in Zen: _____
- e. Estimated time to run protocol (this should be < 24 hours):

- f. Number of cuts and tissue area (microns): _____
- g. Reconstructed? (enter cluster information): _____

27. Dataset 5:

- a. Directory: _____
- b. Start Z: _____
- c. Stop Z: _____

- d. Name of configuration file in Zen: _____
- e. Estimated time to run protocol (this should be < 24 hours):

- f. Number of cuts and tissue area (microns): _____
- g. Reconstructed? (enter cluster information): _____

28. Dataset 6:

- a. Directory: _____
- b. Start Z: _____
- c. Stop Z: _____
- d. Name of configuration file in Zen: _____
- e. Estimated time to run protocol (this should be < 24 hours):

- f. Number of cuts and tissue area (microns): _____
- g. Reconstructed? (enter cluster information): _____

29. Dataset 7:

- a. Directory: _____
- b. Start Z: _____
- c. Stop Z: _____

- d. Name of configuration file in Zen: _____
- e. Estimated time to run protocol (this should be < 24 hours):

- f. Number of cuts and tissue area (microns): _____
- g. Reconstructed? (enter cluster information): _____

30. Dataset 8:

- a. Directory: _____
- b. Start Z: _____
- c. Stop Z: _____
- d. Name of configuration file in Zen: _____
- e. Estimated time to run protocol (this should be < 24 hours):

- f. Number of cuts and tissue area (microns): _____
- g. Reconstructed? (enter cluster information): _____

Image Volume Reconstruction Protocol

Required Software Dependencies

For the reconstruction pipeline to function, the following Python libraries need to be specified in the system path or the reconstruct scripts should be modified to indicate the library locations. The software pipeline has been designed and tested on Python 2.6.

- PyLSM-0.1-r33 (used for reading in Zeiss LSM file format)
- pp-1.6.2 (Parallel Python libraries)
- SciPy 0.7.1
- NumPy 1.3.0
- Python Imaging Library 1.1.7

Gathering the Data

These steps are done on the ICM cluster.

1. Collect the folder of images acquired from the Zeiss microscope computer.
 - a. Take the folder labeled as the date of acquisition and not the folder within this one.
 - i. This will be referred to as the “working directory” from now on
 - b. This can be done over the network, transferring the directory to your cluster account.
2. Collect the parameters and coordinates files from the AVIM computer.
 - a. You will need a USB drive for this. Do NOT connect the AVIM computer to the internet!!
 - b. Copy these to the working directory.
3. Rename the “temp” folder to “stack_folder”
4. Copy reconstruct_parallel_multiovp.py and Reconstruct.sh into the working directory.

Reconstruction

1. Open Reconstruct.sh with a text editor
2. Be sure to change the following variables in the file based on the requirement of the dataset reconstruction.

- a. The number of nodes and processors per node required. NOTE: The product of these two numbers will be the value of the variable 'ncpus' in the reconstruct_parallel_multiovp.py file.

```
#PBS -l nodes=8:ppn=4.
```

- b. The estimated wall time required for the entire reconstruction. Be sure to put a higher value to be on the safer side.

```
#PBS -l walltime=10:00:00
```

- c. Email address.

```
#PBS -M email@jhu.edu
```

- d. The queue in which the job will run. If using the main queue (recommended for higher number of nodes) the value will be 'dque', if using the Winslow queue the value will be 'rlwq', if using the test node the value will be 'testq'

```
#PBS -q dque
```

- e. Enter the full directory path under "WORK_DIR"

- f. Be sure to include the executable file name and the parameters file name under the variable "EXECUTABLE".
e.g. `"/reconstruct_parallel_multiiovp.py pmdi4131205.txt"` (with the quotes)
3. Open `reconstruct_parallel_multiiovp.py` with a text editor (vi works well).
 4. Set the user defined flags to perform the desired operations. Typical settings for a reconstruction are shown below. See the comments in the `reconstruct_parallel_multiiovp.py` script to learn more about the available flag settings.

```
ncpus = 32 (product of nodes and ppn from the Reconstruct.sh file)
```

```
use_channel = 0
```

```
Extract_images_direct_LSM = 0 ## only works on test1... naming system
```

```
Rename_extract_images = 0 ## PERMANENTLY changes to Stack... naming system
```

```
check_dataset = 0
```

```
Correct_InPlane = 0
```

```
Correct_OutOfPlane_Slices = 1
```

```
Slice_directory = 'combined_slices' (which directory the out-of-plane correction will be performed)
```

```
Align_images = 0 (deprecated, leave as '0')
```

```
Align_slices = 0
```

```
Stitch_images = 1
```

```
overlap_combine_method = 1
```

Collapse_zstack = 0

Save_template = 1

cluster = 1

5. Make sure you are on the user1 node and in the working directory and then run the reconstruction program with the command “qsub Reconstruct.sh”
6. You can check the statuses of the job by using the commands ‘qstat -q’ ; ‘qstat -au <username>’ ; ‘qstat’
7. The progress of the operations is updated in the file logfile_reconstruction.txt for the user.
8. When the script finishes running an email will be sent to the email address provided, and the image volume is output to a “output_slices” or ”combined_slices” folder based on the operations performed during reconstruction.
9. Any errors during the reconstruction will appear in the working directory.
 - a. Non ideal alignments (alignment score of less than 85%) will be recorded in Nonideal_offsets.txt
 - i. See the section below on Checking Alignment on how to interpret this information.
 - b. If the depth correction algorithm failed on any individual image, this would be recorded in uncorrected_stacks.txt (if depth correction is working on optical stacks)

- c. If the depth correction algorithm failed on any individual slice, this would be recorded in `uncorrected_slices.txt` (if depth correction is working on stitched slices)

Checking Slice Registration

Additional information is provided for any registration between image slices that is below 85%. As of this manual's writing, it has never been necessary to manually register image slices acquired before and after a cut. If it becomes necessary (noticeable misalignment in a rendered image volume), these instructions provide the means to manually align the image slices for accurate 3D rendering, virtual cut planes, etc.

1. If the optimal alignment between inter-cut sections scored below 85%, the alignment output along with relevant information is output to `Nonideal_offsets.txt`
2. For each non-ideal alignment, the following information is collected
 - a. The reference intercut section and the intercut section to be aligned.
 - b. The individual images used for the alignment.
 - c. The resulting alignment and the score associated with this alignment.
 - d. A reference to a directory containing
 - i. The individual images used for alignment
 - ii. Cutouts of the images to be aligned (transparent middle section for easier manual alignment)

- iii. Overlays of the aligned image on the reference image to demonstrate the current alignment visually
3. Look through the overlays to determine if a manually alignment is necessary.
 - a. Manual alignments are only necessary if there visually appears to be a misalignment between the images used.
4. If no manual alignment is necessary based on the overlays, disregard the data.
5. If a manual alignment is necessary
 - a. Load one of the four reference images from the reference intercut volume into GIMP.
 - b. Open as a new layer the cut out of the corresponding alignment image for the reference image.
 - c. Manually move the cut out image over the reference image to the best visual alignment.
 - d. Determine the offset from the GIMP coordinates.
 - e. Open the Alignment_offsets.txt file in the working directory
 - f. Edit the appropriate line in the Alignment_offsets.txt file (this will correspond to the alignment number specified in the Nonideal_offsets.txt file as well as the name of the directory containing the relevant images for manual alignments).

- i. Note: subsequent lines should be incremented (or decremented) by the difference in the offset x and y values for this line. (i.e. offsets are cumulative)
 - g. The new offsets (x and y) are entered on the appropriate line of the Alignment_offsets.txt file (in the units of pixels - same as GIMP coordinates)
 - h. Save and close the file.
 6. If any manual alignments are performed. (And after all of them are performed.)
 - a. Change the reconstruct_parallel_multiovp.py flags to only stitch the images together and NOT to align again.
 - b. This will pull the new offset values for stitching.

Visualizing the Image Volume

1. The coordinates of the output slices are saved in Slice_coordinates.txt
 - a. The increasing slice number corresponds to deeper into the tissue which corresponds with greater z value.
2. The output slices can be loaded into a variety of image volume rendering softwares.
3. Recommended visualization tools include ImageJ/FIJI, Voxx, ImageVis3D, FluoRender.

4. For more information on these programs, see their respective help files or websites.

Laser GDD Correction

1. To adjust the GDD, go to the laser panel situated below the MRUX1, between the window and the table.
2. Press the “Menu Select” button and then go to “Dispersion Setting” followed by “Select Curve” and “Manual”
 - a. NOTE: To select each of these choices, use the “Menu Select” button.
3. Rotate the “Adjust” knob to manually adjust the GDD.
 - a. You can switch between coarse/fine adjustments by pressing the knob into the control panel.
 - b. After making adjustments to the GDD value, go back to the screen if the signal intensity has improved for the imaged portion of the sample.
 - i. If you are alone, use the “Snap” acquisition in the Zen Software (preferable). If you are working with a colleague you can use the “Live” scanning feature to make quicker adjustments.
 - c. NOTE: Try to keep the laser exposure to the sample as minimum as possible.
 - d. Rotate the knob clockwise/anticlockwise based on judgment and decide if the signal intensity is getting better or not.
 - i. Start with large adjustments and continue with smaller adjustments to find optimal GDD value.

- ii. Repeat this step till satisfied with the signal quality.
4. Once GDD value is settled, note it down in the Image Volume Acquisition Worksheet under section 16.
5. Press “Menu Exit” button till you exit out to the home screen.
6. Verify the GDD value displayed on the home screen with the recorded value in the worksheet.

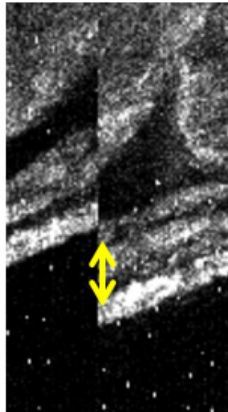
Setting up a Quick Z Acquisition

1. Refer the sections on “Turning on the system”, “Preparing the Sample to be imaged”, “Setting up Microscope” to get the setup running. If you already have the sample mounted and ready to image, go to the next step.
2. Follow steps 1-4 from the “Setting up the AVIM” section.
 - a. Be careful while naming the folder and files so as not to be confused with larger acquisitions.
3. Subtract 10 microns from the Z start value and use that as Z stop value in the LabVIEW program.
 - a. Record your estimated stop value for z on the worksheet.
 - b. Stop value MUST be LESS THAN Start value.
4. Go through the section for “Setting up an Acquisition” and follow the steps to start the acquisition.
 - a. Be careful while naming the folder and files so as not to be confused with larger acquisitions.
5. For reconstruction, refer to section “Image Volume Reconstruction Protocol”.

Rotary Stage Alignment

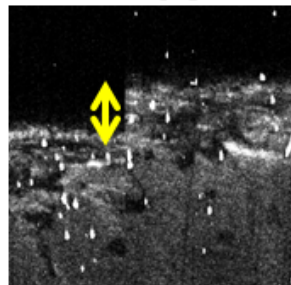
1. Check the rotary alignment of the system. This can be done by collecting a QuickZ for the surface, or even a smaller sub region of say 5 tiles by 5 tiles.
 - a. If collecting a smaller region, be sure that you are capturing tissue region in almost all the tiles. This will make it easier in identifying any misalignment.
2. Reconstruct the acquired volume, referring to the section “Image Volume Reconstruction Protocol”
3. Open the stitched slice, and look for any misalignments between two consecutive files.

Clockwise Bias



RIGHT image shifted DOWN of
LEFT image

Counterclockwise Bias



RIGHT image shifted UP of
LEFT image

- a. Compare the stitched image slice and the reference images above and compare and determine which bias is observed.

4. Once determined which bias is observed, walk over to the AVIM and adjust the Newport 481-A series rotary stage, between the stage and the adjustable legs of the system.
 - a. If a clockwise bias is observed, rotate the knob of the rotary stage counterclockwise, about $1/4^{\text{th}}$ of a turn.
 - b. If a counterclockwise bias is observed, rotate the knob of the rotary stage clockwise, about $1/4^{\text{th}}$ of a turn.
 - c. NOTE: All this while, leave the objective as it is. Keep it constant and only adjust the stage. This is very important.
5. Adjust the X and Y, Start and Stop values to ensure that some structure is acquired. Rotating the knob changes the area which is exposed to the objective.
6. Collect another Quick-Z and reconstruct and visually inspect the image acquired. Based on this, by trial and error, make the necessary adjustment to get an almost perfectly aligned image. Repeat the protocol as many times necessary.

Microtome Blade Adjustment

1. Follow the steps for “Turning on the system” and “Preparing the Sample to be Imaged” steps 1-10 to start things up. If you already have the sample mounted, go to the next step.
2. While performing manual cutting, observe the cut carefully, and see if the knife performs a good clean cut. i.e., the removed paraffin appears to be even throughout the cut.
3. If visible that the knife did not perform a good cut, i.e., one end may be deeper than the other (or only a portion of the sample was cut),
 - a. Note which side was deeper (or the side that was cut), the microscope side or the knife side.
 - b. If the cut was deeper on the microscope side, then make the cutting angle shallower. This can be done by loosening the top four screws on the AVIM, and then carefully rotating the bottom two screws (the same increment) such that the cutting knife angle becomes shallow, i.e. counter-clockwise.
 - i. It is recommended that increments are no larger than $\frac{1}{2}$ turn, smaller turns may be necessary when fine tuning.
 - c. If the cut was deeper on the knife side, then make the cutting angle deeper. This can be done by loosening the top four screws on the AVIM, and then

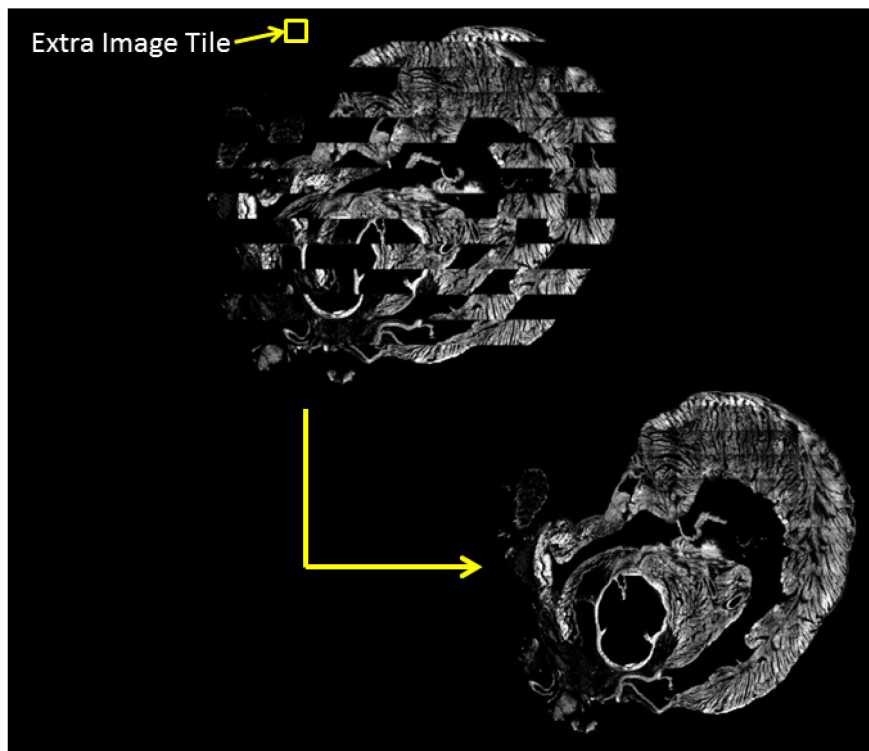
carefully and rotating the bottom two screws such that the cutting knife angle becomes deeper, i.e. clockwise.

- d. NOTE: Be careful to turn both bottom screws the same amount.
 - e. Retighten the top 4 screws on the AVIM, starting with the ones closest to the exposed blade.
4. If the blade angle was adjusted deeper, lower the sample ~100 microns from the prior cut height (the blade height was lowered, so the sample needs to be adjusted).
 5. After adjusting the knife angle, perform at least 3 cuts of 40 microns to achieve a representative cut using Automated_Cut_Control.vi, keeping a record of sample height to ensure you are removing ~40 microns per cut.
 6. After three cuts, if the cutting bias is still observed visually, repeat step 3 and try to minimize the bias.
 7. Once a good visible cut is achieved, proceed to obtaining a Quick-Z and reconstruct and visually inspect the image acquired.
 8. Check if there is uniform intensity across the entire image and if not, perform further adjustments to the knife angle based on the guidelines mentioned in step 3 and repeat steps 3-6.

Removing Extra Stacks

Some communication errors between the AVIM and the microscope can result in extra stacks being acquired. This is intentional in that the communication protocol has been designed so that any errors in communication result in extra stacks being acquired rather than missing a stack. The latter would result in the loss of data and possibly ruining an entire dataset as the imaging process is destructive.

If an extra stack is acquired during acquisition, it will be noticed during image volume reconstruction as a obviously jumbled image slice, seen in the top portion of the image below.



In order to remove the extra stack and get the image slice to look like the lower portion of the above image, follow the steps below.

1. Retrieve the AVIM_Log.txt file recorded during the image acquisition. If you did not save this file, proceed to Step 8 for a manual stack removal.
2. Backup your image stacks.
3. If you have not renamed your image stacks by setting the flag in the reconstruct_parallel.py script, set the flag to “1” and re-run the image volume reconstruction. You can set all other flags to “0” to speed up this process.
4. Copy Check_Log.py and remove_Stack.py into the directory containing the stack_folder, parameters.txt and AVIM_Log.txt for this image dataset.
5. Run “./Check_Log.py AVIM_Log.txt” from a command prompt (without the quotes). This will check for noticeable errors during acquisition.
6. If the output from Step 4 indicates that duplicate stacks were detected, you can automatically remove these stacks by running “./Check_Log.py AVIM_Log.txt REMOVE”
7. Run the reconstruction again and view the output image slices to verify that the stack removal fixed the reconstruction process. Be sure that you re-extract the image tiles from the image stacks. Otherwise, the slices will automatically be stitched using the old (out of order) stack order.
8. If there are remaining errors, the stacks must be removed manually. Identify a potential stack to remove. If the I/O board was not sufficiently far away from the actuator, these stacks can occur at the beginning of the image slice. This will be a trial and error process.
9. Remove the potential duplicate stack by running “./remove_Stack.py ##” (without the quotes) where ## corresponds to the number of the stack to remove.

10. Run the reconstruction again and check if the image slices are corrected reconstructed.

11. Repeat Steps 8-10 as necessary.

If a noticeable number of extra stacks are appearing immediately following a cut step, move the I/O board for the microscope farther away from the actuator and/or shield the I/O board from the actuator.

Appendix C Converting AVIM to Different Microscope

The AVIM was built, tested, and validated using a Zeiss 7MP microscope running Zen 2010 and Multi-Time 25.007. Multi-Time was modified by Zeiss to produce a more reliable communication with the AVIM over the long period of time required to run an image volume acquisition. Please contact Zeiss directly to see if different Multi-Time version will be similar to the 25.007 release.

While the microscope was central to the AVIM design and operation, only slight modifications to both the acquisition and reconstruction code can adapt the AVIM to a variety of other microscopes. The necessary changes are described below.

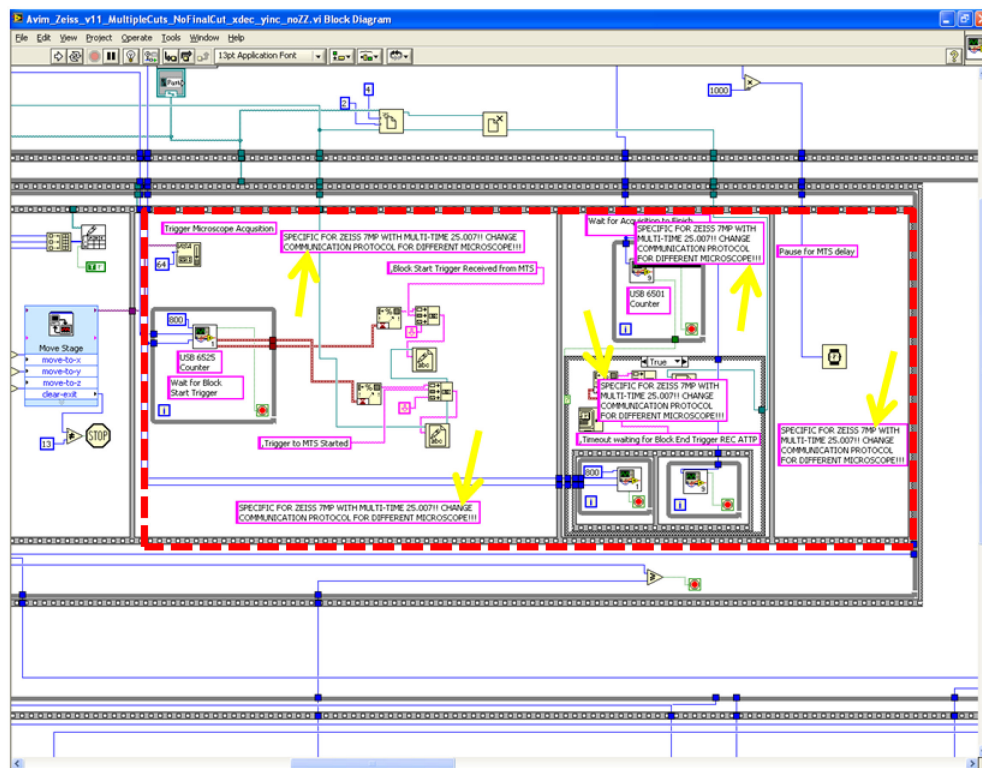
Changes to Acquisition LabVIEW Code

The communication protocol with the microscope represents the only code specific to the Zeiss 7MP. In order to adapt the AVIM to a different microscope, this communication protocol would have to be tailored to one suitable for the intended microscope. We found that having a very robust communication protocol was necessary to both ensure reliable acquisition of images throughout the sample and prevent delays as a result of communication timeouts. Significant testing was required to ensure that the communication protocol would function correctly and efficiently over a 24 hour acquisition.

Briefly, our communication protocol 1) AVIM positions stage; 2) AVIM sends a 5V 100 millisecond square wave pulse (referred to as trigger) repeatedly to 7MP to acquire image(s); 3) 7MP receives trigger from AVIM; 4) 7MP acknowledges receipt of AVIM

signal by sending a return trigger to AVIM; 5) 7MP acquires and saves image(s); 6) 7MP signals AVIM image acquisition complete; 7) AVIM repositions stage (or cuts sample); process repeats from step 1.

The area of the LabVIEW “Block Diagram” containing our communication protocol is highlighted below (red dashed box) and designated within the Diagram with multiple text boxes to bring the user’s attention to the area (yellow arrows). Everything within the red dashed box is part of the microscope communication protocol.



This portion of the code would need to be modified to interface with the intended microscope. A more simple communication protocol (a single trigger to the microscope to acquire and a single trigger to the AVIM to reposition the sample) may be possible

with different microscopes. The resulting communication protocol should be tested on a sample over a 24 hour acquisition to ensure an efficient and reliable protocol.

Changes to Reconstruction Python Code

The reconstruction software pipeline is written in Python, and has a library of functions (volrecon_parallel.py) that are called by the main python script (reconstruct.py). The microscope specific portion of the code is contained in isolated portions of these codes.

1. Within the reconstruct_parallel_multiovp.py:
 - a. Line 90: if cluster == 1:
 - i. This conditional (when cluster == 1) sets the path for the extra libraries required. If these libraries are not in the system path, they should be set here.
 - b. Line 150: ## Extract Single Images From Zeiss LSM format
 - i. This section reads in the Zeiss-specific naming format and sends it out to multiple processors to be rewritten as PNG files (universal format) associated with their coordinate index (line number) in the coordinates files gathered during the acquisition.
2. Within volrecon_parallel.py:
 - a. Line 288: def extract_pngs_parallel(cluster, ...
 - i. This function reads in LSM files and outputs image tiles in PNG format. The PNG files are saved under a file name corresponding to the line number in the coordinates file. This line number in the

- coordinates file contains the coordinates where the image tile (with that line number as its filename) was acquired within the sample.
- ii. An equivalent library will be needed to read in the proprietary format of the intended microscope so that the acquired images can be read by the python reconstruction script.
 - iii. The function will need to be modified to use the library found in item (ii).
- b. Line 4715: `def prepare_parallel(cluster, ...`
- i. This function reads in the parameters file created during the acquisition and the metadata from the acquired images (or image stacks).
 - ii. Lines 4754-4777 opens LSM file and reads necessary metadata needed to accurately reconstruct the image volume.
 - iii. This would need to be changed to read the appropriate file format and pull the metadata to fill the following variables
 1. `image_size_x` : dimension of image tile in μm
 2. `image_dim` : dimension of image tile in pixels
 3. `z_steps_per_stack` : number of tiles in an optical stack
 4. `z_opt_step` : distance in μm between tiles in optical stack
 5. `bits_per_pixel` : bit depth of acquired images

Bibliography

1. Go, A.S., et al., *Heart disease and stroke statistics--2014 update: a report from the American Heart Association*. Circulation, 2014. **129**(3): p. e28-e292.
2. Lee, K.L., et al., *Predictors of 30-day mortality in the era of reperfusion for acute myocardial infarction. Results from an international trial of 41,021 patients. GUSTO-I Investigators*. Circulation, 1995. **91**(6): p. 1659-68.
3. Stone, G.W., et al., *Predictors of in-hospital and 6-month outcome after acute myocardial infarction in the reperfusion era: the Primary Angioplasty in Myocardial Infarction (PAMI) trial*. J Am Coll Cardiol, 1995. **25**(2): p. 370-7.
4. Akar, F.G., et al., *The mitochondrial origin of postischemic arrhythmias*. J Clin Invest, 2005. **115**(12): p. 3527-35.
5. Brown, D.A., et al., *Effects of 4'-chlorodiazepam on cellular excitation-contraction coupling and ischaemia-reperfusion injury in rabbit heart*. Cardiovasc Res, 2008. **79**(1): p. 141-9.
6. Slodzinski, M.K., M.A. Aon, and B. O'Rourke, *Glutathione oxidation as a trigger of mitochondrial depolarization and oscillation in intact hearts*. J Mol Cell Cardiol, 2008. **45**(5): p. 650-60.
7. Jin, H., et al., *Altered spatiotemporal dynamics of the mitochondrial membrane potential in the hypertrophied heart*. Biophys J, 2010. **98**(10): p. 2063-71.
8. Lyon, A.R., et al., *Optical imaging of mitochondrial function uncovers actively propagating waves of mitochondrial membrane potential collapse across intact heart*. J Mol Cell Cardiol, 2010. **49**(4): p. 565-75.
9. Kleber, A.G. and Y. Rudy, *Basic mechanisms of cardiac impulse propagation and associated arrhythmias*. Physiol Rev, 2004. **84**(2): p. 431-88.
10. Weiss, H.R., et al., *Quantitative determination of regional oxygen consumption in the dog heart*. Circ Res, 1978. **42**(3): p. 394-401.
11. Aon, M.A., et al., *Sequential opening of mitochondrial ion channels as a function of glutathione redox thiol status*. J Biol Chem, 2007. **282**(30): p. 21889-900.
12. Aon, M.A., et al., *Synchronized whole cell oscillations in mitochondrial metabolism triggered by a local release of reactive oxygen species in cardiac myocytes*. J Biol Chem, 2003. **278**(45): p. 44735-44.
13. Aon, M.A., S. Cortassa, and B. O'Rourke, *Redox-optimized ROS balance: a unifying hypothesis*. Biochim Biophys Acta, 2010. **1797**(6-7): p. 865-77.
14. Le Grand, B., et al., *Pro-arrhythmic effect of nicorandil in isolated rabbit atria and its suppression by tolbutamide and quinidine*. Eur J Pharmacol, 1992. **229**(1): p. 91-6.
15. Zhou, L., et al., *Effects of regional mitochondrial depolarization on electrical propagation: implications for arrhythmogenesis*. Circ Arrhythm Electrophysiol, 2014. **7**(1): p. 143-51.
16. Aon, M.A., et al., *Mitochondrial criticality: a new concept at the turning point of life or death*. Biochim Biophys Acta, 2006. **1762**(2): p. 232-40.
17. Zorov, D.B., et al., *Reactive oxygen species (ROS)-induced ROS release: a new phenomenon accompanying induction of the mitochondrial permeability transition in cardiac myocytes*. J Exp Med, 2000. **192**(7): p. 1001-14.
18. Gao, J., et al., *Transmural gradients in Na/K pump activity and [Na⁺] in canine ventricle*. Biophys J, 2005. **89**(3): p. 1700-9.

19. Hoffman, J.I., *Transmural myocardial perfusion*. Prog Cardiovasc Dis, 1987. **29**(6): p. 429-64.
20. Osadchii, O.E., E. Soltysinska, and S.P. Olesen, *Na⁺ channel distribution and electrophysiological heterogeneities in guinea pig ventricular wall*. Am J Physiol Heart Circ Physiol, 2011. **300**(3): p. H989-1002.
21. Tsamis, A., et al., *Active contraction of cardiac muscle: in vivo characterization of mechanical activation sequences in the beating heart*. J Mech Behav Biomed Mater, 2011. **4**(7): p. 1167-76.
22. Denk, W., J.H. Strickler, and W.W. Webb, *Two-photon laser scanning fluorescence microscopy*. Science, 1990. **248**(4951): p. 73-6.
23. Minsky, M., *Memoir on Inventing the Confocal Scanning Microscope*. Scanning, 1988. **10**(4): p. 128-138.
24. Ashworth, S.L., et al., *Two-photon microscopy: visualization of kidney dynamics*. Kidney Int, 2007. **72**(4): p. 416-21.
25. Ohler, A., et al., *Two-photon laser scanning microscopy of the transverse-axial tubule system in ventricular cardiomyocytes from failing and non-failing human hearts*. Cardiol Res Pract, 2009. **2009**: p. 802373.
26. Akar, F.G., et al., *Dynamic changes in conduction velocity and gap junction properties during development of pacing-induced heart failure*. Am J Physiol Heart Circ Physiol, 2007. **293**(2): p. H1223-30.
27. Dolber, P.C. and M.S. Spach, *Conventional and confocal fluorescence microscopy of collagen fibers in the heart*. J Histochem Cytochem, 1993. **41**(3): p. 465-9.
28. Mac Gabhann, F. and S.M. Peirce, *Collateral capillary arterIALIZATION following arteriolar ligation in murine skeletal muscle*. Microcirculation, 2010. **17**(5): p. 333-47.
29. Skoch, J., et al., *In vivo imaging of amyloid-beta deposits in mouse brain with multiphoton microscopy*. Methods Mol Biol, 2005. **299**: p. 349-63.
30. Jain, R.K., L.L. Munn, and D. Fukumura, *Dissecting tumour pathophysiology using intravital microscopy*. Nat Rev Cancer, 2002. **2**(4): p. 266-76.
31. Helmchen, F. and W. Denk, *Deep tissue two-photon microscopy*. Nat Methods, 2005. **2**(12): p. 932-40.
32. Ustione, A. and D.W. Piston, *A simple introduction to multiphoton microscopy*. J Microsc, 2011. **243**(3): p. 221-6.
33. Ragan, T., et al., *Two-photon tissue cytometry*. Methods Cell Biol, 2004. **75**: p. 23-39.
34. Sands, G.B., et al., *Automated imaging of extended tissue volumes using confocal microscopy*. Microsc Res Tech, 2005. **67**(5): p. 227-39.
35. Ragan, T., et al., *Serial two-photon tomography for automated ex vivo mouse brain imaging*. Nat Methods, 2012. **9**(3): p. 255-8.
36. Chow, S.K., et al., *Automated microscopy system for mosaic acquisition and processing*. J Microsc, 2006. **222**(Pt 2): p. 76-84.
37. Hovhannisyan, V.A., et al., *Image heterogeneity correction in large-area, three-dimensional multiphoton microscopy*. Opt Express, 2008. **16**(7): p. 5107-17.
38. Nelder, J.A. and R. Mead, *A Simplex-Method for Function Minimization*. Computer Journal, 1965. **7**(4): p. 308-313.

39. Rosenfeld, A., *Digital Picture Processing*. 1982, Orlando, FL: Academic Press.
40. Gopinath, S., et al., *A statistical approach for intensity loss compensation of confocal microscopy images*. J Microsc, 2008. **230**(Pt 1): p. 143-59.
41. Guan, Y.Q., et al., *Adaptive correction technique for 3D reconstruction of fluorescence microscopy images*. Microsc Res Tech, 2008. **71**(2): p. 146-57.
42. Lee, S.C. and P. Bajcsy, *Intensity correction of fluorescent confocal laser scanning microscope images by mean-weight filtering*. J Microsc, 2006. **221**(Pt 2): p. 122-36.
43. Schneider, C.A., W.S. Rasband, and K.W. Eliceiri, *NIH Image to ImageJ: 25 years of image analysis*. Nat Methods, 2012. **9**(7): p. 671-5.
44. Institute, S.C.a.I. "*ImageVis3D*" *An interactive visualization software system for large-scale volume data*. Scientific Computing and Imaging Institute (SCI). Available from: <http://www.imagevis3d.org>.
45. LeGrice, I.J., et al., *Laminar structure of the heart: ventricular myocyte arrangement and connective tissue architecture in the dog*. Am J Physiol, 1995. **269**(2 Pt 2): p. H571-82.
46. Streeter, D.D., Jr., et al., *Fiber orientation in the canine left ventricle during diastole and systole*. Circ Res, 1969. **24**(3): p. 339-47.
47. Scollan, D.F., et al., *Reconstruction of cardiac ventricular geometry and fiber orientation using magnetic resonance imaging*. Ann Biomed Eng, 2000. **28**(8): p. 934-44.
48. Helm, P., et al., *Measuring and mapping cardiac fiber and laminar architecture using diffusion tensor MR imaging*. Ann N Y Acad Sci, 2005. **1047**: p. 296-307.
49. Arts, T., et al., *Relating myocardial laminar architecture to shear strain and muscle fiber orientation*. Am J Physiol Heart Circ Physiol, 2001. **280**(5): p. H2222-9.
50. Young, A.A., et al., *Extended confocal microscopy of myocardial laminae and collagen network*. J Microsc, 1998. **192**(Pt 2): p. 139-50.
51. Smith, R.M., et al., *Nondestructive optical determination of fiber organization in intact myocardial wall*. Microsc Res Tech, 2008. **71**(7): p. 510-6.
52. Brown, D.A., et al., *Cardiac arrhythmias induced by glutathione oxidation can be inhibited by preventing mitochondrial depolarization*. J Mol Cell Cardiol, 2010. **48**(4): p. 673-9.
53. Carmeliet, E., *Cardiac ionic currents and acute ischemia: from channels to arrhythmias*. Physiol Rev, 1999. **79**(3): p. 917-1017.
54. Pandit, S.V., et al., *Left-to-right ventricular differences in I(KATP) underlie epicardial repolarization gradient during global ischemia*. Heart Rhythm, 2011. **8**(11): p. 1732-9.
55. Smith, R.M., S.S. Velamakanni, and E.G. Tolkacheva, *Interventricular heterogeneity as a substrate for arrhythmogenesis of decoupled mitochondria during ischemia in the whole heart*. Am J Physiol Heart Circ Physiol, 2012. **303**(2): p. H224-33.
56. Halestrap, A.P., et al., *Cyclosporin A binding to mitochondrial cyclophilin inhibits the permeability transition pore and protects hearts from ischaemia/reperfusion injury*. Mol Cell Biochem, 1997. **174**(1-2): p. 167-72.

57. Birnbaum, Y., et al., *ECG diagnosis and classification of acute coronary syndromes*. Ann Noninvasive Electrocardiol, 2014. **19**(1): p. 4-14.
58. Noriega, F.J., et al., *Influence of the extent of coronary atherosclerotic disease on ST-segment changes induced by ST elevation myocardial infarction*. Am J Cardiol, 2014. **113**(5): p. 757-64.
59. Piper, H.M., et al., *The role of Na⁺/H⁺ exchange in ischemia-reperfusion*. Basic Res Cardiol, 1996. **91**(3): p. 191-202.
60. Stromer, H., et al., *Na⁽⁺⁾/H⁽⁺⁾ exchange inhibition with HOE642 improves postischemic recovery due to attenuation of Ca⁽²⁺⁾ overload and prolonged acidosis on reperfusion*. Circulation, 2000. **101**(23): p. 2749-55.
61. Pike, M.M., et al., *NMR measurements of Na⁺ and cellular energy in ischemic rat heart: role of Na⁽⁺⁾-H⁺ exchange*. Am J Physiol, 1993. **265**(6 Pt 2): p. H2017-26.
62. Das, B. and C. Sarkar, *Is preconditioning by oxytocin administration mediated by iNOS and/or mitochondrial K(ATP) channel activation in the in vivo anesthetized rabbit heart?* Life Sci, 2012. **90**(19-20): p. 763-9.
63. Halestrap, A.P., *A pore way to die: the role of mitochondria in reperfusion injury and cardioprotection*. Biochem Soc Trans, 2010. **38**(4): p. 841-60.
64. Li, X., et al., *Metabolic adaptation to a disruption in oxygen supply during myocardial ischemia and reperfusion is underpinned by temporal and quantitative changes in the cardiac proteome*. J Proteome Res, 2012. **11**(4): p. 2331-46.
65. Yellon, D.M. and D.J. Hausenloy, *Myocardial reperfusion injury*. N Engl J Med, 2007. **357**(11): p. 1121-35.
66. Taylor, R.R., *Myocardial potassium and ventricular arrhythmias following reperfusion of ischaemic myocardium*. Aust N Z J Med, 1971. **1**(2): p. 114-20.
67. Kohlhaas, M., et al., *Elevated cytosolic Na⁺ increases mitochondrial formation of reactive oxygen species in failing cardiac myocytes*. Circulation, 2010. **121**(14): p. 1606-13.
68. O'Rourke, B., J.E. Van Eyk, and D.B. Foster, *Mitochondrial protein phosphorylation as a regulatory modality: implications for mitochondrial dysfunction in heart failure*. Congest Heart Fail, 2011. **17**(6): p. 269-82.

Curriculum Vitae

Education

Ph.D. Candidate Biomedical Engineering, Johns Hopkins University.

Advisor: Raimond Winslow. (2003 – 2014)

B.S.E. Biomedical and Electrical Engineering, Duke University, Durham, NC, (1999-2003)

Research Experience

Institute for Computation Medicine (June 2004 – 2014)

Advisor: Dr. Raimond Winslow

My work focuses on image metabolic sinks in an ischemic heart. This involved the design and manufacture of an automated volume imaging microtome that expanded the imaging capabilities of a two-photon microscope to acquire image volumes as large as a rodent heart at high resolution. The resulting images are processed through a custom software pipeline where imaging artefacts are removed and images are registered and stitched into a high quality image volume accurately representing the structure of the imaged sample. The distribution and prevalence of metabolic sinks in an intact ischemic heart were demonstrated in a guinea pig heart to illustrate the importance of this arrhythmogenic component following an ischemia-reperfusion injury.

Sean Sun's Group – (Sept 2003 – June 2004)

Advisor: Dr. Sean Sun

My project was to model protein elasticity in alpha helices. An alpha helix composed of alanine amino acids was taken from the 1BMF protein and modeled. Charmm (Chemistry at HARvard Molecular Mechanics), a program for macromolecular simulations, was used to simulate the trajectories of the amino acids during heating. It was found that the angle of the alpha helix during heating fell into a bimodal distribution suggesting two states of energy minimization for an alpha helix.

Journal Publications

R. Kazmierski, A. Shah, B. O'Rourke and R. Winslow. Modular, Open Source Instrumentation for High Resolution 3D Imaging of Cardiac Microstructure (*in preparation*)

R. Kazmierski, A. Shah, B. O'Rourke and R. Winslow. Spatial Properties of Metabolic Sinks and Their Relationship to Ischemia Reperfusion Arrhythmias. *Biophysical Journal*, (*in preparation*)

Conference Proceedings and Posters

Robert T. Kazmierski, Tabish Almas, Fadi G. Akar, Raimond L. Winslow. Interplay between cell-cell coupling and NCX heterogeneity establishes transmural APD gradient in heart failure. Biomedical Engineering Society. Chicago, IL, October 2006.

Teaching Assistant Experience

Johns Hopkins University

NHLBI Short Course: Integrative Computational Modeling of the Cardiac Myocyte (Aug 2008, 2009)

(experimental biomedical researchers and clinician-scientists)

Models and Simulation (Jan-May 2007, Mar-May 2006)

(sophomore undergraduates)

Awards and Recognition

Pratt Fellowship (2002-2003)

Extra-Curricular Activities

Student Recruitment Co-Chair July 2005-June 2006